

# Remodelling a multi-anode ionisation chamber detector for accelerator mass spectrometry of $^{53}\text{Mn}$

Guy T. Leckenby

A thesis submitted for the degree of  
Bachelor of Philosophy (Science) with Honours in Physics at  
The Australian National University



October 2017



---

# Declaration

---

This thesis is an account of research undertaken between February 2017 and October 2017 at the Department of Nuclear Physics, Research School of Physics and Engineering, the Australian National University, Canberra, Australia.

Except where acknowledged in the customary manner, the material presented in this thesis is, to the best of my knowledge, original and has not been submitted in whole or part for a degree at any university.



---

Guy T. Leckenby  
October 2017



---

# Acknowledgements

---

Undoubtedly, the biggest thanks go to my supervisor, Anton Wallner, for his guidance, humour, and great company through those many hours spent pumping the Enge up and down. Toni's explanations were always thorough and his patience was invaluable, especially when I appeared with a new question on uncertainties every ten minutes. Thank you to Stefan Pavetich, for dealing with numerous inane questions about the DCP, and for his epic 36 hour sleepless effort during our final accelerator run. To Martin Martschini, thank you for helping me decode the mystery that is Raytrace from the other side of the world, your patience and thorough explanations were enormously helpful. For Reetika Vadgaonkar, thank you for sharing the sample pressing load, we made a great team. Finally, thank you to Steve Tims for his inexhaustible knowledge of the accelerator, to Michaela Fröhlich for her patience with my chemical ineptitude.

Thank you to Jean Faullimmel, Angus Gruen, Siobhan Tobin, Matt Berrington and Alex Bennet for proof-reading my thesis; your humour was less funny than you think but your comments were more helpful than you know. Special shout out to Michaela Ripper for sharing many late hours in the office together, thank you for guilting me into working and for all the Overwatch related bants, it made 8pm seem not so dark. Thank you to the honours crew of 2017, our camaraderie over shared misery and delectably cheap burgers always made for a Wednesday to look forward to.

To my dearest Kim Chen, thank you for your love, patience and support over all these years, you make me happy even when your feet are made of ice. To Eloise Burns and Radhika Bhatia, thank you for putting up with my eccentricities with a wry smile and making a house into a home. For my parents, Lisa Holley and David Leckenby, thank you for getting me here in such great shape despite my best efforts, your years of compassion and inspiration are the reason I am here and love what I do. Thanks to my bro, Josh Leckenby, for keeping things real, and to my grandmother Elaine Sherwood for blowing my trumpet loud and clear, even when you have no idea what I've achieved. Finally, to my one true love-hate relationship Ultimate Disc, thank you for breaking me and healing me in equal measures, I've been addicted ever since we met.



---

# Abstract

---

Accelerator Mass Spectrometry (AMS) is a single-atom counting technique that measures the abundance of rare, long-lived radioisotopes using only milligrams of sample. The astrophysical radioisotopes  $^{53}\text{Mn}$  and  $^{60}\text{Fe}$  have been utilised for many applications including meteoritics, exposure dating, and the search for near-Earth supernovae.  $^{53}\text{Mn}$  measurements at the ANU have been limited to sensitivities above  $10^{-13}$  by insufficient suppression of the stable isobar,  $^{53}\text{Cr}$ . To expand the applications accessible to  $^{53}\text{Mn}$  analysis, a new detector was commissioned that will improve the available sensitivity.

This thesis covers the implementation of the new Flexible Anti-Scatter Multi-Anode (FASMA) detector. Simulations were conducted to determine the optimal placement of the detector inside the gas-filled magnet, and to assist with the design of a new multi-anode configuration. The FASMA detector was successfully tested and full spectra were recorded. These preliminary results indicate an improvement in the achievable sensitivity, even without the suppression of scattered particles. With further work, the FASMA detector should reach a sensitivity at or below  $10^{-14}$ , which is competitive with the best reported level in the field.

Long-lived radionuclides, such as  $^{53}\text{Mn}$  and  $^{60}\text{Fe}$ , are important for extracting the exposure history of meteorites, both in space and on Earth, as well helping to identify their origin. In light of this, cosmogenic  $^{53}\text{Mn}$  and  $^{60}\text{Fe}$  ratios were measured in ten meteorite samples. Since the available data on live  $^{53}\text{Mn}$  and  $^{60}\text{Fe}$  is scarce, these measurements will improve the constraints on current production rate models for meteorites.



---

# Contents

---

<b>Declaration</b>	<b>iii</b>
<b>Acknowledgements</b>	<b>v</b>
<b>Abstract</b>	<b>vii</b>
<b>1 Introduction</b>	<b>1</b>
1.1 Applications of Manganese-53 and Iron-60 . . . . .	2
1.1.1 Manganese-53 as a Dating Tool . . . . .	2
1.1.2 Near-Earth Supernovae Search . . . . .	3
1.1.3 Meteorites . . . . .	4
1.1.4 Half-life Measurements . . . . .	5
1.2 Thesis Outlook . . . . .	5
1.2.1 Conventions . . . . .	6
<b>2 Accelerator Mass Spectrometry</b>	<b>7</b>
2.1 Principles of AMS Systems . . . . .	9
2.1.1 The Negative Ion Source . . . . .	9
2.1.2 The Injection System . . . . .	10
2.1.3 Acceleration and Stripping . . . . .	10
2.1.4 High Energy Mass Analysis . . . . .	11
2.1.5 Single Particle Detection . . . . .	12
2.2 Gas-Filled Magnet . . . . .	13
2.2.1 Isobar Suppression . . . . .	15
2.2.2 The ANU Enge Split-Pole Magnetic Spectrograph . . . . .	15
2.3 Multi-Anode Ionisation Chamber Detector . . . . .	17
2.3.1 Frisch Grid . . . . .	17
2.3.2 Anode Splitting . . . . .	18
2.3.3 Detector Gas . . . . .	18
2.4 Ratio Measurements . . . . .	20
2.4.1 Normalisation Procedures . . . . .	20
2.4.2 Ratio Applications . . . . .	21
<b>3 Simulating Ion Stopping</b>	<b>23</b>
3.1 Energy Loss in Matter . . . . .	23
3.1.1 Electronic Stopping Power . . . . .	23
3.1.2 Straggling . . . . .	25
3.2 Raytrace and the Enge Split-pole Spectrograph . . . . .	26
3.2.1 Charge-Changing Collision Theory . . . . .	26
3.2.2 Separation Results . . . . .	28
3.2.3 Experimental Comparison . . . . .	30
3.2.4 Magnetic Field Optimisation . . . . .	32

---

3.2.5	Pressure Optimisation . . . . .	33
3.3	SRIM Simulation of the Ionisation Chamber . . . . .	34
3.3.1	Ionisation Curves . . . . .	34
3.3.2	Single Ion Counting with SRIM . . . . .	36
<b>4</b>	<b>Meteorite Measurements</b>	<b>39</b>
4.1	The Current Detector . . . . .	39
4.1.1	Physical Schematics . . . . .	39
4.1.2	Electronics . . . . .	41
4.2	Manganese Measurements . . . . .	42
4.2.1	Energy Peak Drift . . . . .	43
4.2.2	Spectra Analysis . . . . .	44
4.3	Iron Analysis . . . . .	48
4.3.1	Spectra Analysis . . . . .	48
<b>5</b>	<b>The New FASMA Detector</b>	<b>51</b>
5.1	Drawbacks of the Current Design . . . . .	51
5.2	FASMA Detector Design . . . . .	52
5.2.1	Anode Board . . . . .	53
5.2.2	Geometry . . . . .	55
5.2.3	Detector Housing . . . . .	56
5.2.4	Predicted Resolution . . . . .	58
5.3	First Trial . . . . .	59
5.3.1	Angular Vetting . . . . .	61
5.3.2	Sensitivity . . . . .	62
5.4	Future Characterisation . . . . .	63
5.4.1	Electronics and Resolution . . . . .	63
5.4.2	Anode Design . . . . .	64
5.4.3	Other Isotopes . . . . .	65
<b>6</b>	<b>Conclusion</b>	<b>67</b>
6.1	Future Directions . . . . .	68
<b>A</b>	<b>Beam Width Fitting</b>	<b>69</b>
<b>B</b>	<b>Meteorite Data</b>	<b>71</b>
B.1	Manganese Data . . . . .	71
B.2	Iron Data . . . . .	75
<b>Bibliography</b>		<b>77</b>

# Introduction

---

*“By convention sweet is sweet, by convention bitter is bitter, by convention hot is hot, by convention cold is cold, by convention colour is colour. But in reality there are atoms and the void.”*

- Democritus, 5<sup>th</sup> century BCE [1].

In today’s age of scientific enlightenment, it is well known that matter consists of discrete units called atoms (although they themselves are not as discrete as their name suggests). If we can describe the constituents of matter on the atomic scale, then we know the fundamental composition of a sample on the most basic level. This is what Accelerator Mass Spectrometry (AMS) attempts to achieve. AMS is an analytic technique that aims to determine the abundance levels of extremely rare isotopes in samples. Broadly speaking, this refers to long-lived radioisotopes that are typically present in very small abundances, as stable isotopes are usually abundant enough for other methods. The technique has evolved over the past 40 years and established routines are developed for 55 radioisotopes [2], each with their own set of applications. AMS is used across disciplines as broad as archaeology, to environmental studies, and fundamental nuclear physics; with carbon-14, used for radio-carbon dating, being the most common application of AMS.

The low natural abundances ( $10^{-12}$  to  $10^{-18}$  g/g) and long half lives (10 to  $10^8$  years) of the isotopes used in AMS make them impractical to analyse with other techniques. AMS outperforms the sensitivity of decay counting, the most obvious choice for radionuclide detection, for isotope ratios of less than  $10^{-12}$  and only requires milligrams of sample, whereas decay counting can require tons of sample material. Other mass spectrometric methods are either limited by their sensitivity, or their ability to deal with interfering species. Inductively Coupled Plasma Mass Spectrometry (ICP-MS) can in principle measure concentrations as low as one part in  $10^{15}$  [3, 4]. However, this precision is severely limited by the interference of other species that are often many times more abundant. Alternatively, Resonance Ionisation Mass Spectrometry (RIMS) has excellent isobar suppression and can utilise sample sizes as low as  $10^6$  atoms, but it is limited to isotopic sensitivities above  $10^{-12}$  [5]. Thus AMS is the optimal choice for counting most long-lived radioisotopes.

This thesis will focus on AMS methods for the astrophysical radioisotopes manganese-53 and iron-60. Both of these isotopes have a broad variety of applications but are intensively challenging to measure experimentally due to the interfering stable isobars chromium-53 and nickel-60 respectively. Whilst AMS analysis of  $^{60}\text{Fe}$  at the ANU has been optimised to a satisfactory sensitivity, the sensitivity of  $^{53}\text{Mn}$  measurements needs to be improved before the full extent of its applications can be exploited. As a testament to how difficult the measurement is, only two other institutions in the world [6, 7] can

currently measure  $^{53}\text{Mn}$ , and only the Technical University of Munich has been able to measure natural samples. This being said, TU Munich has demonstrated sensitivity approximately 50 times better than our current measurement limit. This thesis primarily examines the implementation of a new detector that aims to improve our sensitivity to match that demonstrated by Munich.

## 1.1 Applications of Manganese-53 and Iron-60

Both of these radionuclides have an impressive suite of astrophysical and other applications. This section provides an overview of some of the more promising and successful applications of  $^{53}\text{Mn}$  and  $^{60}\text{Fe}$ .

### 1.1.1 Manganese-53 as a Dating Tool

Traditionally, the AMS isotopes of beryllium-10, aluminium-26, and chlorine-36 have been used for surface exposure dating and geomorphological studies [2, 8, 9]. These isotopes are formed *in situ* by interactions between secondary cosmic rays (fast neutron/muons) and the target nuclei in rock. For  $^{10}\text{Be}$  and  $^{26}\text{Al}$ , the target is the oxygen and silicon in quartz. For  $^{36}\text{Cl}$  in surface rock, spallation of  $^{39}\text{K}$  and  $^{40}\text{Ca}$  is the most dominant production channel. These radionuclides are particular useful for studying the chronology of landforms through exposure ages, erosion rates and burial dating [10]. Features such as glacial movements, meteorite impacts, fault movements, and lava flows can all be traced using these methods, which are exclusive to AMS due to the low cosmogenic production rate. For further detail on exposure dating, refer to Fifield [8].

The conditions for reliable exposure dating using these isotopes can be somewhat limited and an expansion of the available isotopes is welcome. In particular, harshly arid environments like Australian landscapes can leave little quartz available for production of  $^{10}\text{Be}$  and  $^{26}\text{Al}$  [11]. Furthermore, the time scale of exposure dating is limited by the half-life of  $^{10}\text{Be}$  (the longest of the trio) at 1.39 Ma.  $^{53}\text{Mn}$  potentially overcomes both limitations. It has a half-life of 3.7 Ma [12], which considerably extends the time scale and sensitivity of datable lithologies. It is produced *in situ* by spallation of  $^{56}\text{Fe}$  in iron minerals, particularly laterites and ferricretes, and exhibits the largest predicted production rate of any long-lived cosmogenic isotope [9]. Since iron minerals are often more resistant to weathering, they can remain after other minerals have leached away. This means  $^{53}\text{Mn}$  has considerable potential in exposure dating alone; for more information see Schaefer et al. [10].

$^{53}\text{Mn}$  is also produced in much larger amounts in extraterrestrial matter, via cosmic ray spallation of  $^{56}\text{Fe}$ . Influx of extraterrestrial dust and meteorites results in a fairly constant  $^{53}\text{Mn}$  deposition rate that is traceable in the ferro-manganese crust and sediment deposits in deep ocean areas. Supposing that the characterisation of the flux of interplanetary dust particles does prove to be constant, then  $^{53}\text{Mn}$  could be developed for dating the hydrogenetic manganese crusts over significantly longer time scales than currently available [6]. Initial evidence has already been presented by the Munich group for crust dating back to  $\sim 20$  Ma [13].

Geochronological applications require sensitivities at the  $10^{-12}$  level, which is just achievable with the current  $^{53}\text{Mn}$  set-up at the ANU. However, crust dating is only limited by the sensitivity of the AMS measurement. To unlock the capability of  $^{53}\text{Mn}$  as a dating tool, the sensitivity of  $^{53}\text{Mn}$  measurements needs to be improved.

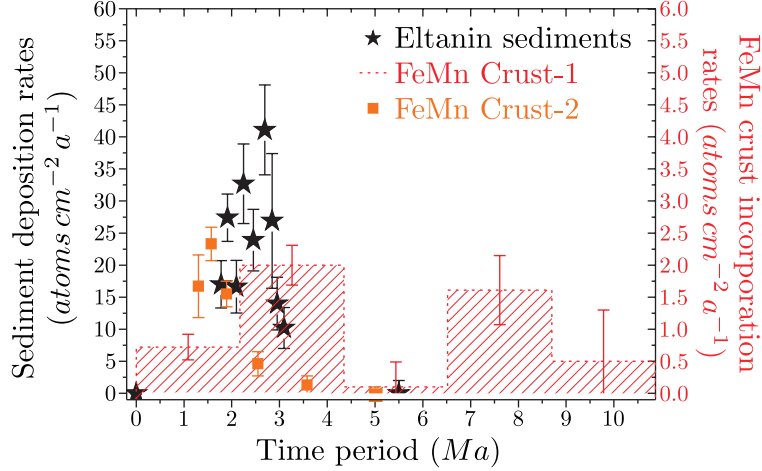


**Figure 1.1:** The deposition rates for sediment samples and incorporation rates for two crust samples. The error bars are  $1\sigma$  and include all scaled uncertainties. Sediment samples have a 0.1 Ma, Crust-1 a 0.3 Ma and Crust-2 a 0.5 Ma temporal uncertainty. This figure is reproduced from Wallner et al. [18].

### 1.1.2 Near-Earth Supernovae Search

$^{60}\text{Fe}$  has less terrestrial applications than  $^{53}\text{Mn}$  but is particularly powerful for studying stellar and interstellar processes because the natural background levels are very low. The main production pathway is the  $s$ -process from  $^{56}\text{Fe}$ ; however, at low neutron densities  $^{60}\text{Fe}$  is shielded by the  $\beta$ -decay of  $^{59}\text{Fe}$  [14]. As a result of the absence of any other significant production channels, the majority of observed  $^{60}\text{Fe}$  abundance is a direct result of production by massive stars just before supernovae explosions, or ejection via stellar winds by late stage asymptotic-giant-branch (AGB) stars [15]. Spallation reactions on  $^{60}\text{Ni}$  are also a source of  $^{60}\text{Fe}$ , but for galactic distributions, this contribution is negligible compared to the supernovae production.

Although there is a wide range of astrophysical applications for  $^{60}\text{Fe}$ , the ANU has contributed significantly to the near-Earth supernovae search. The presence of above-background levels of live<sup>1</sup>  $^{60}\text{Fe}$  in the deep-sea ferro-manganese crust is strongly indicative of global  $^{60}\text{Fe}$  deposition by supernovae events within 100 parsecs of earth [13, 16–18]. Four different sediment cores and two ferro-manganese crusts and nodules from the Indian, Pacific, and Atlantic oceans were measured for their  $^{60}\text{Fe}/\text{Fe}$  ratios. Each sample set was dated using  $^{10}\text{Be}$ : the sediment cores had very fine time resolution of less than 30 ka, whilst the crusts and nodule samples had a poorer time resolution of approximately 2 Ma on average. From the ratio and date of each sample, the  $^{60}\text{Fe}$  sediment deposition rate and crust incorporation rate could be calculated, and the results are presented in Figure 1.1. These signals indicate a  $^{60}\text{Fe}$  interstellar influx at 1.5–3.2 million years ago, and again at 6.5–8.7 million years.

Wallner et al. [18] found that the measured spread of 1.5 Ma is inconsistent with modelling, which suggested a time spread of approximately 100–400 ka. The broader time distribution indicates multiple supernovae events in quick succession, as opposed to a single event. This hypothesis is supported by extensive modelling by Breitschwerdt et al. [19], who suggest that the deposited  $^{60}\text{Fe}$  was generated from 14–20 supernovae explosions that

<sup>1</sup>Live radionuclides are those that have not yet decayed.

formed the Local Bubble. The Local Bubble is a cavity of hot, diffuse plasma in the interstellar medium that is 300 light years across and contains the solar system and surrounding stars. The supernova modelling indicates that the most probable scenario for the deposition of the majority of the observed  $^{60}\text{Fe}$  resulted from two supernovae events at a distance of 90-100 parsecs, 2.3 and 1.5 million years ago. The remaining supernovae contributed less as they happened further away and longer ago. The implications of these results have strengthened arguments regarding the structure and formation of the hot plasma surface that makes up the Local Bubble.

Originally,  $^{53}\text{Mn}$  was also a serious contender for measuring the supernovae deposition signal.  $^{53}\text{Mn}$  is produced in much higher abundances in supernovae (potentially by an order of magnitude) [17] and has an even longer half-life than  $^{60}\text{Fe}$ , so should produce a stronger signal. However, the signal on Earth is obscured by a constant background signal generated from extraterrestrial dust and meteorite influx; any supernovae signal would have to be disentangled from this background. Furthermore, the  $^{60}\text{Fe}$  measurements revealed that the supernovae signal was much broader than the modelling predicted, which would make  $^{53}\text{Mn}$  measurements even more challenging than expected. There is still the potential that if the  $^{53}\text{Mn}$  background can be better understood, then  $^{53}\text{Mn}$  could be useful in contributing to the results of the near-Earth supernovae search.

### 1.1.3 Meteorites

Cosmogenic radionuclides are also used extensively in meteoritics and extraterrestrial studies. Meteoroids are exposed to solar (SCR) and galactic cosmic ray (GCR) particles that react with target nuclei in the meteoroid to produce a variety of cosmogenic isotopes [20]. These radioisotopes provide a history of the irradiated body, and can also produce information on the incoming cosmic radiation itself. Typically, SCR particles only penetrate a few mm into the body and the products are often lost by ablation upon atmospheric entry. GCR particles penetrate up to 50 cm into the body [21] and survive Earth entry as a result. Iron meteorites in particular (as opposed to younger stony meteorites) have been exposed to GCRs over hundreds of millions of years and a full suite of long-lived radionuclides is required to unravel their exposure history.

Traditionally, abundance levels of the cosmogenic noble gases of  $^{3,4}\text{He}$ ,  $^{20,21,22}\text{Ne}$ , and  $^{36,38,40}\text{Ar}$  are used in conjunction with AMS measurements of the radionuclides  $^{10}\text{Be}$ ,  $^{26}\text{Al}$ ,  $^{36}\text{Cl}$ ,  $^{41}\text{Ca}$ ,  $^{53}\text{Mn}$ , and  $^{60}\text{Fe}$ . Together, this information can be used to determine the terrestrial age, the exposure age, the pre-atmospheric size, and more [20].  $^{53}\text{Mn}$  has two main advantages over other nuclides: the target nuclei consists almost exclusively of  $^{56}\text{Fe}$  which makes production rates easy to predict; and no other radionuclides produced *in situ* have a comparably long half-life [22]. Similarly,  $^{60}\text{Fe}$  is produced *in situ* via spallation on only  $^{62}\text{Ni}$  and  $^{64}\text{Ni}$  providing predictable production rates. It can also be used to monitor the secondary neutron flux in meteoroids, and provides a unique determination between cosmic dust particles and ablated matter [23].  $^{53}\text{Mn}$  and  $^{60}\text{Fe}$  are used routinely in meteorite studies [24–26]; however, their further use has been stymied by a lack of experimental data to validate exposure models [20]. Chapter 4 aims to partially remedy this problem.

Meteorites can also provide important constraints on the formation of our solar system. In particular, anomalies in the amount of meteoritic  $^{60}\text{Ni}$  provides evidence for the existence of live  $^{60}\text{Fe}$  in the early solar system [27–29]. Supposing enough  $^{60}\text{Fe}$  survived, it would have acted as a heat source that melted planetesimals and meteoroids as they

---

first coalesced [27]. Recent measurements indicate that this abundance of  $^{60}\text{Fe}$  originated from a late supernova injection into the protoplanetary disk [30]. This particular hypothesis constrains the environment where solar formation could have occurred, implying that formation occurred in a dense stellar cluster in the company of many massive stars.

#### 1.1.4 Half-life Measurements

All of the above applications require accurate determination of the half-life of the radionuclide if absolute values are to be predicted. Recently the half-life of  $^{60}\text{Fe}$  was revised significantly and found to be 75% longer than the previously reported value [31, 32]. AMS played a crucial role in confirming this revision.  $^{53}\text{Mn}$  absolute values are currently limited by a five decade old half-life measurement with a 10% uncertainty. Potential revision is also required here considering the blooming applications of  $^{53}\text{Mn}$ .

## 1.2 Thesis Outlook

The current detector that is used for  $^{53}\text{Mn}$  and  $^{60}\text{Fe}$  was adapted for AMS purposes in the early 2000s and whilst it is sufficient for other isotopes, it has demonstrated significant shortfalls that have limited the sensitivity of  $^{53}\text{Mn}$  measurements. As a result, in late 2016, a new detector was commissioned to replace the old detector. It has been specifically optimised for  $^{53}\text{Mn}$  measurements, although the final design provides improved sensitivity for most isotopes. To maximise the sensitivity increases, this thesis attempts to optimise a variety of parameters associated with implementing the new detector through modelling and experiments. The final goal of characterising the performance increase of the new detector is partly achieved, but was limited by manufacturing delays and time constraints.

Chapter 2 introduces the experimental set-up for Accelerator Mass Spectrometry at the ANU, and introduces the analytic principles behind AMS analysis. It also develops a contextual understanding of the components that will be discussed in later chapters, including gas filled magnets and multi-anode ionisation chamber detectors.

Chapter 3 discusses the theoretical considerations behind stopping heavy ions in gases. In particular, Monte Carlo simulations are used to predict the behaviour of  $^{53}\text{Mn}$  and  $^{60}\text{Fe}$  beams inside the ANU gas filled magnet and the ionisation chamber. These predictions informed the design choices for the newly constructed detector.

Chapter 4 describes the operating features of the old detector and explains its deficiencies in detail. The analytic methods behind AMS data analysis are exhibited by the measurement of  $^{53}\text{Mn}$  and  $^{60}\text{Fe}$  ratio pairs for newly measured meteorites. This will contribute to meteorite studies through collaborations with several Swiss and German institutions.

Chapter 5 explains the design philosophies behind the construction of the new Flexible Anti-Scattering Multi-Anode (FASMA) detector and how they are motivated by solving the shortcomings of the old detector. Some preliminary measurements, which demonstrate the enhanced separation capabilities of the FASMA detector, are discussed, although many new features are still suffering teething issues. The full performance evaluation has been delayed beyond the time limit of this thesis; however, potential future improvements and directions are discussed.

Chapter 6 summarises the current work and reflects on future directions for the FASMA detector, and nuclear astrophysics with AMS as a whole.

### 1.2.1 Conventions

This thesis has departed from the typical format of background-experiment-discussion and has instead compartmentalised the relevant theory, work, and implications for various sections of the design process to better communicate the motivation behind each decision. Whilst the presentation is still approximately linear, please make use of the in-text hyperlinks to navigate the sections if concepts are not clear.

All quoted uncertainties are symmetric  $1\sigma$  confidence intervals, except when noted. All spectra produced by Analogue to Digital Converters (ADC) are 1024 channels in total.

---

# Accelerator Mass Spectrometry

---

According to Synal [33], there are four core principles behind effective Accelerator Mass Spectrometry (AMS) and each component contributes to one or more of these pillars. In particular, these principles are:

1. The suppression of nuclear isobaric ions. Nuclear isobars, nuclei with the same mass number, have only a small mass difference that cannot be resolved when the disturbing isobar is many orders of magnitude more abundant. High suppression rates by methods other than direct mass analysis need to be employed.
2. The suppression of equal mass molecules. Similar to nuclear isobars, molecules of equal mass, or the same mass-charge ratio, are many times more abundant and need to be suppressed.
3. Provide sufficient abundance sensitivity. Abundance sensitivity is the ability to separate beams of different isotopes, and for most AMS spectrometers this means a moderate mass resolution with  $m/\Delta m \approx$  several hundred.
4. Reliable normalisation procedure. Due to the complexity of all the filtering stages, extensive beam loss and mass fractionation effects can occur throughout the process. Therefore a reliable procedure to normalise the measured ratios is required.

These principles will guide the description of the ANU AMS facility and highlight the necessity of each stage.

Most AMS facilities share structural similarities but may differ slightly depending on the isotope of interest. Nearly all facilities use tandem accelerators (with the exception of new  $^{14}\text{C}$  single stage accelerators) so the most prominent distinction is the size of the accelerator used. Small and medium facilities (less than 3 MV) focus on the most widely used isotopes ( $^{14}\text{C}$ ,  $^{10}\text{Be}$ ,  $^{26}\text{Al}$ , etc.) as these are relatively easy to separate from interfering species. For the astrophysical isotopes, the AMS group at the ANU uses a much bigger 14UD pelletron tandem accelerator which can sustain terminal voltages over 14 MV. This provides the high energies required to separate the radionuclide from the interfering species.

In section 2.1 I will describe the beam line and apparatus used for AMS of  $^{53}\text{Mn}$  and  $^{60}\text{Fe}$  at the ANU. In section 2.2, I will explain the principles behind the gas-filled magnetic spectrograph used for isobar separation of  $^{60}\text{Fe}$  and  $^{53}\text{Mn}$ . In section 2.3, I will then outline the general principles behind multi-anode ionisation chamber detectors. The specific details of the ANU detectors will be left to Chapter 4 and Chapter 5 where they are covered in more detail. Finally, in section 2.4, I will outline the logic behind ratio measurements and how they are useful to the applications of AMS.

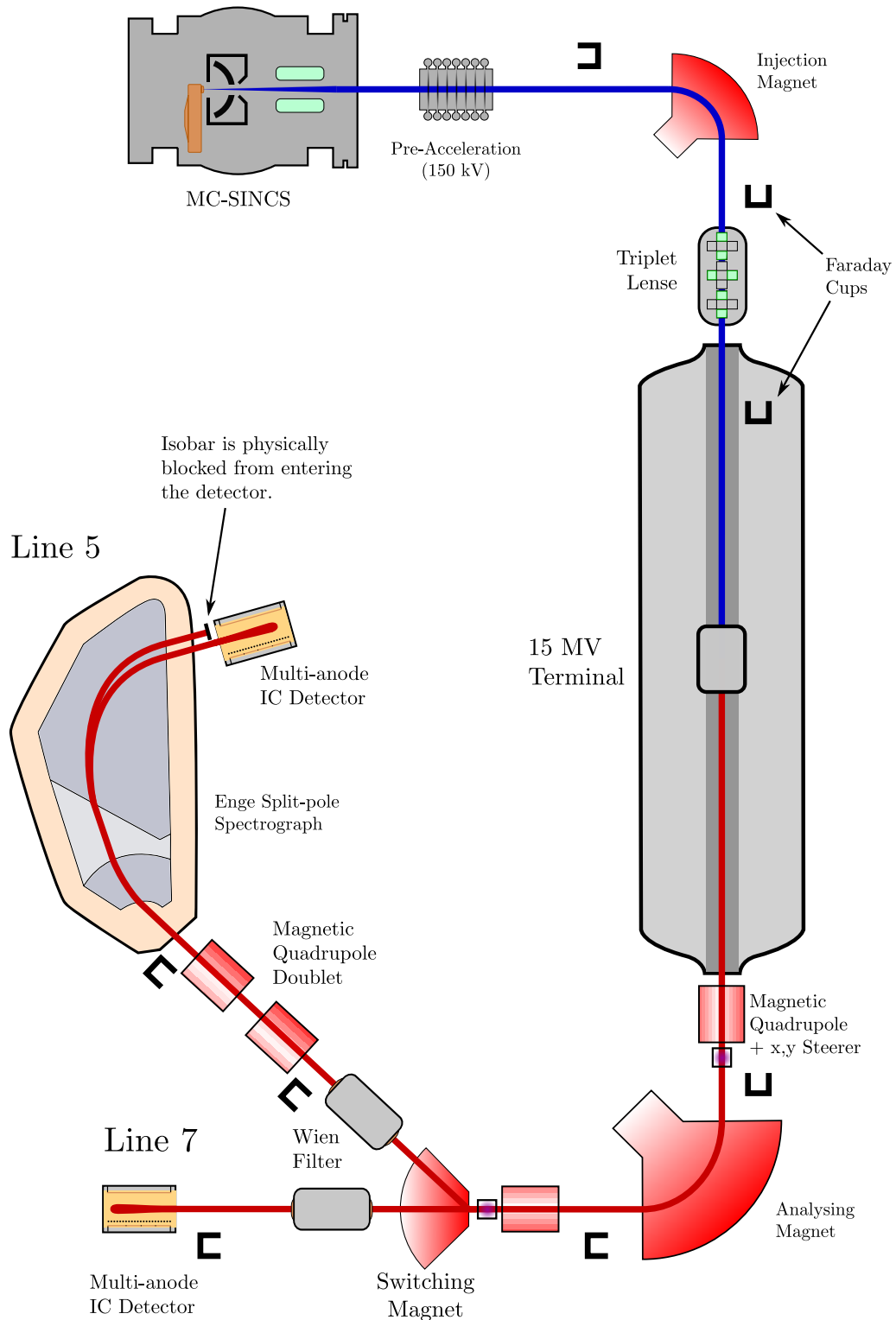


**Figure 2.1:** A full schematic of the AMS system based at the ANU's 14 UD tandem pelletron accelerator. Line 5 is used for  $^{53}\text{Mn}$  and  $^{60}\text{Fe}$ , along with many other isotopes, which we are primarily concerned with in this thesis. Line 7 is used for other isotopes like  $^{36}\text{Cl}$  and  $^{93}\text{Zr}$ . Note that the beam line angles are purely for formatting convenience. In reality line 5 bends  $10^\circ$  left and line 7 bends  $40^\circ$  left. This allows the switching to perform background filtering.

## 2.1 Principles of AMS Systems

All AMS systems share the same fundamental design, although the specific instrumentation can vary between institutions and isotopes. In this section, I will describe the five generalised sections of the set-up that are used at the ANU. Figure 2.1 shows a schematic representation of the 14 UD pelletron tandem accelerator at the ANU.

### 2.1.1 The Negative Ion Source

To analyse isotope ratios of  $10^{-12}$  or less, an intense ion beam is needed. This is provided by a Multi-Cathode Source of Negative Ions by Caesium Sputtering (MC-SNICS), see Figure 2.2. Caesium sputtering is almost exclusively used in AMS as it provides high-efficiency negative ion production, relatively stable beam currents, and short switching time of cathodes with a low source memory effect [33]. Caesium is chosen as the sputtering ion as it provides violent sputtering due to its relatively high mass, and is a good electron donor, which enhances the formation of negative ions.

The caesium is heated in a specialised oven to form a vapour that diffuses into the source to simultaneously bathe the ioniser and cathode in caesium gas. The ioniser is a hot spherical tantalum surface that is held at roughly  $1000^{\circ}\text{C}$ . Upon contact with the ioniser, the caesium gas forms  $\text{Cs}^+$  ions by surface ionisation, which are then accelerated toward the cathode. The sample powder is pressed into a small copper holder, which is loaded into a copper sample wheel that can hold 31 samples. The  $\text{Cs}^+$  ions are naturally focused by the immersion lens onto the sample, and the impact from the  $\text{Cs}^+$  ions sputters

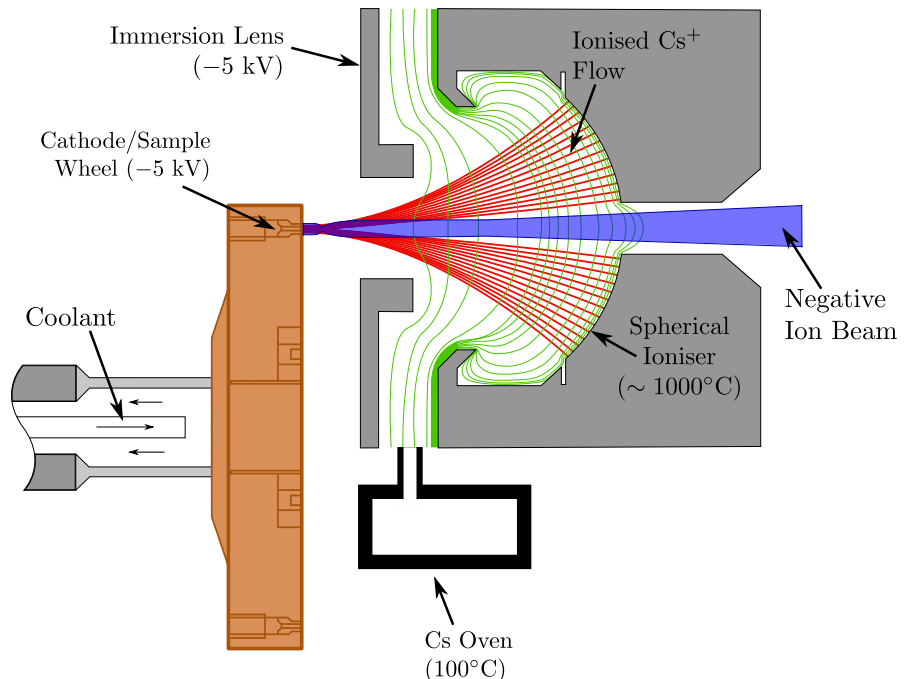


**Figure 2.2:** A schematic of the Multi-Cathode Source of Negative Ions by Caesium Sputtering (MC-SNICS). The hot caesium gas is ionised and focused onto the sample (red trajectories), which is sputtered out into the caesium gas. The caesium can also donate electrons to form negative sample ions (blue beam) that are accelerated away from the cathode and out of the source. Lines of equipotential, generated by the potential difference between the ioniser and immersion lens/cathode wheel, are plotted in green.

the sample into the chamber. The spherical ioniser and immersion lens combination was popularised after Han et al. [34] and Jackson et al. [35] demonstrated significant source output improvement over the original design by the National Electrostatics Corporation (NEC).

In the chamber, the caesium gas donates electrons to the sputtered source forming the desired negative ions. The cathode is also cooled, which promotes the formation of a thin layer of caesium on the cathode that greatly enhances the negative ion formation [36]. The negative ions are then extracted by repulsion from the cathode (held at  $-5\text{ kV}$ ) and the immersion lens (also held at  $-5\text{ kV}$  at the ANU).

In some cases, the formation of molecular negative ions can have advantages over atomic negative ions. The sample can be prepared in a multitude of molecular species, each with different advantages. Manganese does not form stable negative ions and so molecular ions must be used. Manganese oxide ( $\text{MnO}^-$ ) more readily forms negative ions resulting in higher source outputs; however, manganese fluoride ( $\text{MnF}^-$ ) suppresses production of the stable isobar, chromium. As a result, both molecules are used depending on the sensitivity required. For iron, the production rate of  $\text{Fe}^-$  is significantly lower than molecular species like  $\text{FeO}^-$ , which make molecules more favourable.

### 2.1.2 The Injection System

After extraction from the negative ion source, the beam undergoes pre-acceleration of 100–150 keV and electrostatic focusing. The isotope of interest is then selected for transport to the 14UD accelerator using a  $90^\circ$  injection magnet. As the initial beam has significant energy straggling (due to the sputtering tail) [33], the mass resolution is imperfect and many undesirable species will make it into the accelerator tube, including molecular species with the same magnetic rigidity as the desired nuclide. To maximise beam transmission, we do not use narrow apertures to limit the interference but rather rely on the separation resolution of the analysing magnet.

As AMS determines isotope ratios, the stable isotope needs to be measured in addition to the radioisotope. At the ANU, we change the injection magnet to alternate between species in  $^{53}\text{Mn}$  and  $^{60}\text{Fe}$  measurements as we have not yet implemented fast-switching pre-acceleration facilities. Since the stable beam can be as high as  $100\text{ }\mu\text{A}$ , we regularly need to use a chopper to reduce the beam load on the accelerator as large beam loads causes the terminal voltage drop because the charging chains are unable to carry away the build up of negative charge. The chopping mechanism applies an electric field to the beam that deflects it, stopping it from entering the accelerator tank. The rise and fall time of the chopper is approximately 50 ns compared to the  $10\text{ }\mu\text{s}$  injection interval and the  $200\text{--}1000\text{ }\mu\text{s}$  exclusion interval, depending on the attenuation required. This ensures the charging system can maintain the required voltage and produce highly reproducible chopping factors.

### 2.1.3 Acceleration and Stripping

The accelerator itself is a 14 UD pelletron tandem accelerator. Two accelerations stages are provided, the first on the low energy side where single charged negative ions are accelerated towards the terminal that is held at a high positive potential. In the terminal, electrons are stripped to form positively charged ions that are accelerated away from the terminal on the high energy side. The terminal can be charged up to 15.5 MV using the pelletron charging chains, which are significantly better at holding a stable voltage than rubberised

charging belts [8]. Since the beam current for the radioisotope is rarely measurable, beam feedback systems cannot be used to keep a stable terminal voltage. Instead, a generating voltmeter (GVM) is used, which measures the current induced by the varying capacitance produced by periodically shielding the stator component from the terminal voltage with a rotating plate [37]. Hence, the current measured is proportional to the terminal voltage which can be adjusted very accurately. The stability of the terminal under the GVM is approximately  $\pm 1$  kV or better for typical 14 MV operating conditions.

Two stripping processes are available to ionise the beam for the high energy side, gas stripping and foil stripping, and the optimal choice depends on the beam species and the energy needed. The stripping system is pictured in Figure 2.3. The gas stripper is a stainless steel tube (852 mm long, 4 mm radius) where gas is cycled by two turbo pumps. The gas is restricted from escaping into the accelerator tubes by two additional low-conductance tubes (42 mm long, 4 mm radius), which are differentially pumped by two ion pumps to produce a pressure impedance [9]. This ensures minimal impact on the vacuum in the accelerator tubes. Pressures in the stripper are approximately 2-30 mTorr. The effective thickness under gas stripping is usually smaller than a foil, which produces a lower charge state distribution (resulting in lower energies), but also decreases the angular scattering. Since less scattering increases beam transmission, gas stripping is used in most AMS measurements.

The foil strippers are thin carbon foils ( $4 \mu\text{g cm}^{-2}$ ) that are held in a local adaptation of an NEC multi-foil changer. If high energies are needed, then foil stripping is optimal as it produces a much higher charge state distribution than gas stripping. However, foil stripping has three disadvantages: firstly, the foils thicken under bombardment of heavy ions; secondly, they have short life times for heavy mass or high intensity beams and are prone to tearing; and thirdly, they introduce more scattering which reduces the transmission [9].

Many AMS isotopes require the use of a molecular negative ion, including  $^{53}\text{Mn}$  and  $^{60}\text{Fe}$ . In this case foil stripping generates an effect known as the *Coulomb explosion*. When the foil strips the molecule of electrons, the stripping is effectively instantaneous so the components are left positively charged at essentially molecular separation, which causes a strong Coulomb repulsion. As the bonding axis is random, the Coulomb explosion adds both an energy spread and an angular spread to the beam. When high energies are still required (as for  $^{53}\text{Mn}$  and  $^{60}\text{Fe}$ ), the solution is to use a combination of gas and foil stripping such that the molecule can dissociate in the gas, and then the separated constituents will be stripped to a higher charge state by the foil. This method achieves the high charge state distribution whilst minimising the energy spread.

In addition to forming positive ions, the stripping process also dissociates any molecules with the same magnetic rigidity as the radioisotope such that the possibility of transmission through the analysing magnet is significantly reduced. This effect is so useful that in the early times of AMS, it was considered a ‘golden rule’ to use ions in a charge state of 3+ or more to completely remove molecular interferences [33].

#### 2.1.4 High Energy Mass Analysis

Upon exiting the terminal, the beam has been stripped stochastically to form a charge state distribution. Only one charge state for the beam species of interest can be selected by the analysing magnet. For isotopes which do not require high energies, the transmission fraction is the most crucial. However, for isotopes like  $^{53}\text{Mn}$ , high energies are required for single ion detection; hence there is a trade off between higher charge states (higher

energies) and the population of that charge state. For example, charge states of +12 or +13 are typically used for  $^{53}\text{Mn}$ , depending upon the ratio of the sample.

The analysing magnet selects atomic ions with the correct  $mE/q^2$  ratio and has enough mass resolution to select only the isotope of interest. Charge exchange can occur between molecular remnants and the residual gas in the accelerator tubes which can cause other species to pass the analysing magnet. To remove this interference, each beam line has a *Wien filter*, which is a velocity filter that selects ions with a given mass-charge ratio. An electric field is positioned perpendicular to a magnetic field, both normal to the beam direction, such that the Lorentz force from both fields adds to zero for the desired velocity:  $F_L = q(E - vB) = 0$ . Thus, if the velocity (equivalently the mass-charge ratio) is not correct, the particle will be deflected and not make it to the detector.

### 2.1.5 Single Particle Detection

There are a multitude of ways to detect the particle after acceleration. These include silicon detectors which provide total energy measurements, and ionisation chamber detectors that can provide energy loss measurements. Time-of-flight detectors, which are isotopic filters, are also used for heavier isotopes, like actinides, that are not effectively separated by the

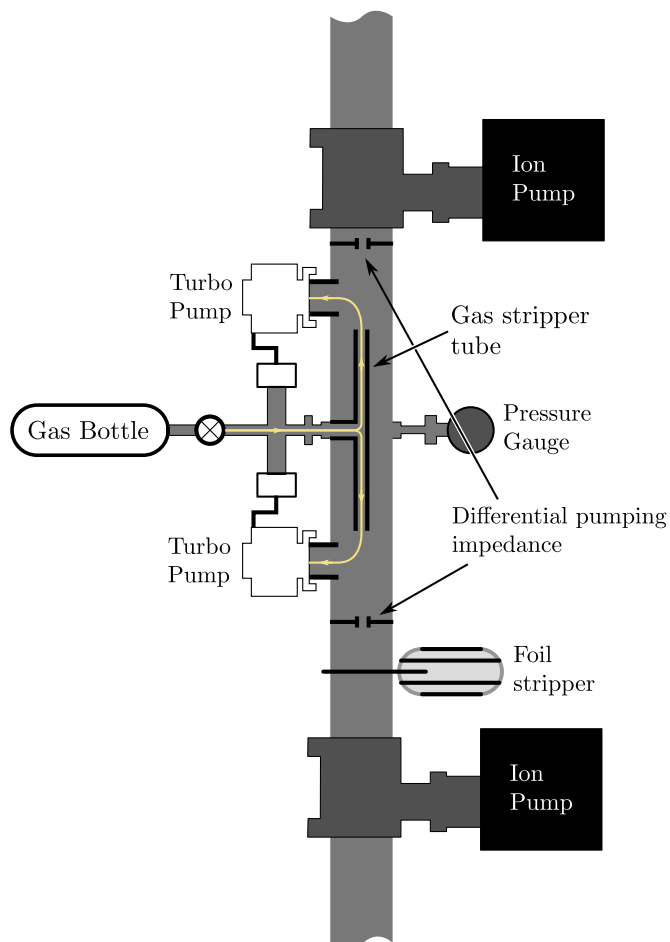


**Figure 2.3:** The stripping system used at the 14 UD tandem accelerator, adapted from Gladkis [9]. The gas is circulated through the turbo pumps whilst the ion pumps ensure any gas escaping does not enter the accelerator tubes.

Wien filter. However the main problem faced for  $^{53}\text{Mn}$  and  $^{60}\text{Fe}$  detection is the presence of *stable isobars*. Isobars are nuclei with the same mass number and in this case, there exist naturally occurring stable isobars of our radioisotopes that, even at trace background levels, can be over a billion times more abundant than the radioisotope itself. For  $^{53}\text{Mn}$  and  $^{60}\text{Fe}$ , these isobars are  $^{53}\text{Cr}$  and  $^{60}\text{Ni}$  respectively. The isobars will be stripped to have their own charge state distribution that will overlap with the radioisotope charge state, and as a result the isobars will have the same mass-charge ratio as the desired radioisotope. The mass difference between the isobars –  $0.012\% \Delta m/m$  for  $^{53}\text{Mn}-^{53}\text{Cr}$  and  $0.055\% \Delta m/m$  for  $^{60}\text{Fe}-^{60}\text{Ni}$  – is too small for high-resolution magnetic separation when the isobars are many orders of magnitude more abundant. Consequently, the trajectories that they will follow through the analysing magnet and the Wien filter will be indistinguishable from that of the radioisotope. Hence, they will also make it to the particle detection stage.

Isobars are, however, different elements and will deposit energy at different rates in matter. Multi-anode gas ionisation chamber detectors can potentially measure this difference in energy deposition and separate the isobar counts from the radioisotope counts. In some cases, like  $^{53}\text{Mn}$  and  $^{60}\text{Fe}$ , the isobar flux may be so high that the isobar causes significant deadtime in the detector, resulting in pileup of counts. In this case, a gas-filled magnet is used to physically separate and block the isobar from entering the detector. The gas-filled magnet and multi-anode ionisation chambers will be discussed in detail in section 2.2 and section 2.3 respectively.

## 2.2 Gas-Filled Magnet

In a standard magnetic spectrograph, the ion beam experiences the Lorentz force from a magnetic field  $B$  perpendicular to its motion, which generates a centripetal force resulting in circular motion. Supposing the particle has energy  $E$ , mass  $m$ , and occupies the charge state  $q$ , the radius of gyration  $\rho$  is given by:

$$\rho = \frac{\sqrt{2mE}}{qB}. \quad (2.1)$$

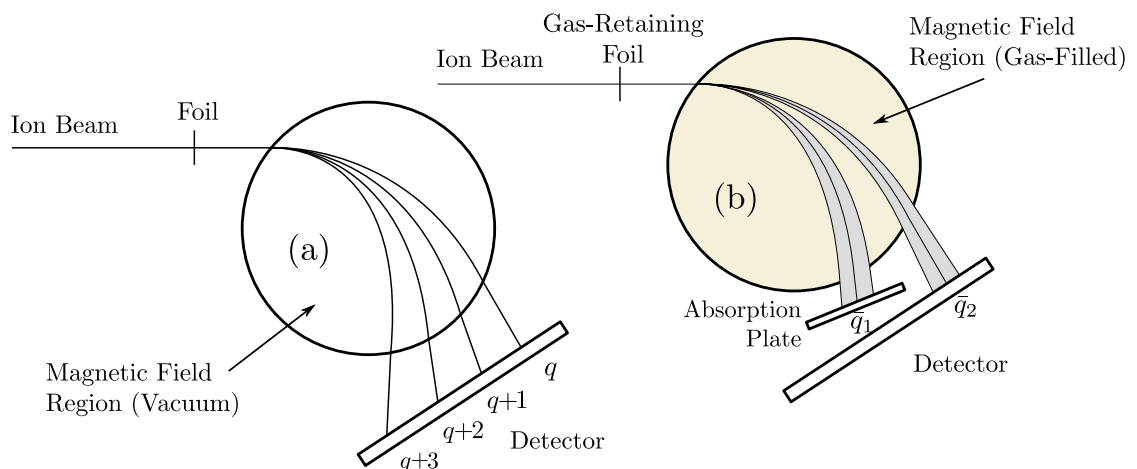


**Figure 2.4:** Illustration of ion trajectories in: (a) vacuum; and (b) a gas. In the gas-filled magnet, the trajectories coalesce around a mean charge state due to successive charge-changing collisions. This figure is adapted from Paul et al. [38].

For an ion beam of identical mass and energy, passing through such a magnetic field will split the beam into any constituent charge states, as seen in frame (a) of Figure 2.4.

However, if the section under the magnetic field is filled with a low pressure gas, then the ions will undergo a series of electron capture and loss collisions, which will change their charge value through the gas. Over many collisions, they will form a mean charge state, which will determine the trajectory of the species. The equations governing these collisions are covered in great detail in Betz et al. [39]. A simpler, more commonly used, semi-empirical relation for the mean charge state in dilute light gasses is given by Sayer [40]:

$$\bar{q} = Z_P \left( 1 - 1.08 \exp(-80.1 Z^{-0.506} \beta^{0.996}) \right), \quad (2.2)$$

where  $Z_P$  is the projectile atomic number and  $\beta = v/c$  is the normalised velocity term. From Equation 2.2, it is evident that the mean charge state depends on the atomic number; thus, a separation of isobars can be generated by passing the beam through a gas-filled magnet, as visualised in part (b) of Figure 2.4.

As Equation 2.2 is velocity dependent, this separation will change with the energies of the particles. Equation 2.2 has been plotted in Figure 2.5 for  $^{53}\text{Mn}$  and  $^{53}\text{Cr}$  to demonstrate this energy dependence. Since the difference in mean charge state is approximately constant, the separating power remains constant throughout the gas-filled magnet, although the radius of the trajectory will increase with a decreasing mean charge state. The arrows in Figure 2.5 indicate typical entry and exit energies for the gas-filled magnet at the ANU. Note that the exit arrows do not align; this is because  $^{53}\text{Cr}$  loses  $\sim 2$  MeV less energy than  $^{53}\text{Mn}$  due to its lower atomic number.

The difference in the mean charge state between isobars will produce a physical separation upon exit of the magnet region that can be used to suppress the unwanted isobar. The power of this suppression is mainly dependent on the planar spread of the beam. Paul et al. [38] have suggested that the width is controlled by two competing factors. A

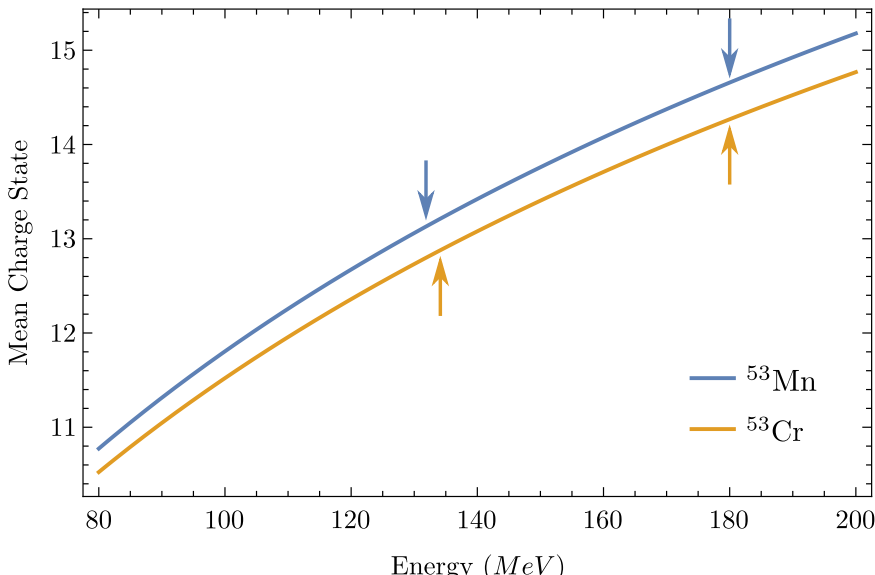


**Figure 2.5:** The mean charge state of  $^{53}\text{Mn}$  and  $^{53}\text{Cr}$  over a suite of energies, calculated from Equation 2.2. The arrows mark example energies of the isobars when the beam enters the ANU gas-filled magnet and when it enters the detector. This figure was adapted from Gladkis [9].

higher pressure will induce more interactions resulting in a more stable mean charge state, which will reduce the beam width due to fewer fluctuations away from the mean charge trajectory. On the other hand, a higher pressure will also increase width broadening due to angular and energy loss straggling. Balancing these competing factors results in an optimum pressure for operation of the gas-filled magnet. This pressure is dependent on the beam species.

### 2.2.1 Isobar Suppression

It is important to understand the purpose of isobar suppression to appreciate fully how best to utilise a gas-filled magnet to improve a measurement. The purpose of the isobar separation is not to maximally suppress the stable isobar, but rather to allow a sufficiently low amount of the stable isobar into the detector such that the measurement can be made. Ionisation chamber detectors (discussed in section 2.3) used for AMS are limited to about 2000 counts per second before significant dead time and pileup interferes with the separation capability of the split anodes. It is essential that the count rate, which consists mostly of the stable isobar, be limited to suitable levels.

If the sample ratio is high, the good radionuclide counting statistics can still be achieved, even with poor isobar suppression, by reducing the source output or moving the beam out of the detector. Then the energy available should be prioritised for separation by energy loss in the detector. If the sample ratio is low, however, then excellent isobar suppression is crucial to maintain an appropriate count rate, as the source output needs to be high and the majority of the radioisotope beam needs to be in the detector for decent counting statistics to be achieved. In this case, a significant portion of the available energy needs to be committed to isobar suppression to make the measurement possible at all. In short, the goal for operating a gas-filled magnet is to achieve the required level of isobar suppression whilst maximising the energy available for the detector.

### 2.2.2 The ANU Enge Split-Pole Magnetic Spectrograph

The ANU operates a gas-filled Enge split-pole magnetic spectrograph on beam-line 5, pictured in Figure 2.7, for isobar suppression of  $^{60}\text{Fe}$ ,  $^{53}\text{Mn}$ ,  $^{32}\text{Si}$  and other isotopes. The split-pole spectrograph was originally designed for nuclear spectroscopy, in particular nuclear reaction studies [41]. The Enge split-pole spectrograph consists of two separate poles enclosed by a single power coil, as pictured in Figure 2.6. The particular shape and splitting of the poles is designed to achieve second-order double-focusing over the focal plane. Due to the shape and splitting of the poles, there are several sections where the beam travels under little or no magnetic field. These include the field clamp, the gap between the poles, and between the pole and the detector. The result is that the beam does not spend its entire trajectory under full magnetic field, although the exact percentage depends on the positioning of the detector and the gyromagnetic radius. Angular and energy loss straggling still occurs in these regions, which degrades the beam width with no gain in separation.

The gas used at the ANU is standard nitrogen gas ( $\text{N}_2$ ). This choice was motivated by the results of Knie et al. [42] where hydrogen, helium, nitrogen, argon, methane, and isobutane were all tested at different pressures to determine the optimum resolution. The optimum pressure for isobar separation is slightly more complicated and will be discussed in section 3.2

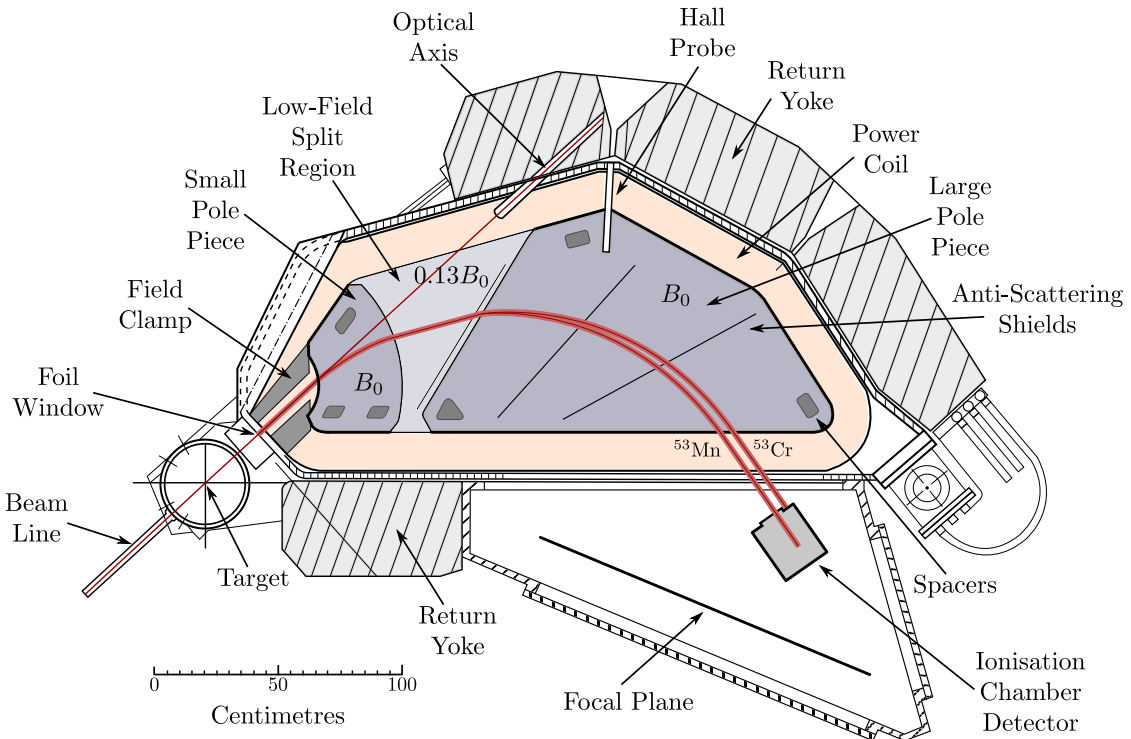


**Figure 2.6:** A schematic top view of the Enge split-pole spectrograph [41], adapted from Paul et al. [38]. The magnet and detector chamber region is filled with low pressure nitrogen gas (typically 3.5 Torr). Approximate trajectories for  $^{53}\text{Mn}$  and  $^{53}\text{Cr}$  are shown demonstrating the isobar separation of the spectrograph.

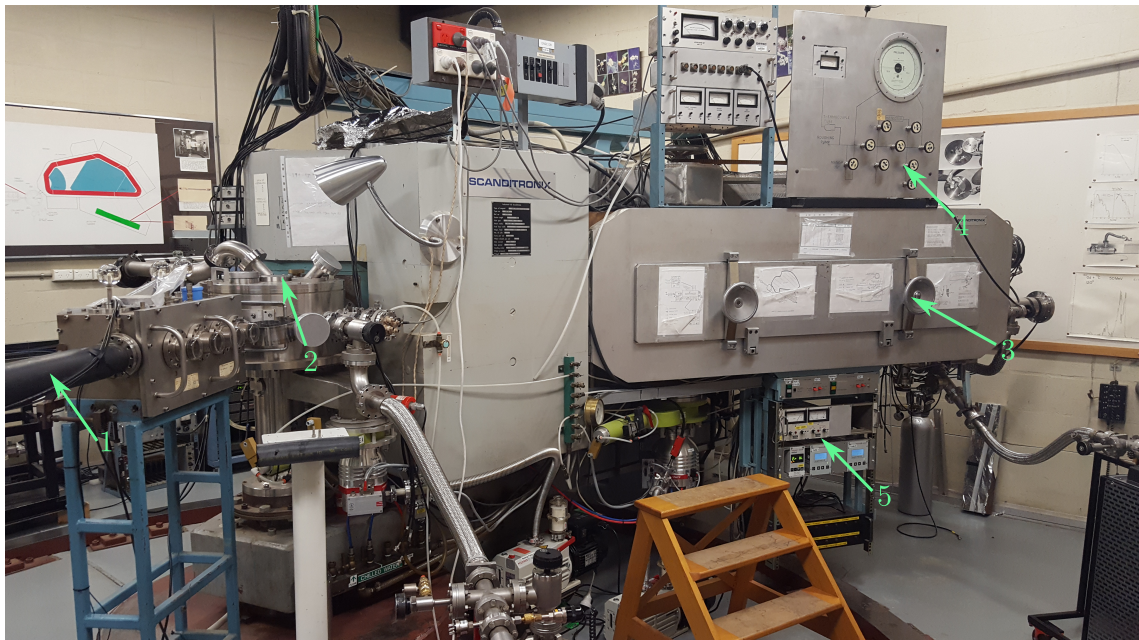


**Figure 2.7:** Photograph of the Enge split-pole spectrograph at the ANU. 1: Incident beam line. 2: Target chamber. The chamber is empty and the Mylar foil is located at the exit. 3: Detector housing. 4: Gas handling system for Enge and detector. 5: Vacuum control systems.

## 2.3 Multi-Anode Ionisation Chamber Detector

This thesis is primarily concerned with the construction and characterisation of a new multi-anode ionisation chamber detector for AMS at the ANU. Extensive technical coverage is given for both the old detector and FASMA detector designs in section 4.1 and section 5.2 respectively. In this introductory section, I will only describe the general principles behind multi-anode ionisation chamber detectors.

For over a century, ionisation chambers have been used to measure ionising radiation [43]. The simplest version has two parallel electrode plates, oppositely charged, fixed in a chamber full of gas. The electrodes produce a constant electric field throughout the chamber such that when a heavy ion enters the chamber, any ionising collision with the gas will separate the electron-ion pair and accelerate them towards their respective electrodes. The electrons induce a measurable signal on the anode that is recorded. Typically, an energy of 25–35 eV is needed to create an ion pair [44], although the first ionisation potential is roughly 20 eV less. As a result, approximately 6 million ion pairs will be formed in stopping a 180 MeV ion.

Assuming the gas is inert such that it does not readily form negative ions, the electron signal can be integrated and shaped such that the signal size will be proportional to the primary ionisation, and thus the energy loss of the ion. As visualised in Figure 2.8, the drift velocity for the electrons is approximately 1000 times faster than the atomic target ions due to their much smaller mass. For typical gas pressures and electric field strengths, the drift velocity in isobutane is around  $50 \text{ mm } \mu\text{s}^{-1}$  [45]. This means that the electrons are quickly removed from the gas volume resulting in minimal detector deadtime and high count rates.

### 2.3.1 Frisch Grid

The rise time of the signal on the anode depends on the drift velocity of the electrons, whilst the amplitude of the signal depends on the distance between the creation site of the electron-ion pair and the anode [46]. Since we want the amplitude to be proportional to the energy loss, the variation due to the height of the creation site below the anode, caused by the vertical spread of the incoming beam, needs to be eliminated. This is done by the introduction of a *Frisch grid* which is a series of thin wires, held at an intermediate potential between the point of ionisation and the anode. The Frisch grid is held at an independent voltage to the anode and so shields the anode from the creation of any mirror charges until the electrons drift past the Frisch grid [44]. As a result, all the induced charges on the anode appear at the same height (the grid height), removing the influence of the position of the pair production site. In addition to this, the Frisch grid also shields the anode from the positive ions travelling to the cathode, resulting in a more stable signal.

The Frisch grid also allows different field strengths to be applied between the anode-grid region and the cathode-grid region. This means different drift velocities can be selected for separate parts of the detector volume. These values are important to achieve optimal energy resolution in the detector as the field strengths are a compromise between many parameters including maximum anode voltage, shaping time, and recombination probability [46]. This optimisation will be discussed in more detail in subsection 5.2.2.

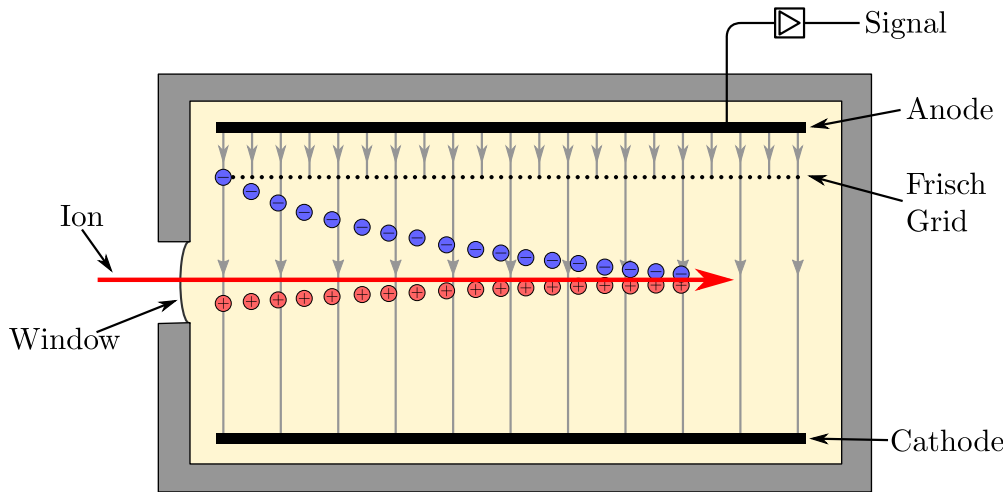


**Figure 2.8:** The working principle behind an ionisation chamber detector. The charges created from the ion stopping interactions induce a signal in the electrodes. Note that in reality, ion stopping occurs over much faster time scales than the electron drift velocity such that the electrons all drift upward together. This figure is adapted from Martschini [47].

### 2.3.2 Anode Splitting

A standard ionisation chamber is not particularly useful for isobar discrimination as the isobars have the same energy. However, as they have different atomic numbers, they have different energy loss profiles and will deposit different amounts of energy throughout the detector (for specifics on energy loss, see section 3.1). This variable energy loss is depicted in Figure 2.9 for  $^{53}\text{Mn}$  and  $^{53}\text{Cr}$ . If the anode is split at certain depths along the beam path, the isobars will deposit different amounts of energy on each split anode and the signals can be used to create multidimensional spectra that are used to separate the isobars. The magnitude of the separation in these spectra is obscured by the energy width of each species. There are many factors that contribute to the energy resolution in the detector, including the beam width from the accelerator, the angular and energy straggling from the gas-filled magnet and windows, and the intrinsic electronic noise, just to name a few. Energy resolution is discussed in detail in subsection 5.2.4.

In addition to simple depth segmentation, each individual anode can be split diagonally to gather information on scattered projectiles [48]. Depending on the position of entry, different amounts of energy will be deposited on each triangular anode due to their asymmetric geometry. Given the isobars are separated in position space by the gas-filled magnet, this can provide another gate for discriminating between the isobars. The initial designs for the new anode configuration will feature two diagonally split anodes, which will give two points of position data that can be used to determine the angle of the trajectory. This information can be used to disregard highly scattered particles that are notorious for generating long tails in the energy spectra. More details of the new anode splitting design for the FASMA detector can be found in subsection 5.2.1.

### 2.3.3 Detector Gas

The main requirement for the target gas in an ionisation chamber is that it does not readily form negative ions that could give false signals at the anode. There are many candidates that satisfy this requirement. Previously at the ANU, propane ( $\text{C}_3\text{H}_8$ ) has been used

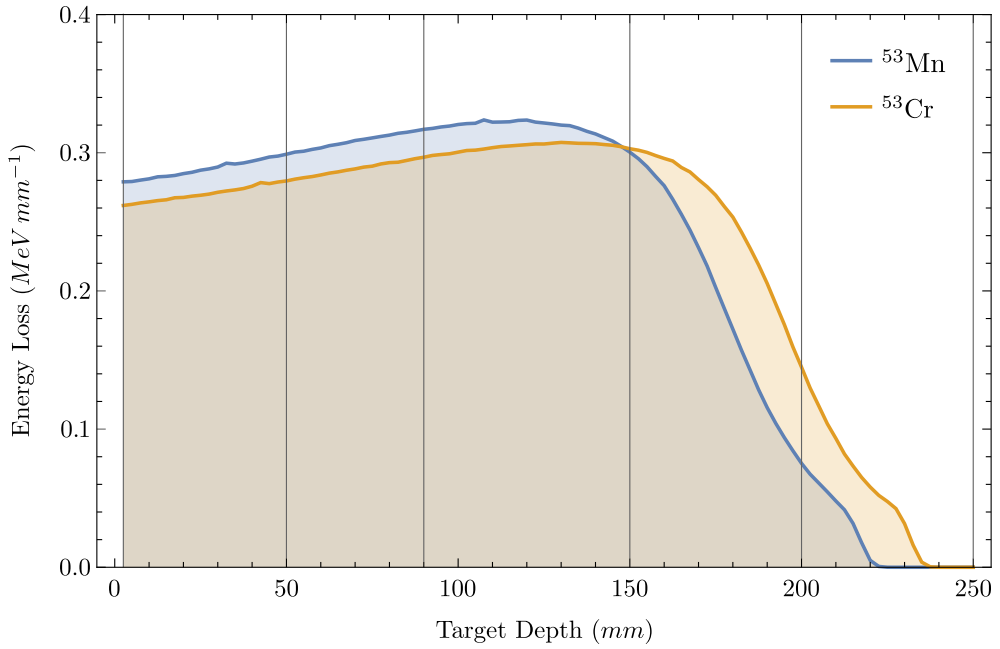


**Figure 2.9:** The energy loss of  $^{53}\text{Mn}$  and  $^{53}\text{Cr}$  ions due to ionisation as a function of the distance travelled in 34.5 Torr of isobutane gas. The average energy entering the detector is 132 MeV for  $^{53}\text{Mn}$  and 134 MeV for  $^{53}\text{Cr}$ . These curves were produced by a SRIM simulation, see section 3.3 for more details.

as the target gas due to its low price and commercial availability. Recently, isobutane ( $\text{C}_4\text{H}_{10}$ ) has replaced it due to its higher stopping power, which allows for lower detector pressures to stop the incoming beam fully. This reduces the outward bowing of the detector entrance foil. As the beam has vertical and horizontal distributions, this bowing can generate different path lengths through the detector gas contributing to energy straggling. Thus, obtaining a lower detector pressure means isobutane should have improved energy resolution over propane.

It is also important to keep a stable pressure in the detector such that each ion has a consistent energy loss profile. Currently, the ionisation chambers at the ANU are filled to the required pressure and then isolated to maintain a constant pressure. This relies on negligible detector leakage, which can be challenging to achieve. Other detectors operated without the access restrictions of the Enge use a gas cycling system to maintain a stable pressure and provide new gas consistently.

Ionisation chambers also exhibit a non-linear signal decrease for heavier species. For a given ion energy, the pulse amplitude decreases with increasing atomic number. This effect is known as the *pulse height deficit* and introduces a species dependence on the energy deposited in the detector. The pulse height deficit is caused by increased cross sections of non-ionising energy loss and multiple ionisation of individual target atoms, which increases with the proton number. Weijers et al. [49] predict that for ions with atomic number around 24-28 at energies of 130 MeV, the pulse height deficit is about 5%. However the deficit between isobars is much smaller so energy calibrations will work for both species. Furthermore, any isotopic fractionation will be cancelled out since the standard sample experiences the same effect, as described in subsection 2.4.1.

## 2.4 Ratio Measurements

Generally, the aim of an AMS measurement is to acquire the ratio of the long-lived radionuclide to its stable isotope. For manganese, this is the  $^{53}\text{Mn}/^{55}\text{Mn}$  ratio, and for iron, this is  $^{60}\text{Fe}/\text{Fe}$ .<sup>1</sup> This section will describe how these ratios are determined and how they are used.

### 2.4.1 Normalisation Procedures

In AMS, the radioisotope is directly counted by the detector. The stable isotope is typically  $10^{12}$  time more intense [8] so the beam is measured as an electrical current in a Faraday cup. As the charge state selected is known, the number of ions (and hence the ratio) in the beam can be determined. Due to the possibility of beam losses or mass fractionation at each stage of the filtering process, the stable isotope current is usually measured after the analysing magnet.

Most purpose built AMS systems, of which the ANU is not one, utilise a fast-cycling mechanism such that the stable isotope can be measured during the measurement to keep track of any variations in the source output. This can be done either by changing the field of the injecting magnet or by changing the amount of pre-acceleration used after the source. Typically, the latter is used as switching times down to microseconds can be achieved by changing the applied voltage [8]. Note that whilst this allows the different isotopes to be injected into the accelerator, the terminal voltage and analysing magnets are usually kept constant due to the comparatively long charging times and hysteresis in the analysing magnet. Thus Faraday cups are positioned off the beam axis to catch the stable isotopes as they are ejected at different angles. Facilities which are shared for nuclear physics research have in general not been modified for fast-cycling and instead are obligated to change the field of the injecting magnet. A potential alternatively is to ‘bounce’ the injection and analysing magnets with a bias voltage, however this is avoided because of the impact it would have on proximal equipment needed by the nuclear physics groups. There are some preliminary plans to implement fast-cycling for  $^{53}\text{Mn}$  and  $^{60}\text{Fe}$  at the ANU; however, at the time of this thesis, they have yet to be implemented. Simultaneous injection was also investigated during the early 1990s [50], but they are not common today due to their incompatibility.

Regardless of the methodology for measuring the stable isotope current, the ratio measured is not the absolute ratio; there are several processes that lead to alterations of the initial isotopic ratio. The efficiency of charge state population during the stripping process is isotopically dependent, the beam transport is not necessarily identical and fractionation may also occur during negative ion formation [33]. This is in addition to the difficulties present in isobar separation, discussed in the next paragraph. To solve these problems, standard samples with well-known isotopic compositions are used to obtain renormalisation factors for the measured samples. Because any beam losses or fractionation effects are applied identically to both the standard and unknown samples, this has the added benefit of cancelling out any systematic errors present in the measurement of absolute values. Note that the standard samples should be prepared using the same chemical analysis as the real samples to replicate any systematic errors in the sample processing.

The renormalisation using standard samples is particularly helpful during isobar sep-

---

<sup>1</sup>For iron, the measured ratio is  $^{60}\text{Fe}/^{54}\text{Fe}$  due to the similar terminal voltages used. The  $^{60}\text{Fe}/\text{Fe}$  can be derived using the natural abundance of each stable isotope.

aration in the detector. For particularly difficult radioisotopes (like  $^{53}\text{Mn}$  and  $^{93}\text{Zr}$ ), the energy separation in the spectra from the multi-anode ionisation chamber may be insufficient to overcome the energy spread of the stable isobar causing the radionuclide and interfering isobar peaks overlap. In this case, a region of interest (ROI) can be specified that excludes any interfering isobar counts, even if this ROI only accounts for a fraction of the total radioisotope counts. As long as the standard sample has the same ROI applied during the data analysis, the measured sample can be renormalised to give the absolute ratio. For more sensitive ratios (less than  $10^{-12}$ ), excluding a significant proportion of the radionuclide counts may introduce untenable levels of uncertainty due to counting statistics. On the other hand, this process of renormalisation makes many radioisotope measurements possible that would not be possible without standard samples.

To help design the aforementioned region of interest and provide information on the associated background counts, blank samples that have been shielded from radioactivity and contain negligible levels of the radioisotope are also tested. This provides an easy way of determining a vastly complicated set of uncertainty factors associated with the AMS analysis and any induced signal in the sample preparation. Thus, the blank measurement provides a minimum detectable sensitivity associated with a given measurement process, as the exact set-up changes with each run.

The renormalisation process is also essential in generating reproducible results. Because the measured ratios are so low, otherwise negligible factors like the external temperature can significantly impact the reported values. Renormalisation with standard and blank samples are crucial in eliminating these systematic errors and ensuring that the results are not only reproducible across facilities but between individual runs. In addition, optimising the count rates in the detector, not just the current into the Faraday cup, is crucial for reproducibility of  $^{53}\text{Mn}$ . Many of these reproducibility conditions are isotope dependent and require specific routines at individual facilities.

#### 2.4.2 Ratio Applications

The ratio of the radionuclide to its stable isotope can be used in a variety of different ways to reveal information about physical processes. The most famous and commonly used method is for dating. If a physical process induces a constant abundance of the radioisotope, then the ratio can be used to determine the time of isolation from this physical process. The most obvious example is carbon dating where  $^{14}\text{C}$  is consistently produced by cosmic rays in the upper atmosphere and is then well mixed throughout living organisms during respiration. Upon death, the animal stops taking in  $\text{CO}_2$  and thus the  $^{14}\text{C}$  decays. Knowing the background ratio, the present ratio, and the half-life of  $^{14}\text{C}$  (5730 years), the sample can be dated. Exposure dating with  $^{10}\text{Be}$ ,  $^{26}\text{Al}$ , and  $^{36}\text{Cl}$  instead utilises the build up of the radionuclide over time. These isotopes are produced by exposure to cosmic-ray secondaries (neutrons, muons) in surface rocks [51]. When geological processes shift a rock face to the surface, the constant accumulation of the radionuclide allows the date of exposure to be determined.

If the date of the sample is already known, then the ratio can give information on the formation of the radioisotope. The most relevant example is the search for near-Earth supernovae [18], discussed in subsection 1.1.2. In this case, the sediment samples are dated using  $^{10}\text{Be}$ . From there, the ratio determines the amount of  $^{60}\text{Fe}$  in the sample leading to the deposition rate onto the Earth at the time.

Ratio measurements can also be used to determine the half-life of a given radionuclide.

---

For example, in 2009 Rugel et al. [31] re-examined the half-life of  $^{60}\text{Fe}$  using decay counting and found a significant departure from the previously reported value (by a factor of 1.8 and over 4 standard deviations). To provide discrimination between the two half-life measurements, Wallner et al. [32] used AMS measurements to measure the half-life of  $^{60}\text{Fe}$ . To do this, they measured the ratio of  $^{60}\text{Fe}/^{55}\text{Fe}$  and then the ratio of  $^{55}\text{Fe}/\text{Fe}$ . Since the half-life of  $^{55}\text{Fe}$  is well known, they were able to use the  $^{55}\text{Fe}$  standards to determine the half-life of  $^{60}\text{Fe}$  without making absolute measurements. Evidently, the ratio determined by AMS is useful in a variety of contexts.

---

# Simulating Ion Stopping

---

The physics of ion stopping is a rich and complex field that began over a century ago and continues today. Ziegler et al. [52] provide a comprehensive review of the field in the tutorial tome for their famous program, The Stopping and Range of Ions in Matter (SRIM) [53]. In this chapter, I will cover some basic formulae and definitions for ion stopping, focusing mainly on energies around  $1 \text{ MeV u}^{-1}$ , which are considered high but are the most relevant for Accelerator Mass Spectrometry (AMS). I will then focus on the Monte Carlo simulations that I used to predict the behaviour of the Enge gas filled magnet and the ionisation chamber detector itself. These simulations enabled me to optimise several characteristics of the detector set-up that we would be unable to measure otherwise.

## 3.1 Energy Loss in Matter

A kinetic, charged particle will decelerate in matter by distributing energy through a large number of Coulomb interactions with the atoms of the target. Due to the sheer number of interactions, this energy loss can be approximated as a continuous function known as the *stopping power* (also called the *specific energy loss*) [44],

$$S(E) = -\lim_{\Delta x \rightarrow 0} \frac{\Delta E(E)}{N \Delta x} = -\frac{dE(E)}{dx}. \quad (3.1)$$

In Equation 3.1,  $\Delta E$  is the average energy loss over a depth interval  $\Delta x$ . The denominator  $\rho_A = N \Delta x$ , is known as the *areal density* (typically given in  $\text{mg cm}^{-2}$  for gas targets) and it allows us to neglect any differences in density and geometry between targets and instead focus on the energy loss properties.

The stopping power is the combination of both electronic stopping, due to Coulomb reactions with the target electrons, and nuclear stopping, due to Coulomb reactions with the screened nuclear charge of the target atoms [52]. Figure 3.1 shows both the electronic and nuclear stopping for  $^{53}\text{Mn}$  into 34.5 Torr of isobutane. For energies above 1 MeV, electronic stopping dominates and produces the majority of the energy separation recorded in ionisation chambers.

### 3.1.1 Electronic Stopping Power

It is difficult to get a uniform description of electronic stopping, as many factors only occur in specific energy ranges or beam-target combinations. The key parameter is the particle's velocity. For fully stripped particles, the model put forward by Bethe [54] and Bloch [55]

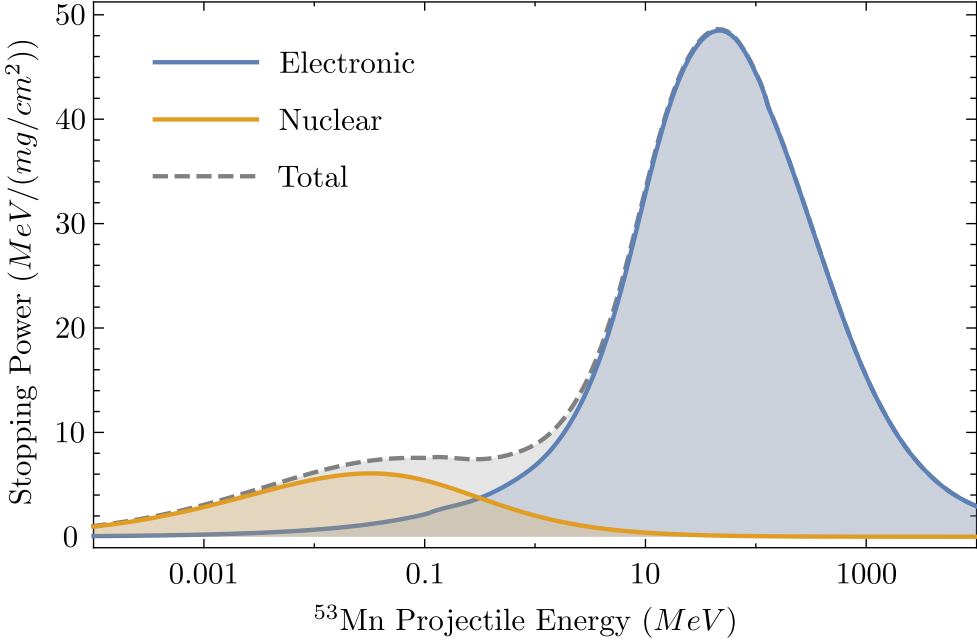


**Figure 3.1:** The stopping power of  $^{53}\text{Mn}$  into 34.5 Torr of isobutane as a function of energy. These results were taken from SRIM’s Ion Stopping and Range Tables.

in the 1930s describes electronic stopping reasonably well,

$$S_{\text{elec}} = \frac{4\pi e^4 N Z_P^2 Z_T}{m_e v_P^2} \left( \ln \left( \frac{2m_e v_P^2}{I(1 - \beta^2)} \right) - \beta^2 \right), \quad (3.2)$$

where  $N$  is the number density of the target,  $Z_T$  is the target atomic number,  $Z_P$  is the projectile atomic number,  $e$  and  $m_e$  are the electron charge and rest mass respectively,  $v_P$  is the projectile velocity and  $\beta = v_P/c$  is the normalised velocity term. The parameter  $I$  represents the mean excitation and ionisation potential of the target and is normally experimentally determined [44].

Typically, an ion is fully stripped when the ion’s velocity is larger than the classical velocity of the innermost electron, given by  $v_e = Z_P v_0$  where  $v_0 = 2.2 \times 10^6 \text{ m s}^{-1}$  [47]. In this case, most AMS projectiles are not fully stripped and thus Equation 3.2 does not apply. Instead, the projectile charge is determined by electron capture and loss reactions which produce a charge state distribution. As mentioned in section 2.2, this distribution was described with semi-empirical formulas compiled by Sayer [40]. Assuming that the probability that an ion adopts a certain charge state is given by  $\Phi(q, v_P, Z_P)$ , we can then adapt Equation 3.2 to yield a revised electronic stopping formula,

$$S_{\text{elec}} = \frac{4\pi e^4 N q_{\text{eff}}^2 Z_T}{m_e v_P^2} \left( \ln \left( \frac{2m_e v_P^2}{I(1 - \beta^2)} \right) - \beta^2 \right) \quad \text{with } q_{\text{eff}} = \sqrt{\sum_{q=0}^{Z_p} q^2 \Phi(q, v_P, Z_P)}. \quad (3.3)$$

Note that the distribution  $\Phi(q, v_P, Z_P)$  is still heavily dependent on the projectile atomic number. In this way, projectiles of the same mass and energy (namely interfering isobars) can be separated by their energy loss characteristics.

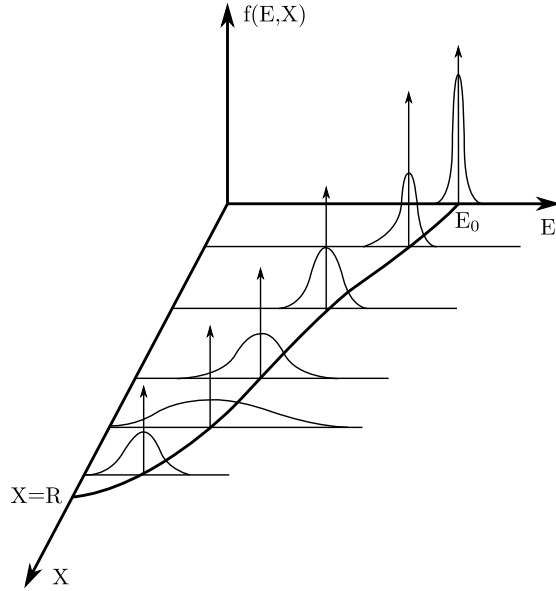


**Figure 3.2:** Plots of the energy distribution of an initially mono-energetic beam of charged particles at successive penetration depths. The straggling initially increases in width and skewness, although at low energies a focusing effect occurs. This figure has been reproduced from Knoll [44].

### 3.1.2 Straggling

The microscopic Coulomb interactions are so intricate that the energy loss of any given particle will appear to be stochastic. This means that after a collimated, mono-energetic beam passes through a given thickness of material, it will acquire a statistical energy and angular spread due to the randomness of the interactions with the target. This effect is called *straggling* and it provides a fundamental resolution limit for energy loss [44].

The width and shape of this distribution varies along the penetration path of the projectile as it depends on both the energy and the energy lost at any given point. A qualitative visualisation of how the energy straggling evolves with penetration depth is given in Figure 3.2. Determining a quantitative description of energy straggling is much more challenging. The first description was the Bohr formula [56], which takes quite a simple form

$$\delta E_{\text{bohr}} = 4\pi e^2 Z_P \sqrt{Z_T N \Delta x}, \quad (3.4)$$

with the same parameters as used previously. Bohr's formula works well for fully stripped particles like protons and alpha particles, but significantly underestimates the straggling for partially stripped projectiles. For partially stripped projectiles, the majority of the energy loss is distributed through electron capture and loss reactions which are not accounted for in Bohr's model. Yang et al. [57] developed empirical formulae using semi-empirical scaling relations that improved the accuracy of straggling estimates significantly.

Accurate predictions are still challenging today, primarily because there is a lack of experimental data for energy straggling of heavy ions in various targets [58]. This is due to the immense number of combinations of ions, targets and energies. Schmidt-Böcking and Hornung [59] have attempted to provide a semi-empirical formula for heavy ions into argon-methane and isobutane gases. Their formula is based on several assumptions valid

for the specific situation of ionisation chambers, gas type, and heavy ions; it is given by

$$\delta E \approx c(v_P, Z_P, Z_T) \overline{\Delta E} \frac{S(E_0 - \overline{\Delta E})}{S(E_0)}, \quad \text{with } c(v_P, Z_P, Z_T) \approx 14 \sqrt{\frac{Z_P Z_T}{Z_P^{1/3} + Z_T^{1/3}}}, \quad (3.5)$$

where  $\overline{\Delta E}$  is the average energy loss. This equation yields energy straggling in keV if the average energy loss is given in MeV.

It is evident that this formulation takes into account the changes in the stopping power throughout the projectile flightpath. The  $S(E_0 - \overline{\Delta E}) / S(E_0)$  terms modulates the straggling given how much energy is lost. For flat sections, it is mostly unitary whilst at the Bragg peak, the energy straggling increases. Near the end of the flightpath however, the energy loss correlation generates a focusing effect as ions that experienced lower energy loss previously are subject to high stopping and vice versa [47].

## 3.2 Raytrace and the Enge Split-pole Spectrograph

As discussed in section 2.2, we use a gas-filled Enge split-pole spectrograph for separation of interfering isobars. There are several operating parameters of the Enge that can be varied to give optimal operation. In particular, these are the gas pressure in the spectrograph and the magnetic field applied by the poles. For the magnetic field, a lower field strength will increase the radius of the flightpath through the spectrograph, which will increase the time the beam experiences under the magnetic field, increasing the separation power. However, this improved separation competes with the increased energy and angular straggling associated with more collisions, and consequently it is not obvious which field strength gives the optimum resolution. Similarly, an increased pressure will stabilise the mean charge state but increase the straggling.

To determine the optimum isobar suppression parameters for the Enge, a Monte Carlo simulation called *Raytrace* was used. Raytrace was first written by Spencer and Enge [41] to help them design and test the focusing capabilities of their spectrograph. At the time, the spectrograph was used for separating nuclear reaction products – there was no gas in the chamber – so the resulting trajectory of the ions was governed exclusively by the Lorentz force and the initial charge state. Paul et al. [38] adapted the program to include a Monte Carlo treatment of the charge-changing collisions within the gas-filled spectrograph. The theory behind this Monte Carlo simulation will be presented in the next section.

### 3.2.1 Charge-Changing Collision Theory

Paul et al. [38] describe in detail the physics behind their Monte Carlo treatment of the ion-gas interactions. I will briefly summarise their explanation such that the reader understands the limitations of their model. They deal explicitly with the charge-changing interactions by propagating between vertices in the trajectory associated with a charge-changing event. The path length from one collision to the next is given by

$$\ell = -\lambda \ln p, \quad (3.6)$$

where  $\lambda$  is the mean free path between charge-changing collisions and  $p$  is a random number between 0 and 1 that physically represents the probability of an ion surviving a path length  $\ell$  without a collision. At each vertex, the charge state is modified and the ion is propagated

by its equation of motion. The mean free path is related to the total charge-changing cross section  $\sigma_t$  by

$$\lambda = \frac{1}{N\sigma_t}, \quad (3.7)$$

where  $N$  is the atomic/molecular density. Given the cross sections, we could then accurately calculate the distance between each vertex.

However, there is little physical data on charge-changing collisions for heavy ions so a phenomenological model is used instead. Initially, we suppose that the equilibrium charge state distribution is approximated by a Gaussian function

$$F_q = \frac{1}{d\sqrt{2\pi}} \exp\left(-\frac{(q - \bar{q})^2}{2d^2}\right), \quad (3.8)$$

where  $\bar{q}$  is the mean charge state and  $d$  is the standard deviation. Then the single electron capture and loss cross sections can be approximated by exponentials,

$$\begin{aligned} \sigma_c(q) &= A_c \exp(b_c(q - \bar{q})) \text{ and} \\ \sigma_l(q) &= A_l \exp(b_l(q - \bar{q})). \end{aligned} \quad (3.9)$$

Given this form, and the assumption that the charge only changes during charge-changing collisions, the following relations can be derived:

$$\begin{aligned} d^{-2} &= b_c + b_l, \\ A_l &= A_c \exp\left(\frac{b_c - b_l}{2}\right). \end{aligned} \quad (3.10)$$

Multiple electron capture processes have experimentally confirmed negligible cross sections so they are neglected in this model. However, multiple electron loss processes are significant and need to be accounted for. To do so, parameters for the equilibrium charge state distribution in Equation 3.8 are sourced from a semi-empirical formula, which in conjunction with the fitted values for  $A_c$  and  $b_c$ , are used with Equation 3.10 to determine the values for  $A_l$  and  $b_l$ . In this way, experimental knowledge is used to define the shift to a higher mean charge state by the multiple electron loss collisions.

The charge-changing cross sections are highly dependent on the ion velocity. Paul et al. [38] used the empirical scaling rule developed by Schlachter et al. [60] to scale the single electron capture cross section by the energy of the ion. The scaling relation is given by

$$\tilde{\sigma}_c = \frac{1.1 \times 10^{-8}}{\tilde{E}^{4.8}} \left(1 - \exp(-0.037\tilde{E}^{2.2})\right) \left(1 - \exp(-2.44 \times 10^{-5}\tilde{E}^{2.6})\right), \quad (3.11)$$

where  $\tilde{\sigma}_c = \sigma_c Z_G^{1.8}/q^{0.5}$  is the reduced capture cross section in  $\text{cm}^2$ ,  $\tilde{E} = E / (Z_G^{1.25} q^{0.7})$  is the reduced kinetic energy in  $\text{keV u}^{-1}$ , and  $Z_G$  is the atomic number of the gas. In the case of diatomic molecular gases like nitrogen,  $Z_G$  is the atomic number of nitrogen and the cross sections are multiplied by two.

Over the course of the calculation, the energy dependent capture cross section given by Equation 3.11 are fitted to Equation 3.9 to derive the energy dependent parameters  $A_c$  and  $b_c$ , which are used (as above) to determine  $A_l$  and  $b_l$ . In this way, the total cross section  $\sigma_t(q) = \sigma_c(q) + \sigma_l(q)$  is calculated which defines the mean free path  $\lambda$  by Equation 3.7. The probability that electron loss (capture) occurs is then given by  $\sigma_l/\sigma_t$  ( $\sigma_c/\sigma_t$ ).

The charge-change at each vertex is determined by the capture-loss cross sections.

Angular straggling is also introduced at each vertex by shifting the velocity vector by  $\delta_\Omega$ , sampled from the Gaussian distribution

$$P(\delta_\Omega) = N_0 \exp\left(-\frac{\delta_\Omega^2}{2d_\Omega^2}\right), \quad (3.12)$$

where  $d_\Omega$  is the standard deviation. This distribution was calculated by a formula following the Meyer and Sigmund-Winterbon theories [61].

Having both the charge-change and the angular straggle determined at each vertex, the ion is then propagated by its equation of motion between vertices. The ion experiences both the Lorentz force from the magnetic field and the electronic stopping power from the gas. The electronic stopping collisions do not necessarily change the charge of the ion and the mean free path of these collisions are significantly shorter than that of the charge-changing collisions. As a result, we assume the stopping power to be continuous such that the equation of motion is given by

$$m \frac{dv}{dt} = q(\mathbf{B} \times \mathbf{v}) - \frac{dE}{dx}(|\mathbf{v}|). \quad (3.13)$$

Since the ionic charge does not change between vertices, the stopping power can be scaled from the average stopping power by

$$\frac{dE}{dx} = \left(\frac{q}{\bar{q}}\right)^2 \left(\frac{dE}{dx}\right)_{ave}. \quad (3.14)$$

The average stopping power is easily determined by SRIM [52].

Paul et al. [38] found that this adapted Raytrace program accurately reproduced both the observed pressure resolution minima and the path trajectories through the spectrograph. In the simulations discussed in the following sections, the above version of Raytrace was used, sourced directly from Michael Paul who developed it at the Argonne National Laboratory.

### 3.2.2 Separation Results

Ultimately, the isobar suppression capabilities of the Enge spectrograph depend on both the peak-to-peak separation and the width of those beams. To quantify this, we considered the *resolution* of the peaks, a concept used extensively in high performance liquid chromatography,

$$R = \frac{2(P_A - P_B)}{W_A + W_B}, \quad (3.15)$$

where  $P$  is the peak position in cm and  $W$  is the full width at half maximum (FWHM) in cm. Note that the FWHM is related to the standard deviation  $\sigma$  by  $FWHM = 2\sqrt{2 \ln 2} \sigma$ . A higher resolution means better separation.

In the simulations, 5000 ions of both the radioisotope and the stable isobar were run to provide adequate counting statistics. Characteristic energies of 181 MeV for  $^{53}\text{Mn}$  and 165 MeV for  $^{60}\text{Fe}$  were chosen with typical nitrogen pressures of 3.45 Torr and a pole field value of 1.05 T. The foil window is accurately reproduced with a  $20.1 \mu\text{g cm}^{-2}$  Mylar foil.

In addition to these obvious parameters, the detector position can also be adjusted. The original design by Enge [41] placed the focal plane of the spectrograph at an angle to the exit face of the second pole, as seen in Figure 3.3. By placing the detector on the focal

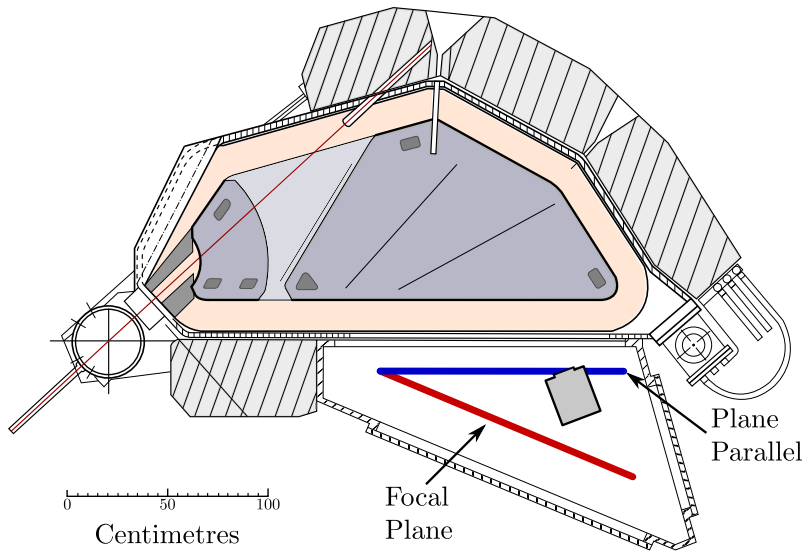


**Figure 3.3:** The position of the ionisation chamber detector can be moved around the detector chamber of the spectrograph. The two potentially optimum positions for the detector are along the focal plane in red and plane parallel to the exit face of the second pole. This figure has been adapted from Paul et al. [38].

plane, the maximum focusing effect would be achieved. On the other hand, if we placed the detector plane parallel to the exit face of the second pole, then the percentage of beam path outside the magnetic field would be reduced, decreasing the angular straggling from interactions with the gas. For reasons discussed in subsection 3.2.4, the following results apply when the detector occupies a plane parallel position.

The Enge produces separation in both planar position and energy space due to the Lorentz force acting on different mean charge states and the difference in stopping powers respectively. Figure 3.4 shows the results from a typical Raytrace simulation that was run. Figures 3.4a and 3.4b demonstrate the position separation in the plane of the spectrograph.  $^{53}\text{Mn}$ - $^{53}\text{Cr}$  has a resolution approximately half that of  $^{60}\text{Fe}$ - $^{60}\text{Ni}$  because Mn ( $Z = 25$ ) and Cr ( $Z = 24$ ) are only separated by one proton, whereas Fe ( $Z = 26$ ) and Ni ( $Z = 28$ ) are separated by two protons.

Due to the difference in stopping power (as predicted by Equation 3.3), the isobars arrive at the detector with different mean energies. Theoretically, this gives us a gate from the total energy signal in the detector, although in practice the separation is often significantly less than provided by the split anodes. Figures 3.4c and 3.4d also demonstrate the energy distribution of the stable isobar when it is gated based on its position separation, simulating the physical blocking plate. There is a slight bias to lower energies for the gated ions although this effect is somewhat negligible compared to the energy separation in the ionisation chamber.

It is evident from the fitted normal distributions shown in Figure 3.4 that the Raytrace data fits well to a Gaussian shape. This is unsurprising because the program samples its angular straggling point-wise from the normal distribution in Equation 3.12. This is not a very realistic treatment of angular or energy straggling. As a result, Raytrace underestimates the scattering tails for both the position and energy distributions, and this is evident in experimental data. This makes the separation much more difficult, primarily because it is the scattered particles that produce the interference in the ionisation chamber.

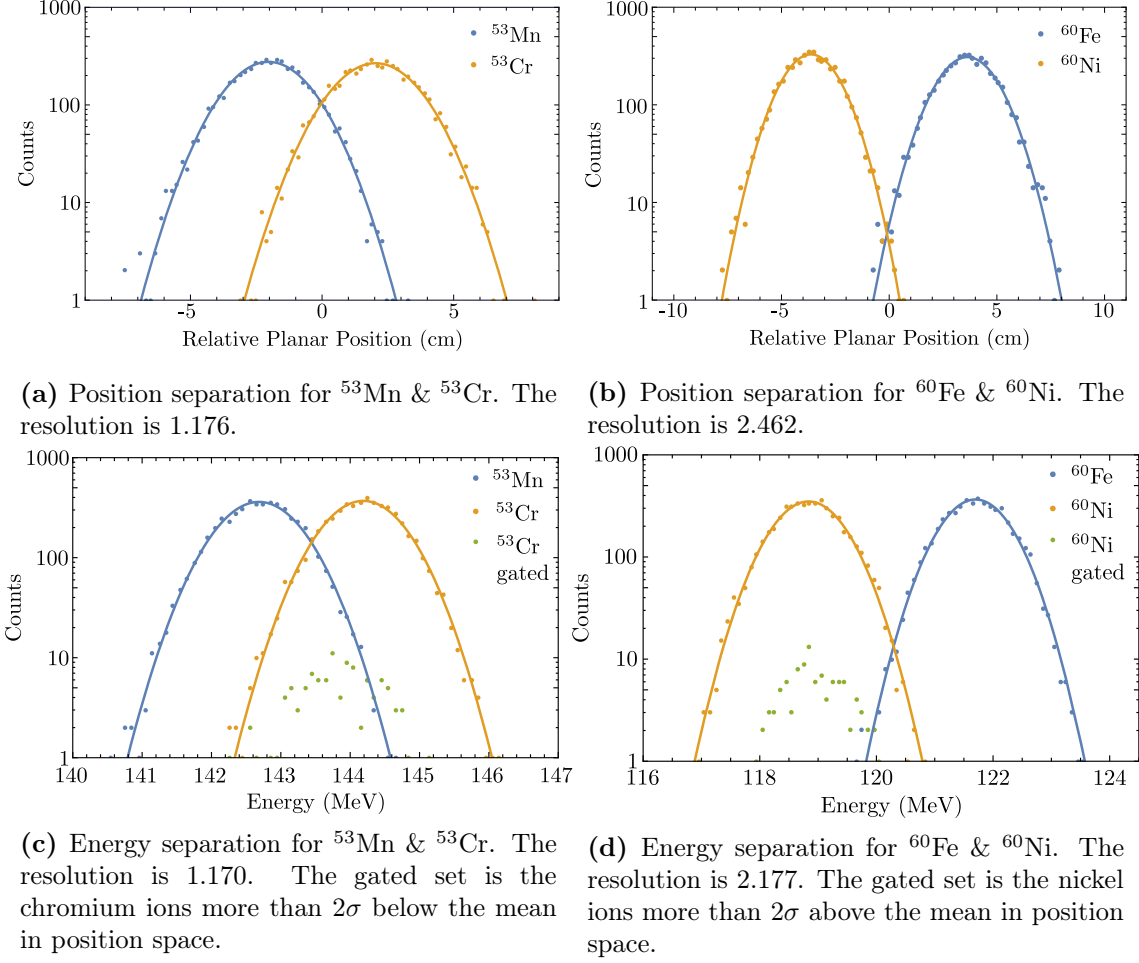


**Figure 3.4:** The separation predicted by Raytrace between the radioisotope and stable isobar in the Enge spectrograph. The pressure was 3.45 Torr, the field strength was 1.05 T, and the detector was plane parallel.

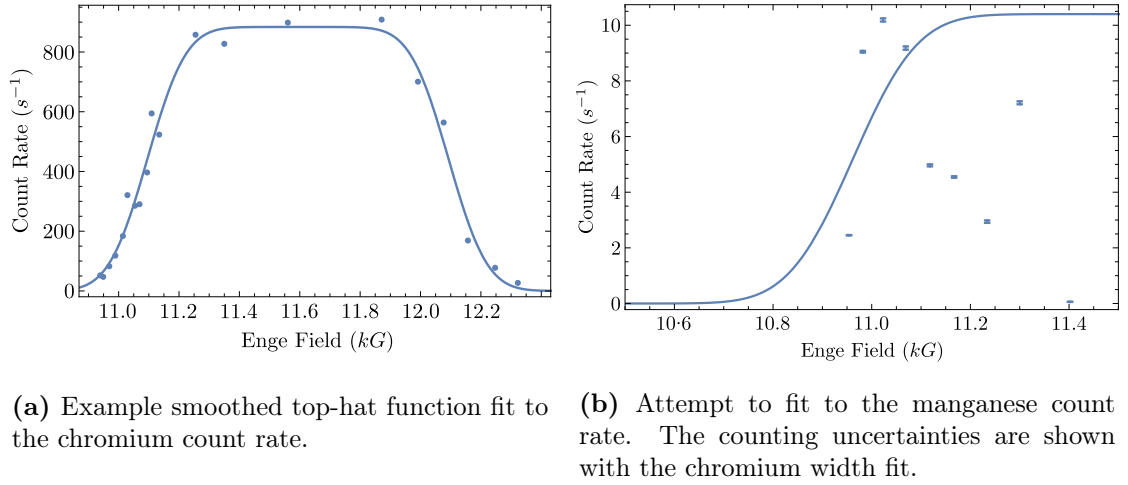
### 3.2.3 Experimental Comparison

When testing the separation capabilities of their Enge spectrograph for isobar separation, Paul et al. [38] used a focal-plane heavy-ion detector consisting of a gridded ionisation chamber with position sensitive proportional counters. We do not have access to such a detector at the ANU so comparing the predicted position results is more challenging. To measure the width of the beam with our current detector set-up, the beam was passed across the entrance of the ionisation chamber by varying the magnetic field in the Enge. As the beam is approximately Gaussian, the count rate should increase as the beam enters the detector, saturate when the whole beam is in the detector, and then decrease again producing a smoothed top-hat function as depicted in Figure 3.5a. From the rise time, the width can then be determined in terms of the magnetic field. Given the width of the detector window is known, this magnetic field width can be converted to centimetres, which are the units Raytrace uses for the focal plane distribution. The exact mathematical details of this inference are covered in Appendix A.

During use of the accelerator in August of 2017, the above methodology was implemented using manganese standards and blanks. The results for the chromium beam widths observed are presented in Table 3.1. The fitting error was on average about 10%, which

Energy (MeV)	Pres. (mbar)	Cr Width (cm)	Fit Error	Raytrace (cm)
194	5.2	1.011	10.1%	1.318
194	5.2	1.102	13.3%	1.318
119	5.2	1.077	4.35%	1.252
194	7.1	1.199	16.9%	1.167

**Table 3.1:**  $1\sigma$  beam widths of the observed chromium beams. Errors quoted are fitting errors, not measurement errors. The calculated Raytrace beam widths have been corrected for geometry inflations.



(a) Example smoothed top-hat function fit to the chromium count rate.

(b) Attempt to fit to the manganese count rate. The counting uncertainties are shown with the chromium width fit.

**Figure 3.5:** The results from the fits produced by scanning the beam across the ionisation chamber.

is quite good considering the methodology used. The exact experimental set-up was also simulated with Raytrace for comparison. It was found that the real measurements were on a similar order of magnitude but were lower by up to  $3\sigma$ .

Standard samples with high manganese counts were also measured to determine the separation of the two isobars at the detector. Figure 3.5b shows the manganese counts as a function of the magnetic field. The count rate fitted for chromium is included as a reference and the data points include counting error bars. It is quite clear that the smooth rise observed in Figure 3.5a is not reproduced by the manganese. The fluctuation in the count rate is also not attributable to the counting statistics as the uncertainty is negligible compared to the fluctuation. The primary problem for these measurements appeared to be source instability. The sample had been previously sputtered, so little material was left. Although decent beam currents could be produced, significant variability in the count rate occurred over the process of measuring. This was determined by the variation in the stable isotope current, which was recorded throughout the measurement. Therefore, we were unable to determine the separation conclusively.

The observed discrepancy in the beam widths can be partially remedied by correcting for the different geometries between Raytrace and the experiment. As visible in Figure 3.3, the detector face is placed perpendicular to the beam direction whilst the plane parallel focus is aligned with the pole face, at a distinct angle to the detector face. Since Raytrace produces its results along the parallel plane, the beam width is calculated to be larger than

it actually is because the beam impacts the plane at an angle. Using basic geometry, it is easy to derive magnitude of this inflation to be  $\sec \theta$ , where  $\theta$  is the angle between the plane normal to the beam and the plane of interest. In the Raytrace simulations on the plane parallel focus,  $\theta$  was maintained at  $20^\circ$ . This means that Raytrace overestimates the beam width by 6.42%. The reference beam widths in Table 3.1 have been corrected for this factor.

After the geometry correction, the predicted Raytrace beam widths were still  $2.1\sigma$  larger on average than the observed beam widths. As this uncertainty is only the fitting error, the uncertainty resulting in the variation of the source output could adequately account for this discrepancy. However, the fact that Raytrace consistently overestimates the beam width indicates the difference is systematic rather than random variation in the source. This is especially interesting as prior experience suggests that Raytrace underestimates the beam straggling. The source of this discrepancy was not investigated due to time restraints. Furthermore, since the presented discrepancy is only 15.5%, these results are sufficient to justify the use of Raytrace to predict quantitative optimisation trends calculated in the following sections.

### 3.2.4 Magnetic Field Optimisation

By decreasing the magnetic field, the percentage path length covered by the full magnetic field increases generating more separation. A competing effect is the increased angular straggling associated with an increased path length. To test which is the dominant factor for the ANU set-up and isotopes of interest, the resolution was determined by running Raytrace simulations for a variety of magnetic field values. Since Raytrace is a Monte Carlo program, each set of parameters was run five times to determine basic variances in the values of mean position and width yielding the uncertainty in the resolution via the usual propagation. Both running the Raytrace simulations and collecting the resolution statistics were automated using Python. The results are demonstrated in Figure 3.6 for

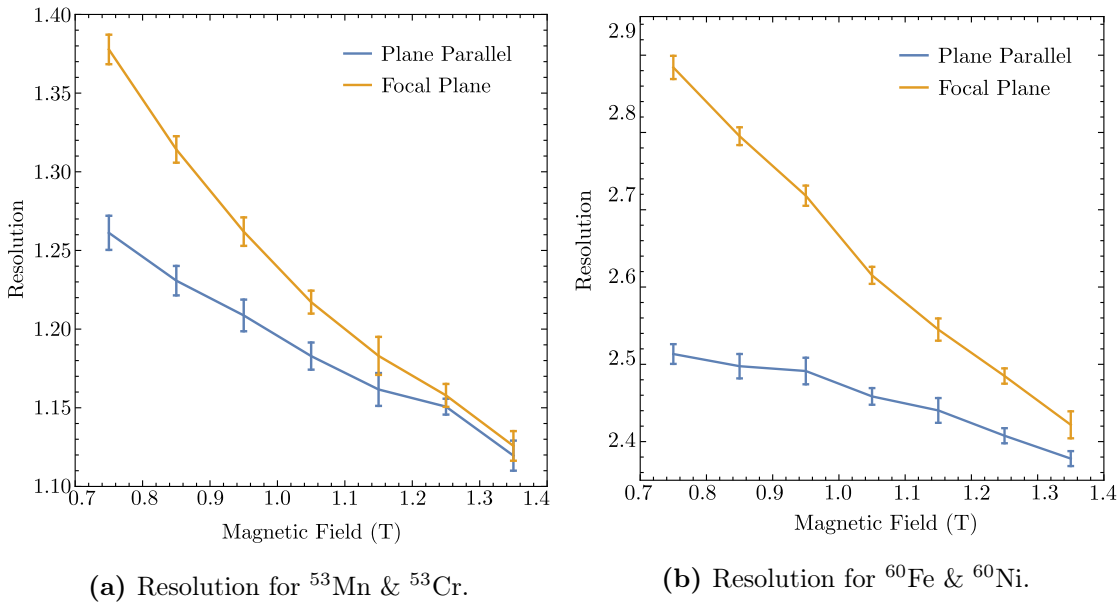


**Figure 3.6:** The resolution between the radioisotope and stable isobar as a function of the magnetic field strength in the Enge spectrograph. The pressure for all field values was 3.45 Torr.

both  $^{53}\text{Mn}$  and  $^{60}\text{Fe}$ . The field values were limited by the geometry of the spectrograph.

Several observations are immediately apparent. Firstly, lower magnetic field values produce higher resolutions. This supports the conclusion that an increase in the percentage of beam under the full field due to a larger trajectory radius is the dominant factor over increased straggling resulting from the longer trajectory. The plane parallel position also produces lower resolutions, which is due to the defocusing associated with moving away from the focal plane. This effect becomes more pronounced for larger trajectories as the distance between plane parallel and focal plane increases with larger radii. As a result, a comparatively small benefit is gained for decreasing field strengths at the plane parallel position.

From these results, one might initially conclude that the detector should be positioned with as large a radius as possible. However, as discussed in subsection 2.2.1, the purpose of the isobar separation is not to allow the least amount of the stable isobar into the detector but instead reduce count rates such that the measurement can be made. Despite the decreased resolution for stronger magnetic field values they yield shorter path lengths that retain more energy, which is beneficial for isobar separation in the detector. Thus, the exact optimisation depends on the sensitivity of the measurement you are trying to make.

### 3.2.5 Pressure Optimisation

The pressure in the Enge also controls two competing effects that can be used to optimise the resolution of the spectrograph. Increased pressure results in increased charge changing collisions, which reduces the deviation from the mean charge state, hence sharpening the beam. On the downside, it also increases the straggling, which broadens the beam. Paul et al. [38] demonstrated this experimentally and confirmed that Raytrace was able to accurately reproduce this effect. It was found that for 200 MeV  $^{58}\text{Ni}$  ions, a minimum magnetic rigidity resolution occurred at around 6.5 Torr. A comparable minima should be observed in the  $^{60}\text{Fe}$ - $^{60}\text{Ni}$  resolution.

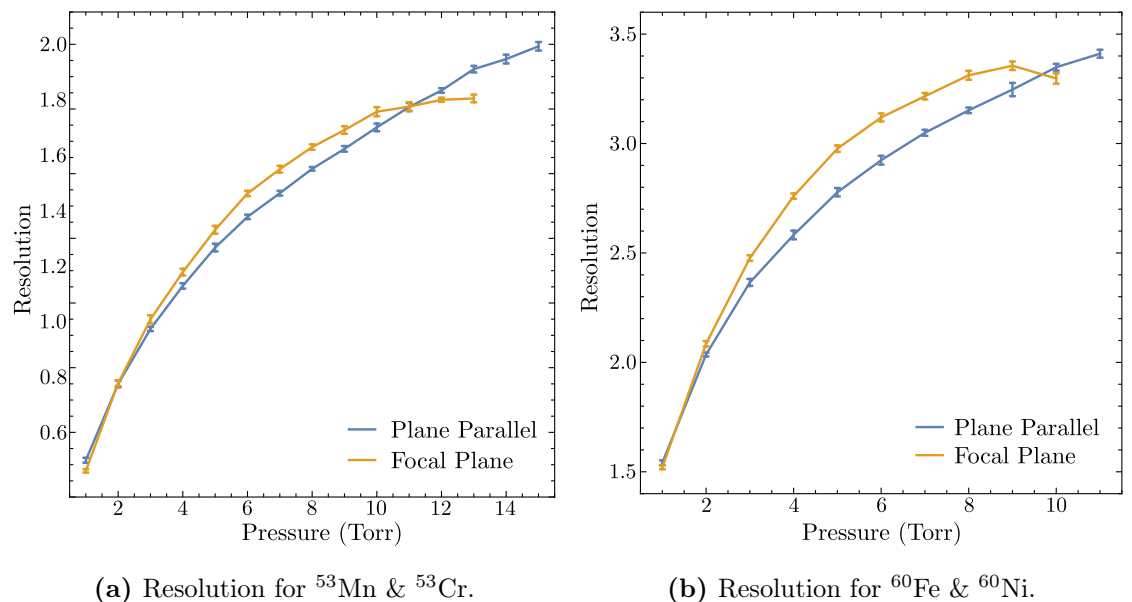


**Figure 3.7:** The resolution between the radioisotope and stable isobar as a function of the pressure in the Enge spectrograph. The magnetic field for all pressure values was 1.05 T.

Using the same method as the magnetic field optimisation, the resolution as a function of pressure for  $^{53}\text{Mn}$  and  $^{60}\text{Fe}$  is given in Figure 3.7. The pressure range is limited by the energies available, the data stops at the last pressure where all ion trajectories have a positive energy value. Since the plane parallel position has a shorter trajectory, higher pressure values were explored before the ions ran out of energy. For the large majority of pressure values, the focusing of the mean charge state is the dominant process and the resolution increases with pressure. At the focal plane, the maximal resolution value observed by Paul et al. [38] is achieved at 13 Torr for  $^{53}\text{Mn}$  and 9 Torr for  $^{60}\text{Fe}$ . The maximal resolution value is not achieved at the plane parallel position as the increased straggling has a smaller effect due to the shorter trajectory.

The maximum resolution is not exactly achieved where Paul et al. [38] indicated. Apart from the slightly different energy value, Paul et al. considered magnetic rigidity resolution,  $\Delta B\rho / \langle B\rho \rangle$ , which is independent of the trajectory radius as it is normalised out. In contrast, we only care about the total beam width, which would be minimised at a slightly higher pressure as it is not corrected for increasing radii. As a result, the prediction in Figure 3.7 agrees with the experimental validation from Paul et al.

The priority is only to get enough isobar suppression to provide suitable detector count rates – otherwise the energy in the detector needs to be maximised. The plane parallel position provides slightly worse resolutions but also retains more energy than the focal plane due to the decreased path length. From these results, it appears that the energy lost associated with any given gain in resolution, be that via decreasing the magnetic field or increasing the pressure, is approximately equal so it does not really matter how you increase the resolution. As a result, the current detector position, as indicated in Figure 3.3, is appropriate and any resolution gains can be achieved by adjusting the pressure in the Enge.

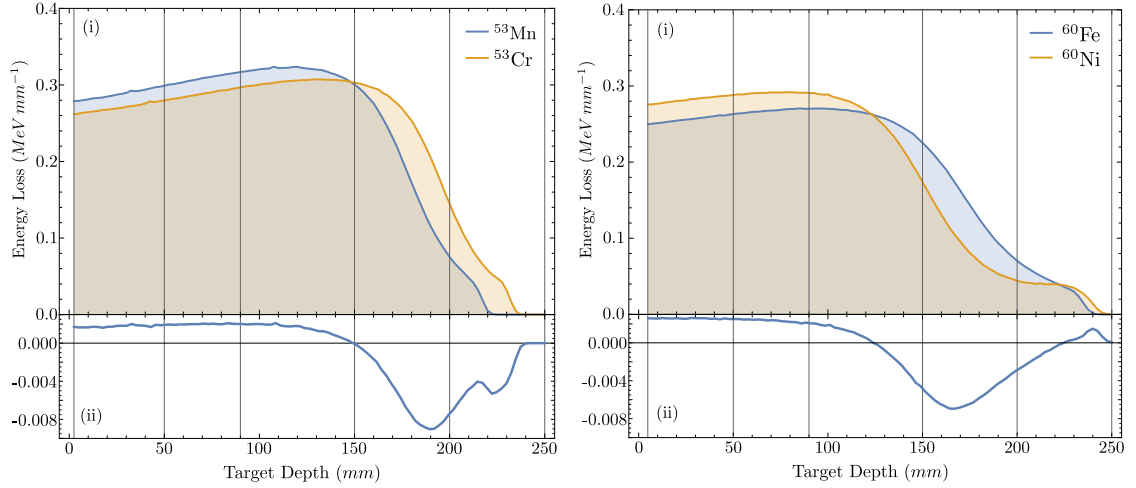
### 3.3 SRIM Simulation of the Ionisation Chamber

The final stage of AMS is to count single atoms in an ionisation chamber and use the energy loss signature of the ions to separate the interfering isobar from the radionuclide of interest. The exact energy loss for an individual ion is the result of approximately 6 million ion pairs formed during the ion's passage. The Stopping Ranges of Ions in Matter (SRIM) [52] is a Monte Carlo simulation that predicts the interactions of ions in matter dealing with ionisation, recoil collisions, phonons, target damage, and much more. It is one of the most cited scientific programs and the source of the majority of stopping range data due to its flexibility with beam-target combinations and its extensive experimental support. As a result, it is the perfect program with which to simulate the ionisation process that occurs inside our detectors.

I used SRIM in two ways to visualise the ionisation process and to quantify what separation power could be expected from the new detector. In the following section, I will detail the results I collected, what conclusions can be drawn from these simulations, and the limitations of the simulations themselves.

#### 3.3.1 Ionisation Curves

The ionisation of the target is roughly proportional to the energy loss of the ion in the energy range of about  $1\text{ MeV u}^{-1}$  that is used for  $^{53}\text{Mn}$  and  $^{60}\text{Fe}$  AMS. This is due to the dominance of electronic stopping in this energy range. Ionisation chambers rely on this



**(a)** Energy loss due to ionisation for <sup>53</sup>Mn and <sup>53</sup>Cr in 34.5 Torr isobutane at a mean energy of 137.7 MeV and 139.4 MeV respectively.

**(b)** Energy loss due to ionisation for <sup>60</sup>Fe and <sup>60</sup>Ni in 37.9 Torr isobutane at a mean energy of 115.9 MeV and 112.6 MeV respectively.

**Figure 3.8:** The energy loss due to ionisation curves for <sup>53</sup>Mn and <sup>60</sup>Fe isobar pairs. The vertical lines show the suggested anode splitting for the FASMA detector, detailed in section 5.2. Pane (i) shows the total energy loss whilst pane (ii) shows the differential energy loss by subtracting one curve from the other.

proportionality to estimate the energy loss. For such a simulation, SRIM is able to tell you the distribution of energy lost to ionisation, phonons, and vacancy production in the target. For the energies used for <sup>53</sup>Mn and <sup>60</sup>Fe, ionisation accounts for over 99% of the energy loss and thus is a good indication of the total energy loss.

SRIM can produce the total stopping powers for any given beam-target combination. However since the ionisation chamber only measures the ion pairs formed by electronic stopping, I chose to consider the ionisation specifically. Furthermore, since the stopping tables only take mono-energetic beam inputs, I used a TRIM calculation which is the Monte Carlo simulation component of SRIM. Using the specialised TRIM.dat input, I was able to specify the specific energy, position, and angle of incoming ions. With this method, I could take the Raytrace output and directly input the results into SRIM to produce an ionisation curve representative of the energy and position distributions of the incoming ion beam. The results for <sup>53</sup>Mn and <sup>60</sup>Fe are plotted in Figure 3.8.

From these ionisation curves, it is clear that the biggest energy deposition difference occurs at the point where the ionisation curves cross. The most important factor in designing a split anode configuration is to ensure a splitting is placed on this crossover point. This ensures all that the energy difference before and after the crossover is deposited on different anodes. If the crossover point occurred in the middle of an anode, then both isobars would deposit the same energy on that anode, as the difference before the crossover cancels the difference after the cross over.

In reality, it is hard to position the crossover exactly at the split in an anode. The crossover point also varies depending on the beam species. Therefore, it is important to have enough anodes such that good separation can be achieved, even if the crossover is not perfectly placed. The splittings indicated in Figure 3.8 have clearly been chosen specifically to suite <sup>53</sup>Mn. If these splittings and this pressure were used for <sup>60</sup>Fe, it is clear from Figure 3.8b that the third anode would produce no separation. To fix this,

the pressure could be increased such that the crossover occurred at the second-third anode boundary, or a new anode board could be designed.

Whilst aligning the crossover point correctly generates the biggest separation, there are other factors that mean further anodes can provide useful separation. As shown in Figure 3.2, the energy straggling is largest at the Bragg peak and is smaller at both the beginning and end of ion stopping. In particular, the Schmidt-Böcking straggling formula given in Equation 3.5 demonstrates that the straggling is scaled with the energy deposited on the anode. This means that whilst the difference in energy deposition might be greatest at the crossover, it will also experience the largest energy straggling as it occurs near the Bragg peak. Later sections of the detector benefit from focussing effects, which decrease the straggling and improve the isobar separation despite having a smaller energy difference. This effect is particularly powerful in the last anode, which can often provide the best separation of all the anodes. As a result, anode splittings both before and after the crossover are required to maximise the combined separation of the detector.

Further considerations for the split anode design are discussed in subsection 5.2.1.

### 3.3.2 Single Ion Counting with SRIM

Whilst ionisation curves are good at predicting the average behaviour of the incoming ions, they cannot reveal how the distribution in energies will appear in the spectra recorded by the detector. To simulate these factors, I decided to directly simulate the detection process by running SRIM for individual ions. To do this, I wrote a program called *AutoSRIM*. AutoSRIM takes the parameters for an ion from the Raytrace output, runs a TRIM calculation for a single ion using the TRIM.IN input file, integrates the resulting ionisation curve for a specific anode set-up, and records the energy deposited on each anode in an output file. In this way, the output from AutoSRIM produces anode spectra in the same way that the real detector produces spectra.

Several limitations of SRIM should be noted before comparing the old detector and the FASMA detector. SRIM usually calculates the energy straggling using Bohr straggling given in Equation 3.4. This can be up to a factor of three smaller than Yang straggling [57]. As a result, the energy spread predicted by SRIM will be smaller than actually observed. Furthermore, SRIM only consider the production of charge carriers, and not the collection process. In this respect, the FASMA detector should make significant improvements over the old detector with better grid shielding, improved field geometry, and newer electronics (see section 5.2 for more details).

A few interesting spectra produced by AutoSRIM have been plotted in Figure 3.9. Initially, as in Figures 3.9a and 3.9b, no angular distribution was given to the ions before simulation. Thus, we are able to view the natural peak width as a result of just the energy spread entering the detector. Because SRIM underestimates the energy straggling, these peaks are fully separated. The comparison between Figures 3.9a and 3.9b also reveal that the fundamental separation power of the new detector is only slightly better than the old detector. However, experience informs us that positioning the crossover such that it is nearly on the third-fourth anode boundary is practically impossible with the old detector. These simulations demonstrate that any separation gains with the FASMA detector should originate in improved usability and charge collection rather than better separation of the fundamental charge carriers.

In Figures 3.9c and 3.9d, I introduced a randomly sampled angular normal distribution

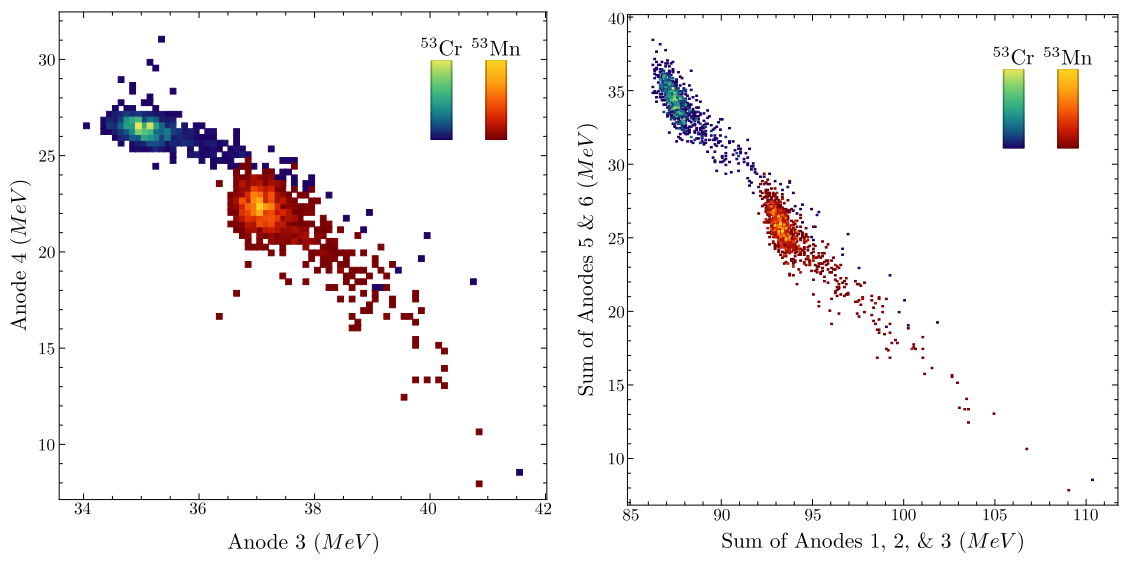
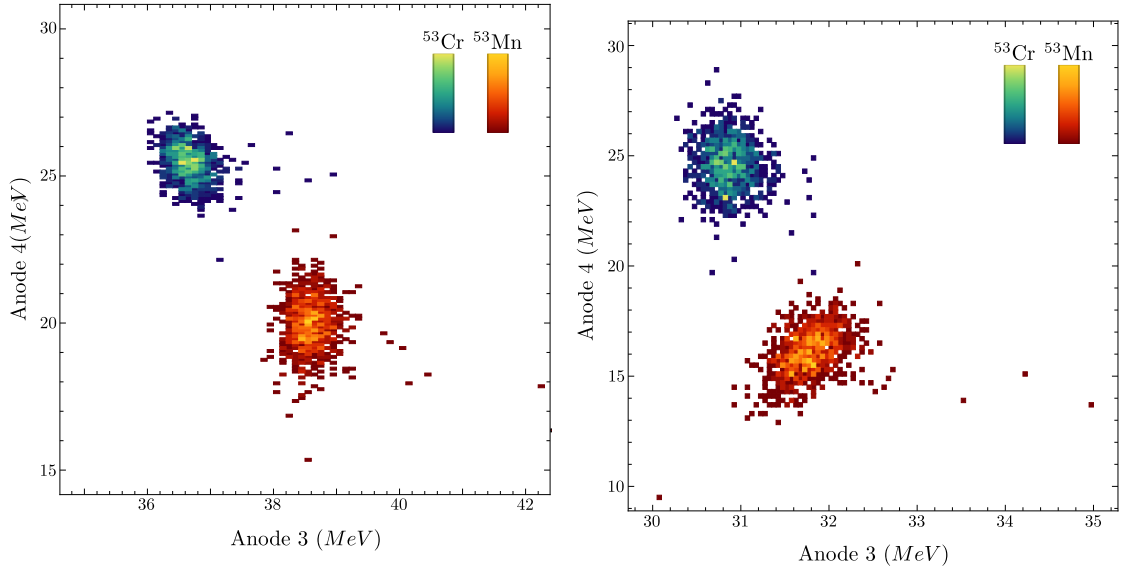


**Figure 3.9:** Simulated spectra using the AutoSRIM program. The beam was initially a 181 MeV  $^{53}\text{Mn}$  beam before the Raytrace simulation. Two-dimensional histograms have been used to simulate the analogue to digital conversion (ADC) channels in the real data acquisition.

---

with a standard deviation of  $10^\circ$ .<sup>1</sup> As evident from the spectra, this introduced a tail to the peaks that causes extensive overlap. This is because ions incoming on an angle will be stopped earlier in the detector, which introduces low energy tails for the deeper anodes and high energy tails for the closer anodes. This produces the characteristic diagonal tail that is visible in the spectra. We can see that even in the case of maximum possible separation in Figure 3.9d, the chromium tail still impinges on the manganese peak. This demonstrates that most of the isobar interference comes from scattered particles rather than the energy or position distribution of the beam.

Many of these simulation results have informed the choices made when designing the anode configuration for the FASMA detector. For further information on this, see subsection 5.2.1.

---

<sup>1</sup>Note that although I have only shown angular simulations for the FASMA detector, the old detector behaved very similar in these simulations.

# Meteorite Measurements

To demonstrate the typical measurement process implemented using the current detector, we analysed meteorite samples provided by Thomas Smith from the University of Bern. Full radioisotope depth profiles of meteorites are essential for many sub-fields of meteoritics and planetary science. In particular,  $^{60}\text{Fe}$  and  $^{53}\text{Mn}$  provide very useful exposure histories due to their simple target structure and long half-lives (see subsection 1.1.3 for further details). However, their use has been stymied by an “experimental database [that] is far from settled” [20]. This is partially due to the high energies required to perform Accelerator Mass Spectrometry (AMS) on  $^{60}\text{Fe}$  and  $^{53}\text{Mn}$ . As a result, meteorite data for both  $^{60}\text{Fe}$  and  $^{53}\text{Mn}$  is very rare. Whilst it is not obvious how much data have been collected, this work could have potentially doubled the available  $^{60}\text{Fe}$  and  $^{53}\text{Mn}$  data pairs.

These measurements also reveal the extent of the problems with the current ionisation chamber detector. As a result, the first component of this chapter will contain a detailed description of the current detector for preliminary comparison against the new detector. section 4.2 and section 4.3 will describe the process and results of the meteorite measurements. Note that these results are still preliminary and further beam-time will be required to adequately characterise the reproducibility of the measurements.

## 4.1 The Current Detector

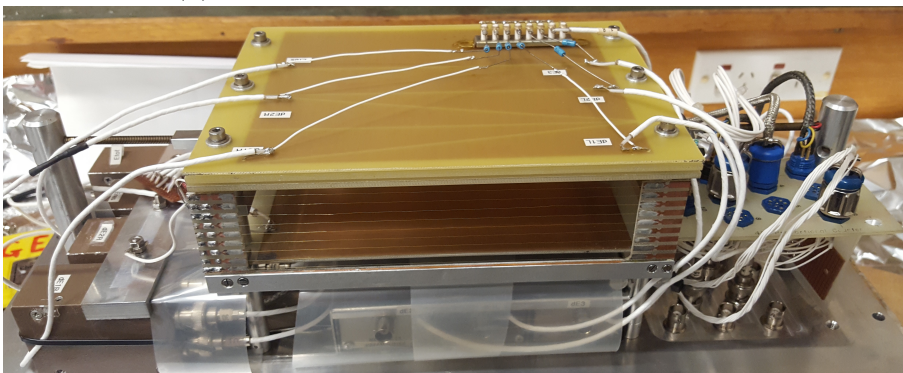
The current multi-anode ionisation chamber detector was adapted by L. Gladkis and L.K. Fifield from a short focal plane detector named the  $45^\circ$  focal plane detector (FFDFPD), which was used for difficult particle identification in nuclear reaction studies [9]. Whilst the detector is largely the same a decade later, some of the improvements implemented by Gladkis and Fifield have since been discarded. In this section, I will provide the physical schematics and electronic set-up to familiarise the reader and provide a basis for comparison in Chapter 5.

### 4.1.1 Physical Schematics

The detector is housed in a  $500\text{ mm} \times 175\text{ mm} \times 200\text{ mm}$  aluminium casket, as pictured in Figure 4.1a. The window aperture is centred on the largest face and is  $100\text{ mm}$  wide by  $40\text{ mm}$  high. This height matches the Enge spectrograph pole gap of  $38.1\text{ mm}$  so that the entire beam enters the detector despite the vertical spread. The edge of the aperture itself is a knife edge design, which minimises scattering events when used as a discrete mask with which to block the interfering isobar. This knife edge is symmetric as both the sides of the detector are used for different isotopes.



(a) Aluminium housing for the current detector.



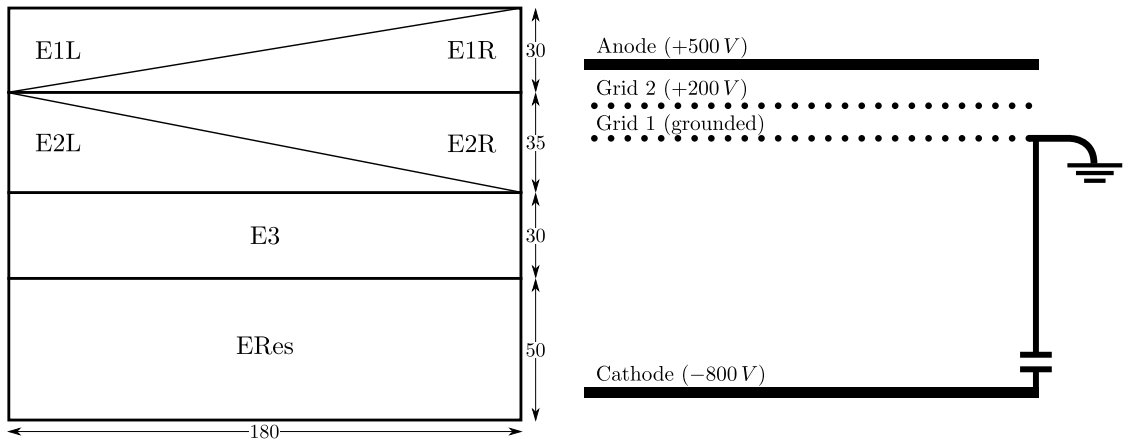
(b) Anode board and associated electronics.

**Figure 4.1:** Two images of the current ionisation chamber detector used in the gas filled magnet at the Australian National University.

The active component of the board is 180 mm wide and 145 mm deep such that scattered particles that enter on angular trajectories are still accepted. The pre-amplification electronics and wiring is attached to the lid of the housing on both sides of the electrode stack, as pictured in Figure 4.1b, which significantly broadens the housing and increases the overall weight of the detector. The anode stack and associated electronics are lowered into the housing and aligned using the screws in the lid.

The detector is filled with either propane or isobutane to pressures between 40-80 Torr. The detector does not have a gas cycling system, although for the most part, ageing of the gas has been negligible and stable pressures have been maintained for extended periods of time. The window is secured with a mylar foil that is 3.56  $\mu\text{m}$  thick (14C), although a mylar foil that is 6.10  $\mu\text{m}$  thick (24C) can be used for higher pressures. Due to the positive pressure in the detector, the foil bows outward significantly increasing the energy loss before the anodes for centralised particles. To mitigate this, Gladkis [9] attached a wire support frame for the window to allow for a thinner window and reduce the bowing effect. However, it was determined that the wire supports produced significant scattering events that outweighed the improvements.

Finally, the detector is mounted on Kevlar insulated brackets which electrically isolate the detector from the Enge spectrograph. This allows for a better handling of electrical noise associated with variable grounding. The mounting places the centre of the detector



(a) The anode configuration and labelling for the current detector in the horizontal plane. Distances are in mm.

(b) Schematic of the electrode stack for the current detector in the vertical plane.

**Figure 4.2:** The anode configuration for the current ionisation chamber detector.

approximately 15 cm from the pole face. As the detector is wide and must be situated normal to the incoming beam, there is a significant gap between the exit of the Enge spectrograph and the detector window.

#### 4.1.2 Electronics

The electrode stack consists of the usual cathode, split anode, and a double Frisch grid, as seen in Figure 4.2b. The first grid is grounded and capacitively coupled to the cathode which is held at  $-800\text{ V}$ . The second grid is held at  $+200\text{ V}$  and all sections of the anode are held at  $+500\text{ V}$ . Both the anode and the cathode are thin copper sheets supported on a fibreglass board. The anode splittings are depicted in Figure 4.2a. E1 and E2 are diagonally split. By comparing the relative signals induced on E1L and E1R (similarly for E2L and E2R), the position of the incoming particle can be determined. Given that the Enge separates the isobars in position space, this can be quite a powerful tool in stable isobar rejection.

Due to the proximity to the window that bows outward under pressure, the field lines are bent toward the window, which distorts and overwhelms any separation measured in E1. In particular, a height dependence is produced as lower electrons drift along distorted field lines to the window whilst others travel directly to the anode. To mitigate this, a grid of nine thin wires connected in series with  $100\text{ M}\Omega$  resistors is situated across the front of the electrode stack. Although this improves the field distortion, the signals from E1 are still generally quite poor.

The detector uses Canberra 125 and Ortec 142 pre-amplifiers to shape the signal induced in the anodes. The pre-amplifiers are mounted inside the chamber next to electrode stack to minimise the electrical noise associated with travel distance, especially before amplification. To measure the deadtime and the electronic noise of the system, a pulser signal is inserted in the pre-amplifiers. By measuring the width of the pulser distribution in the spectra, we can quantify the electronic noise component which is given in Table 4.1.

The energy resolution of the system depends on the gas pressure and type used in both the Enge and the detector. Close-to-optimum energy resolutions, which were taken from

**Table 4.1:** Energy and electrical resolutions of the current detector. These resolutions were determined using  $\text{MnF}_2$  blanks at 195 MeV. The Enge contained 3.9 Torr nitrogen and the detector had 71.5 Torr isobutane.

Anode	Energy Resolution	Electronic Resolution
ETot	2.3%	0.5%
E1L	11.5%	3.3%
E1R	14.4%	4.1%
E2L	6.5%	4.8%
E2R	14.2%	3.3%
E3	3.2%	6.3%
ERes	7.1%	6.3%

spectra produced with isobutane, are quoted in Table 4.1. This resolution was significantly improved over the resolution we were able to achieve during the meteorite measurements due to the effects discussed in subsection 4.2.1.

## 4.2 Manganese Measurements

The meteorite AMS measurements were made on the 14UD tandem accelerator described in Chapter 2. The meteorite samples were manganese-oxides ( $\text{MnO}_2$ ) so source outputs were relatively high, as discussed in subsection 2.1.1. The +13 charge state was chosen, which has a yield of 7.95% after stripping at this energy. Transmission from the low energy cup after the injection magnet to the Enge spectrograph was 0.71%, and is a combination of geometric transmission factors plus the charge state yield.<sup>1</sup> Current to the analysing magnet was kept constant whilst the terminal voltage and injection magnet were changed to measure  $^{53}\text{Mn}$  and  $^{55}\text{Mn}$ . The terminal voltage was 14.130 MV for  $^{53}\text{Mn}$  and 13.609 MV for  $^{55}\text{Mn}$ . As a result, the  $^{53}\text{Mn}$  beam had a total energy of 194.66 MeV.

Propane was used in the ionisation chamber itself as the isobutane supply unexpectedly ran out and no isobutane could be sourced in a timely manner. Due to the decreased stopping power of propane, higher pressures need to be implemented to fully stop the particles at 195 MeV. As a result, the thicker 24C foil was used, which holds higher pressures at the expense of degraded energy resolution. The detector was maintained at 98 Torr and 107 Torr for the first and second runs respectively. The Enge spectrograph was filled with nitrogen at 4.3 Torr throughout the measurements.

For each run, the  $^{55}\text{Mn}$  current was measured just before the Enge entrance using a current integrator for 10 seconds at the start and end of each ‘loop’. Due to the high radioisotope ratios, the loop length was 100 seconds for standard and unknown samples and 300 seconds for blank samples. Each measurement consisted of two loops, resulting in three current measurements and 200 (600) seconds total for standard/unknown (blank) samples. The count rate in the detector was maximised by adjusting the terminal voltage regularly, which improves reproducibility of the results obtained.

For clarity, I refer to a set of sample measurements with a given set of parameters as a run, and an individual sample measurement as a measurement.

<sup>1</sup>Transmission values are approximate at best as the currents measured on the Faraday cups are not absolute.

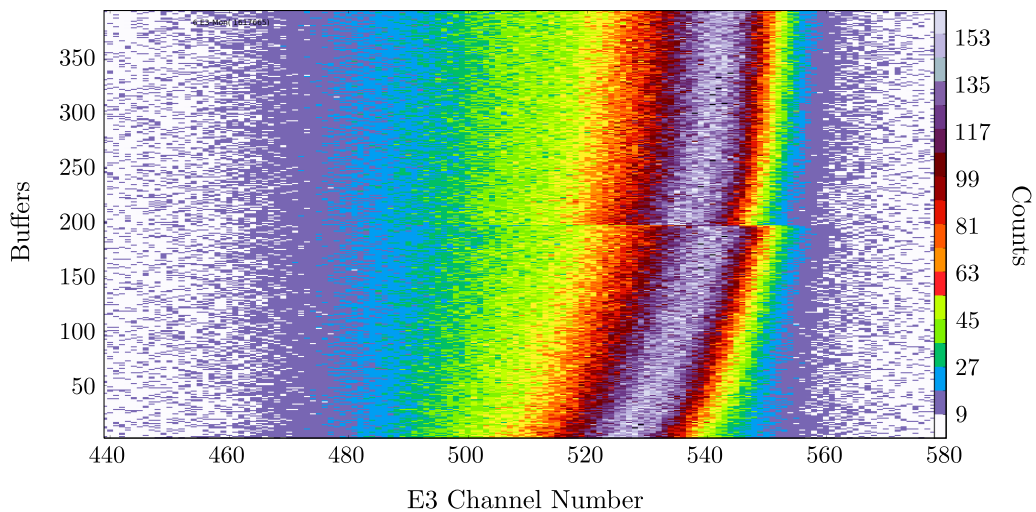


**Figure 4.3:** The monitor spectra for E3 from the TSH Blank sample. The buffers are a measure of the event storage, which, since the count rate is roughly constant, is proportional to the time. The discontinuous shift in the spectra is the boundary between the first and second loop.

#### 4.2.1 Energy Peak Drift

In the first set of measurements, the spectra produced from the anodes showed significant drifting in the peaks both throughout the individual measurements and across the run as a whole. The effect seemed to be count rate dependent and as a result blank samples, which are run at higher count rates, demonstrated significant shifts. We can see this quite clearly in the monitor spectra like Figure 4.3, which plot the buffers<sup>2</sup> against the channel number to reveal the temporal behaviour of the spectrum. In Figure 4.3, it is clear the chromium peak shifts from 526 to 543 across the measurement. The peak position bounces back in the middle of the measurement when the  $^{55}\text{Mn}$  current is measured but shifts again during the second half of the measurement.

In addition to the shift during measurements, the average chromium peak position in E3 shifted 53 channels across the first measurement run. Whilst E3 was the worst, E2 and ERes also shifted significantly. When the detector gas was changed, the peak positions reset to their initial values but then continued to shift.

During the second day, the shifting was significantly reduced to the extent that it was no longer visible in the monitor spectra and only shifted 15 channels during the first run and 5 channels during the second run. As we will demonstrate in the next section, the measured ratios are extremely sensitive to shifts in the spectra. In fact, the average gate on a given spectra may only be 25 channels wide so a shift of even 5 channels can cause significant chromium contamination. As a result, only spectra from the second day are analysed in section 4.2. It is possible to manually shift the gates the same amount as the observed shift in the chromium peak; nevertheless, the shift during the measurements would still be significant enough to cause large uncertainties.

The cause of the shift is somewhat mysterious. It was initially hypothesised that the propane gas was poor quality and was thus ageing during the measurement. Gas ageing, produced by the pulse height deficit described in subsection 2.3.3, results in a decrease in the charge collection efficiency of the detector. However, the shift is toward

<sup>2</sup>Buffers are a property of the data acquisition software that stores events in small packages. This design is specifically chosen so that monitor spectra and spectrum slices can be produced. Because the count rate is approximately constant, the number of buffers are roughly proportional to time.

higher channels which would indicate increasing energy deposition. The fact that the peak positions recovered after replacement of the detector gas and that the shift appears to be count rate dependent indicates it could be another phenomena associated with the gas. This effect has occurred only once before and was not observed when testing the new detector only a week later with the same gas, so it clearly needs further investigation.

#### 4.2.2 Spectra Analysis

This section describes the analysis of the anode spectra to extract absolute ratio measurements for the samples.

Different experimental conditions produce separation in different anodes and alters the peak position, necessitating the individual analysis of each measurement run. Generally three to four signals produce good separation between the chromium and manganese events. Individual gates are drawn based on the separation and are applied in combination to eliminate interfering chromium events. These gates are designed on both standard and blank samples to maximise the amount of manganese encompassed but minimise the number of chromium events accepted. Typically, three different gates are designed: a wide, normal and tight gate. The wide gate places the emphasis on the measured background as the main source of uncertainty, whilst the tight gate emphasises the counting statistics. These three gates structures are analysed independently of each other using the same data analysis method to determine which gate produces the lowest uncertainty and to ensure the uncertainty estimates are reasonable. The gate structures used for the first usable run are shown in Figure 4.4.

By only accepting events that occur within the gates from all four two-dimensional spectra, only manganese events were selected with  $\sim 1\%$  of counts accepted being chromium counts. From here, the *measured* ratio was calculated from the following equation:

$$\frac{^{53}\text{Mn}}{^{55}\text{Mn}_{\text{meas}}} = \text{counts} \times \frac{1}{\text{current}} \times \frac{1}{\text{chopper}} \times e \times \text{charge} \times \frac{2}{\text{pulser}}, \quad (4.1)$$

where counts is the counts accepted by the gates, current is the measured  $^{55}\text{Mn}$  current, chopper is the chopping factor applied to the  $^{55}\text{Mn}$  current,  $e$  is the electron charge, charge is the selected charge state after stripping, and pulser is the pulser counts observed in the spectrum.

As two loops are taken, there are three  $^{55}\text{Mn}$  current values available. If the current decline is approximately linear, then the current value used in 4.1 is simply the average. For every measurement taken, this was the case. If the measured currents were highly non-linear, then the ratio for each loop would have been calculated separately and the average taken afterwards. The chopping factor for these measurements was 1:20 (therefore chopper = 20) and the +13 charge state was selected. The pulser signal introduced at the pre-amplifiers not only measures the electronic noise but also provides an accurate determination of the dead time of the detector. Two pulsers are inserted every second, hence the factor of two. All of these values, with the exception of the recorded counts, are known very accurately compared to the more relevant uncertainties (discussed below) and I have hence assumed negligible uncertainty. The measured ratios for the sample TSI San Angelo, calculated with 4.1, are given in Table 4.2a.

Using different gates also gives us an idea of how much the drifting peaks affects the measurements. Ideally, the ratio of the measured ratio between different gates should be identical across all samples. This is because the same portion of the events are being

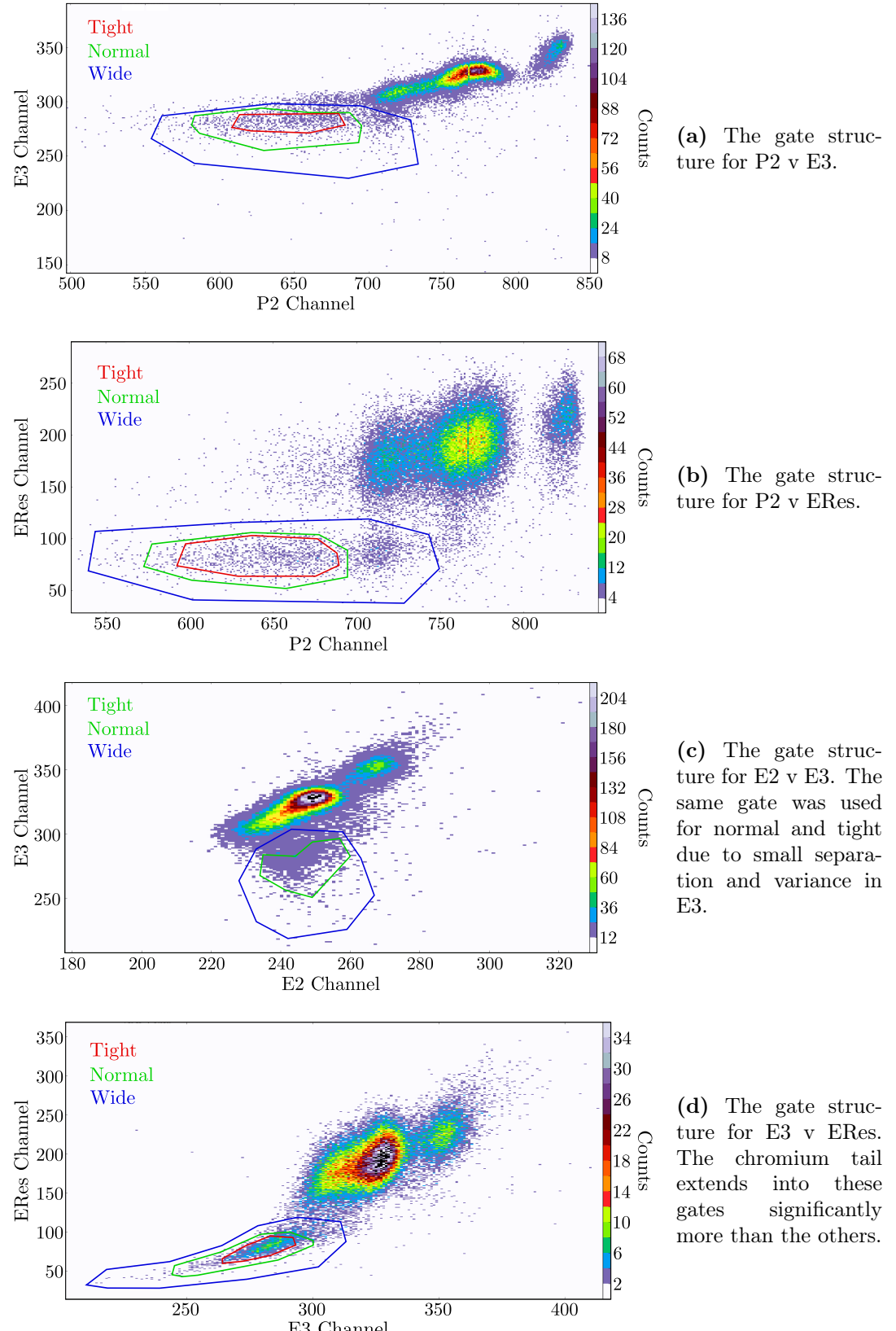


**Figure 4.4:** Comparison of different gates across the four spectra with good separation. The sample shown is a standard with a nominal ratio of  $1.38 \times 10^{-9}$ . The gates have been specifically designed to avoid the chromium tails more clearly evident in the blank samples.

**Table 4.2:** The ratio for each gate for the sample TSH San Angelo, and how these different gates vary across the run.

(a) Measured counts and ratios for sample TSI San Angelo.

	Counts	Ratio
Tight	691	$(9.24 \pm 0.05) \times 10^{-10}$
Normal	951	$(1.46 \pm 0.06) \times 10^{-9}$
Wide	2450	$(3.77 \pm 0.22) \times 10^{-9}$

(b) The ratios between the gates across all measurements during the first run.

	Gate Ratio	Std Dev	% Dev
N/T	1.63	0.049	3.0%
W/T	4.28	0.26	6.2%
W/N	2.63	0.15	5.7%

selected each time, regardless of the actual ratio of the sample. The variance in the ratios between the different gates would then give us an idea as to what extent each gate was susceptible to the shifts. Table 4.2b shows how the ratios of the measured ratio vary for each gate-pair. From the percentage deviation, we can see that ratios involving the wide gate varies the most, then the tight gate, and finally the normal gate. As we are dealing with ratios, the variance of the ratio will be the root mean square of the variance in the two gates. From this, we can actually estimate the variance in the individual gates. Values of  $\sigma_N = 2.0\%$ ,  $\sigma_T = 3.0\%$ , and  $\sigma_W = 5.5\%$  approximately reproduce the variance in the gate ratios with an average overestimation of 0.24%. We cannot see these drifts in the monitor spectra and so we are assuming that these fluctuations are random errors that are unrelated with the statistical counting error. As a result, the uncertainty in the measured ratio for each gate is the root mean square of the Poisson uncertainty from the individual counts and the estimated variance due to drifts for each gate.

The measured ratio is not the true ratio of the sample. First, we need to correct for the background included in the measurement. To do this, we look at blank samples which have been deprived of the active radionuclide by extended protection from any production channels. In this sense, any counts that make it through our gate structure and are recorded as ‘manganese’ counts must be either background manganese introduced through chemical preparation, source memory, etc., or chromium ions with highly improbable trajectories. Given the preparation standards employed at the ANU, the background is likely dominated by chromium events. However, the level of this chromium background depends on the chromium content of the sample in the first place. Using a series of blank samples with different chromium levels, the measured background rate can be fitted against the total events recorded (which is dominated by chromium counts) to determine a linear relation between the chromium rate and the measured background. Using this method, the measured ratio will have a background correction that is proportional to its chromium rate.

In this case, the background level was less than 1% of the total ratio because the meteorite ratios were so high ( $> 10^{-9}$ ). Furthermore, the statistical uncertainties dominate the background correction anyway, so the variance in the background correction contributes minimally to the overall uncertainty. Finally, due to the problem with the drifting peaks, this measurement series is not of particularly good quality so we were only interested in a quick analysis. The uncertainty in the variance of the background correction was assumed to be 50% of the total background level. The meteorite samples were prepared by Thomas Smith at the University of Bern. Smith provided us with blank samples associated with each chemical preparation batch of meteorites and it is these blanks that were used for background correction to ensure consistency with any introduced background. The

**Table 4.3:** The measured background signal and measured standard ratios for an example run. The normalisation factor is the nominal ratio of the standard divided by the background corrected standard ratio.

	Avg Background	Stat $\sigma$	Total $\sigma$	Standard Ratio	Stat $\sigma$	Norm Fact
Tight	$1.41 \times 10^{-12}$	13.8%	51.9%	$2.53 \times 10^{-10}$	3.7%	$5.50 \pm 0.27$
Normal	$5.44 \times 10^{-12}$	26.9%	56.8%	$4.27 \times 10^{-10}$	4.9%	$3.29 \pm 0.12$
Wide	$1.27 \times 10^{-10}$	6.2%	50.4%	$1.08 \times 10^{-9}$	4.5%	$1.45 \pm 0.12$

measured background level used for the TSI San Angelo sample is provided in Table 4.3.

Whilst over 90% of the radioisotope will make it into the Enge if the accelerator tuning is good, the gates may reject a significant percentage of the total radioisotope counts. This is acceptable as standard samples are measured with a known nominal ratio that can be used to calculate a renormalisation factor. The renormalisation is crucial to deriving the absolute ratio of the samples, and also cancels out any systematic errors associated with differences between accelerator set-ups, etc. The normalisation factor is simply the nominal ratio divided by the background corrected measured standard ratio. The standard sample was measured at the start, middle and end of each run. Because the standard varied non-linearly across this period, the normalisation factor was calculated separately for the first half and second half of each run. The normalisation factors and measured standard ratios used for the TSI San Angelo sample are provided in Table 4.3.

Ideally, renormalising yields a final ratio that, should be independent of the gate structure. At this point, we can compare the value yielded by each gate and since the analysis is independent, the values should agree within the statistical error quoted. This is a good measure of whether the error analysis has been realistic so far, as each analysis uses different numbers but the same process. It is also important to examine the relative values reported to see if the differences are in any way correlated which would imply inconsistent renormalisation. For the first run, the average variance between the ratios was  $1.11\sigma$  and on the second day was  $0.54\sigma$ . For a normal distribution, 50% of events are within  $0.675\sigma$  so this would indicate that the uncertainty was overestimated for the second run and underestimated for the first run. Since the peak drifting was worse for the first run whilst everything else stayed the same, this would indicate that comparing the ratios of the gates did not entirely account for the peak shifts.

The standard for  $^{53}\text{Mn}$  AMS was provided by Gregory F. Herzog by analysing kilograms of an activated meteorite sample. The nominal ratio is  $2.59 \times 10^{-10}$  and is assumed to be exact due to the very low uncertainties associated with activity measurements. On the other hand, the half-life of  $^{53}\text{Mn}$ , currently taken to be 3.7 Ma, was measured by Honda and Imamura [12] with an uncertainty of 10%. The nominal ratio is determined by calculating number of atoms  $N$  given the activity of the sample  $A$  and the half-life  $t_{\frac{1}{2}}$ ,

$$N = \frac{1}{\ln 2} A \times t_{\frac{1}{2}}. \quad (4.2)$$

Since the uncertainty in the activity is negligible, the nominal ratio also receives an uncertainty of 10% from the half-life measurement. This uncertainty in the absolute ratio is systematic and applied equally across all of the determined ratios. In fact, relative to each other, this uncertainty does not contribute and if the half-life measurement is improved, the improvement can be applied across all  $^{53}\text{Mn}$  measurements.

In addition to all of the above uncertainty treatment, we include a ‘reproducibility’ uncertainty associated with the inherent variance in the final ratio between different accelerator runs. This usually has to be collected across several different beam times and thus the following reported values are only preliminary results awaiting further validation. This reproducibility between the two different measurement runs analysed here has been estimated by taking the standard deviation of the two measurements. This varied between 4% and 26% over the samples, although the average was 9.5%.

The final  $^{53}\text{Mn}/^{55}\text{Mn}$  ratios are reported in Table 4.4 at the end of this chapter. The full data set used for determining these ratios can be found in Appendix B.

## 4.3 Iron Analysis

The iron meteorite samples were iron-oxides ( $\text{Fe}_2\text{O}_3$ ), and we selected the  $\text{FeO}^-$  negative molecular ion. The transmission from the low energy cup to the Enge spectrograph was 7.08%, given the +10  $^{54}\text{Fe}$  charge state yield.<sup>3</sup>

For iron measurements,  $^{54}\text{Fe}$  is used as the stable isobar, as both  $^{54}\text{Fe}$  and  $^{60}\text{Fe}$  require a similar terminal voltage. Since  $^{54}\text{Fe}$  is stable, the  $^{60}\text{Fe}/\text{Fe}$  ratio can be easily calculated from the measured  $^{60}\text{Fe}/^{54}\text{Fe}$  ratio by correcting for the natural abundance;  $^{54}\text{Fe}$  represents 5.85% of the total Fe composition. For  $^{60}\text{Fe}$  the +11 charge state, with a yield after stripping of 21.5%, was chosen with a terminal voltage of 14.144 MV. For  $^{54}\text{Fe}$ , the +10 charge state, with a yield of 21.0%, was chosen with a terminal voltage of 14.215 MV. Given these conditions, the  $^{60}\text{Fe}$  beam had an energy of 166.87 MeV.

The Enge spectrograph contained 3.2 Torr of nitrogen and was operated at a field of 1.174 T. The detector contained 60 Torr of propane and the 24C foil was used. The loop length was 1000 seconds for samples due to the low count rate and 100 seconds for standard samples. The  $^{54}\text{Fe}$  current was measured for 10 seconds at the start and end of each loop; however, due to the long run time, the source output was optimised to adjust for the change in the sputtering geometry of the cathode over the 1000 seconds.

### 4.3.1 Spectra Analysis

Because the stable isobar,  $^{60}\text{Ni}$ , has two protons more than  $^{60}\text{Fe}$ , the spectra analysis is significantly easier due to the separation achievable in the detector and the fact that the scattering tails move away from the  $^{60}\text{Fe}$ . Only a single type of gate is required to identify the  $^{60}\text{Fe}$  and the background level is often zero.<sup>4</sup> The gates used and the relevant spectra are displayed in Figure 4.5. It is clear from these spectra how marked the separation is, compared to the  $^{53}\text{Mn}-^{53}\text{Cr}$  case.

Counting statistics of  $^{60}\text{Fe}$  measurements make the largest contribution to the uncertainty of the measured ratio because of the low  $^{60}\text{Fe}$  concentrations. As a result, the source is often driven hard to achieve the highest possible currents and longer counting periods are required. Between measurement loops, the source is retuned to adapt to the changed sputtering geometry. Both the current before and after this retune are recorded manually from the analogue dial, and the average is used to calculate the mean current over the measurement. As we did not have drifting problems, the statistical error for the samples

<sup>3</sup>Note that this transmission value is 10 times higher than for manganese. This emphasises the different priorities for  $^{60}\text{Fe}$  and  $^{53}\text{Mn}$  measurements.  $^{60}\text{Fe}$  is easy to separate in the detector but has much lower ratios so maximising the transmission is much more important than achieving high energies.

<sup>4</sup>Over 20+ beam times, less than 10  $^{60}\text{Fe}$  counts have ever been recorded for the blank samples.

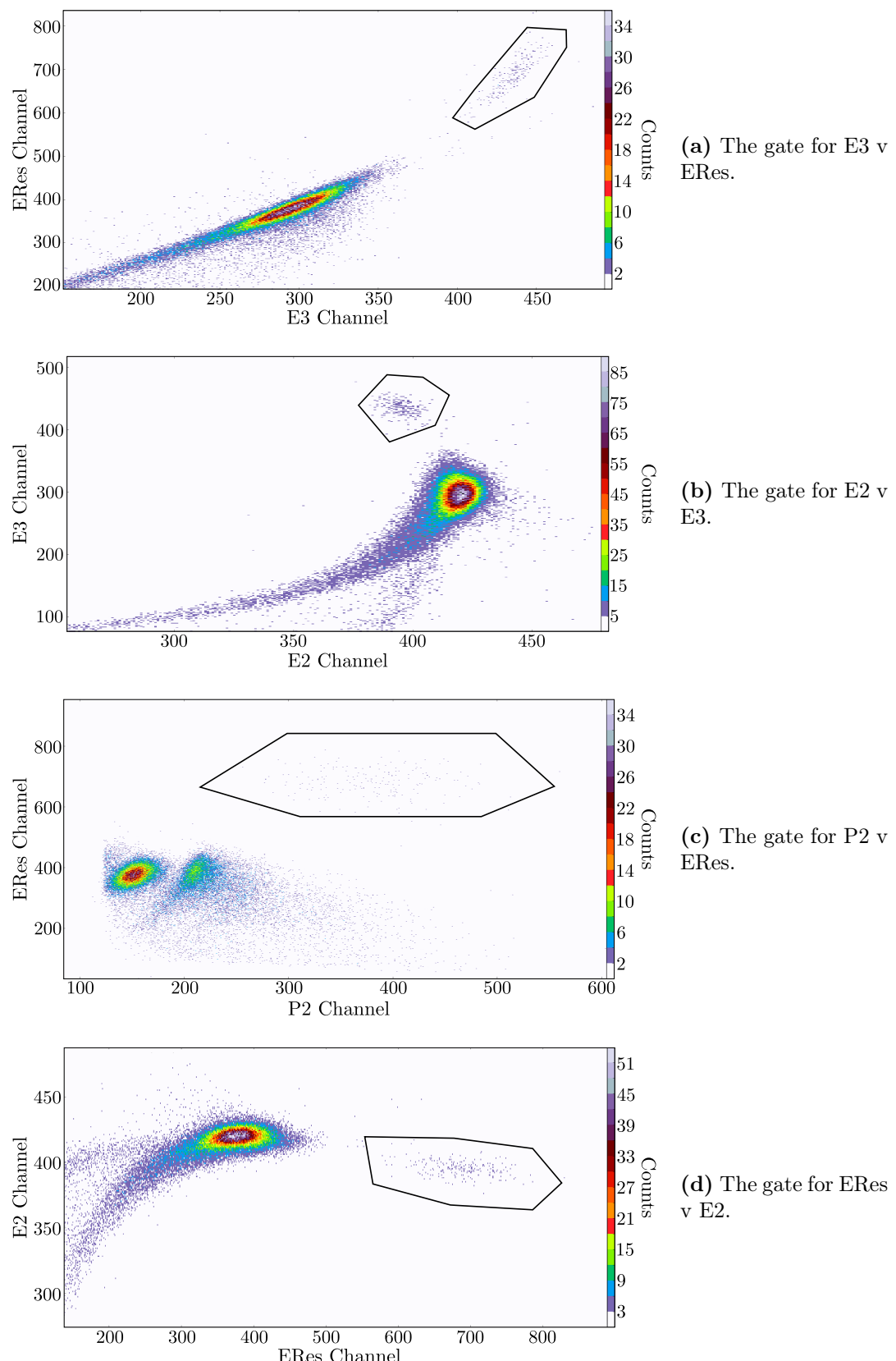


**Figure 4.5:** The gates used across the four spectra with good separation. The sample shown is a standard with a nominal ratio of  $1.25 \times 10^{-12}$ . The gates have been designed to accept as many  $^{60}\text{Fe}$  counts as possible since  $^{60}\text{Ni}$  barely interferes at all.

was just the Poissonian counting statistics. The measured standard ratios did not vary significantly so the value used to calculate the normalisation factor was simply the weighted average.

The background signal is more challenging to deal with. We measured three different blank samples for a total of 24,000 seconds ( $\sim 7$  hours) and did not observe a single count in the region of interest. As every blank sample was sourced from the same material, the 12 measurements can be added together to simulate a much longer measurement. This allows us to provide a much smaller upper limit on the background level given we did not observe any counts. For such minute background levels, classical Poisson statistics provide an unsatisfactory treatment of the  $1\sigma$  confidence levels (the uncertainty for zero counts is not  $\sqrt{0}$ ), especially as the physical confidence intervals are asymmetric. Feldman and Cousins [62] provide a classical confidence belt construction for upper confidence limits of null results that utilises accurate choices based on the data. Their construction applies specifically to Poisson processes with background. In our case, we are interested in the event number for a process with zero events observed and a mean background of zero (as we are measuring the background). The  $1\sigma$  confidence level is [0.00, 1.29]; thus, the  $1\sigma$  background limit would be calculated using 1.29 counts. Across our blank measurements, this yielded an upper limit of  ${}^{60}\text{Fe}/\text{Fe}_{\text{background}} = 1.20 \times 10^{-16}$ .

The standard used was prepared at the Paul Scherrer Institute (PSI) for the determination of the half-life of  ${}^{60}\text{Fe}$  [32]. It has a nominal value of  $1.246 \times 10^{-12}$  determined by activity measurements performed on  $(2.47 \pm 0.11) \times 10^{15} {}^{60}\text{Fe}$  atoms. The systematic uncertainty is limited by the uncertainty in the half-life, but this is only 1.92%, significantly less than the uncertainty associated with the  ${}^{53}\text{Mn}$  half-life. No repeat measurements were done due to time constraints, however the uncertainty should be dominated by Poissonian counting statistics in any case.

The final  ${}^{60}\text{Fe}/\text{Fe}$  ratios are presented below in Table 4.4. The full data set, including measured ratios, can be found in Appendix B.

**Table 4.4:** The final  ${}^{53}\text{Mn}/{}^{55}\text{Mn}$  and  ${}^{60}\text{Fe}/\text{Fe}$  ratios for the supplied meteorite samples. Note that these ratios are preliminary results that are self-consistent but underestimate the uncertainty associated with reproducibility. All uncertainties are included, along with uncertainty in the nominal value of the standards used.

Meteorite	${}^{53}\text{Mn}/{}^{55}\text{Mn} (\times 10^{-9})$	${}^{60}\text{Fe}/\text{Fe} (\times 10^{-14})$
TSI San Angelo	$4.82 \pm 0.55$	$1.26 \pm 0.32$
TSI Sacramento Mountains	$5.66 \pm 0.67$	$2.34 \pm 0.44$
TSI Tamentit	$2.47 \pm 0.29$	$2.30 \pm 0.39$
TSI Zeramra	$3.49 \pm 1.18$	- <sup>a</sup>
TSH Carthage	$2.40 \pm 0.54$	- <sup>a</sup>
TSH Charcas	$2.06 \pm 0.28$	$2.13 \pm 0.50$
TSH Chulafinnee	$2.35 \pm 0.31$	$4.71 \pm 0.75$
TSH Dalton	$3.23 \pm 0.40$	- <sup>a</sup>
TSH Durango	$2.25 \pm 0.27$	$2.27 \pm 0.51$
TSH Plymouth	$2.62 \pm 0.44$	$2.44 \pm 0.56$

<sup>a</sup> Value not measured due to time restraints.

# The New FASMA Detector

As evident from some of the problems faced in Chapter 4, the isobar discrimination power of the old detector needs to be improved in order to measure manganese samples with lower isotope ratios. Given optimum conditions, the current detector is capable of a sensitivity in the low  $10^{-13}$  range, as determined from blank samples. However, the AMS group at the Technical University of Munich were able to achieve a sensitivity of  $7 \times 10^{-15}$  from blank samples, so clearly improvements can be made. Over the past 18 months, a new detector has been designed and constructed that should improve the sensitivity of manganese measurements.

The detector has been christened the Flexible Anti-Scatter Multi-Anode (FASMA) detector, which highlights the interchangeable anode board configuration and improved scattered particle discrimination of the new anode design. In this chapter, I will explain the design ethos of the new detector, describe the physical and electronic schematics, and analyse the preliminary spectra produced by the first trial. Although it is still very early days in the optimisation process, the enhancements have already produced observable improvement. In conjunction, I will suggest some further refinements to improve the sensitivity.

## 5.1 Drawbacks of the Current Design

The limitations of the old detector make it difficult to improve the sensitivity of manganese measurements beyond  $10^{-13}$ . Some of these limitations are associated with the fundamental difficulty of separating  $^{53}\text{Mn}$  and  $^{53}\text{Cr}$ . On the other hand, quite a few can be improved by designing a purpose built detector for AMS.

The primary problem that limits the current sensitivity of manganese measurements is the interference of tails in the spectra due to scattered particle trajectories. These are particularly difficult to manage as the relevant simulation software poorly accounts for scattered particles, so adaptations can only be tested experimentally. The scattering tails are most prominent at the last anode where the scattered particles are stopped earlier in the detector. The scattering tails appear vertically in the ERes anode, as displayed in Figure 5.1, indicating that the highly scattered trajectories are associated with lower energies. This is somewhat beneficial because if scattered particles had higher energies, then they would very effectively reproduce manganese energy loss signals and directly interfere with the manganese peak, as discussed in subsection 5.4.2. What is clear from the spectra shown in Figure 5.1, is that the scattering tail that interferes most with the  $^{53}\text{Mn}$  peak, rather than the energy width of the chromium peak. If scattered events could be removed in post-processing, then the sensitivity capability of manganese measurements would significantly increase.

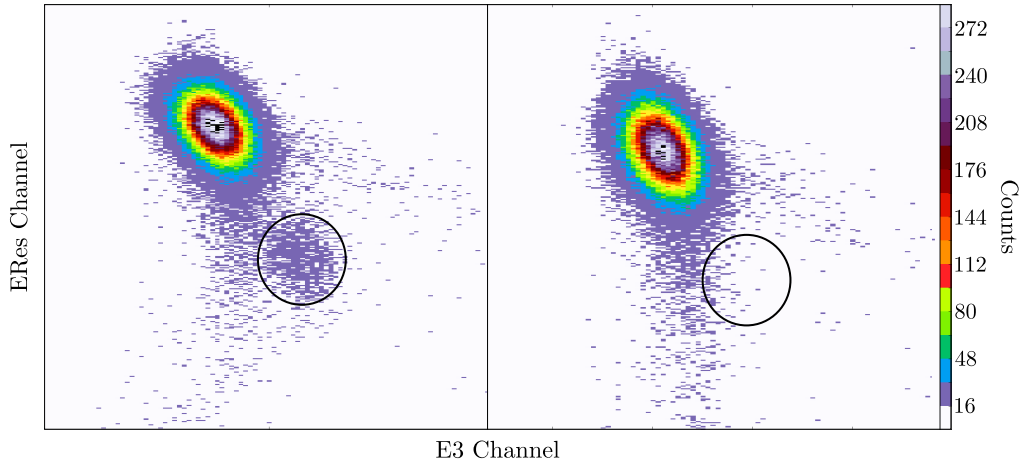


**Figure 5.1:** A comparison of a standard and blank sample taken with the old detector. The tail from the scattered particles obscures the separation achieved. These spectra were taken from a  $^{53}\text{Mn}$  run in March 2017.

The 14UD accelerator is capable of sustaining terminal voltages higher than 15 MV when conditioned appropriately. For the +13 charge state, this means the  $^{53}\text{Mn}$  beam could have energies in excess of 206 MeV. However, the ions cannot be fully stopped by the old detector at these energies, even when using isobutane. This is because the maximum pressure is limited by the 14C foil, which would burst under higher pressures. Larger energies are beneficial because the difference between the chromium and manganese signal deposited on the anodes grows with increasing energy. As a result, the detector should ideally be able to use all of the energy that can be provided by the accelerator.

The current detector also exhibits poor charge collection on the E1 anode. This is primarily due to field distortion created by the window grid, and the outward bowing of the window itself, which reduces the charge collection efficiency of the anode. In addition to this, there is minimal energy difference in the stopping power between manganese and chromium ions at the beginning of their trajectory. As a result, the current detector only has three anodes that produce effective separation. This makes it very difficult to optimise for a wide variety of isotopes. There is minimal flexibility in moving the crossover point onto an anode splitting and a relatively small number of anode combinations possible.

Apart from the conceptual issues above, the detector itself is ageing. In some instances, a dried coating of liquid has been found on the inside of the detector window. Although it is not clear what the culprit was, it has been suggested that the pre-amplifiers could have overheated and released a vapour that then congealed once the detector had cooled. The wiring inside the detector is somewhat haphazard and poorly shielded, which could contribute to the relatively high electronic noise levels observed. The total energy resolution is also poor (2.3%) when compared to ionisation chambers at other institutions (< 1%) [46]. The energy resolution is limited by the energy straggling in the Enge, but Raytrace simulations indicate that this should not be more than 0.77%.

## 5.2 FASMA Detector Design

The Flexible Anti-Scatter Multi-Anode (FASMA) detector was designed to rectify the problems outlined in section 5.1. The majority of design considerations were conceptualised by Martin Martschini during his post-doctoral position at the ANU.

### 5.2.1 Anode Board

The bulk of the achieved separation gains have been made with careful analysis of the anode board design. The new detector houses an anode board that is 200 mm wide and 250 mm long. The extra 105 mm of length solves several problems. Firstly, the new detector can stop a beam of 206 MeV  $^{53}\text{Mn}$  ions with only 42 Torr of isobutane (assuming  $\sim 56$  MeV is lost in the Enge). This means that for  $^{53}\text{Mn}$ , the maximum beam energy that can be fully stopped using the 14C foil and isobutane is  $\sim 250$  MeV, much higher than the 14UD can produce. The extra length in the detector also allows the crossover point to be shifted. This means different beam species with their own specific energy loss profile can be optimised for a given anode set, even if the full length of the detector is not used. For example, the  $^{60}\text{Fe}$  energy loss profile in Figure 3.8b indicates that  $^{60}\text{Fe}$  would best be operated at a higher pressure that positions the crossover on the E2-E3 boundary. This would leave E4 and ERes with poor separation, but they would not necessarily be required since the separation in E2 and E3 would be so good. This flexibility was not possible with the old detector due to shallowness of the anode board.

The previous anode splittings were not optimised for any particular isotope and did an especially poor job for  $^{53}\text{Mn}$ . In fact, it was very challenging to position the crossover point on the E3-ERes boundary, whilst still fully stopping the particles. To solve this problem, the FASMA detector has a removable anode that allows different anode splitting designs to be interchanged given the specific isotope being examined. This is facilitated by the use of copper plated fibreglass boards, which can be machined to the correct anode pattern. The electrode stack is slotted such that each board can slide into place. Every anode board has to have its own wiring, but with the use of a 25 pin D-sub feed-through embedded in the detector housing, changing the cabling is straightforward. This means individual anode designs can be used for each isotope, and also allows for several different designs to be trialled for  $^{53}\text{Mn}$ .

The initial anode design is presented in Figure 5.2a. As demonstrated in Figure 3.8a, this anode configuration places the crossover point for  $^{53}\text{Mn}$ - $^{53}\text{Cr}$  on the E3-E4 boundary. In this simulation, the mean stopping range was  $215 \pm 3$  mm for 137.7 MeV  $^{53}\text{Mn}$  ions and  $230 \pm 3$  mm for 139.4 MeV  $^{53}\text{Cr}$  ions. All ions are stopped in the last anode, which maximises the use of all anodes and the separation between the isobars.

As mentioned in section 5.1, the dominant factor limiting the sensitivity is the scattered tails. To deal with this, anodes E2 and E4 have been diagonally split to provide position information. Depending on the point of entry, the particle will deposit more or less of its energy on the left anode compared to the right anode. By looking at the ratio  $P = ER/(EL+ER)$ , the ‘position’ will linearly vary from 0 to 1, left to right across the anode. Note that by normalising against the total energy deposited on the anode, the position measurement is independent of the species of the incoming ion. As a result, a  $^{53}\text{Mn}$  ion and a  $^{53}\text{Cr}$  ion that enter the detector at the same position should produce identical position measurements (assuming the amplification is the same for EL and ER).

Given that both E2 and E4 can collect position information, angular information about the particle’s trajectory can be derived from the two data points. The old detector also has two position signals, derived from E1 and E2. However, because the E1 signal was distorted and the anodes were very close to each other, the angular resolution was limited and any suppression with this information was not helpful. By implementing the diagonal splitting on E2 and E4, the distortion from E1 is removed and over 70 mm is gained in the distance between the position measurements. This should improve the resolution of the

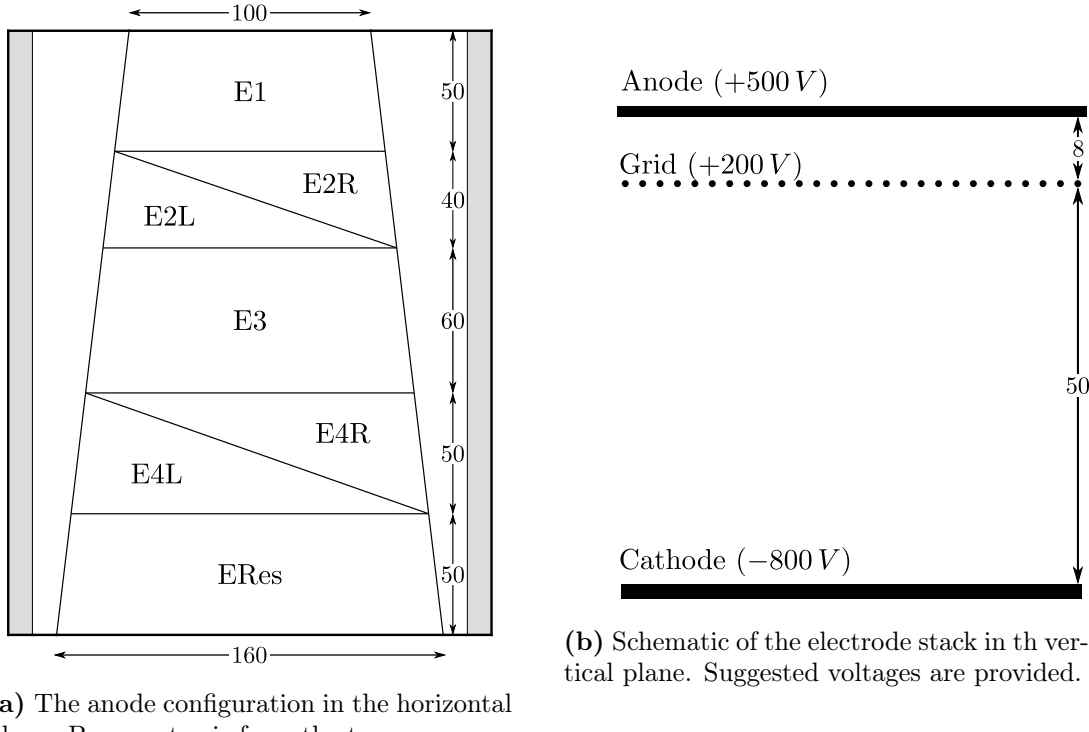


**Figure 5.2:** The anode configuration for the FASMA detector. All distances are in mm.

angular measurement.

There are a few ways to implement angular determination from two position channels. You could look at the difference between the two position values  $|P_2 - P_4|$ , and the deviation from zero would indicate the angular nature of the trajectory. In reality, this would be difficult to achieve because E2 and E4 are not the same size so normal trajectories would not give zero values, as in the ideal case. In addition, a correction factor to account for different amplification of E2 and E4 would have to be included. This would mean some angular trajectories could ‘cheat’ and appear with a position difference smaller than that of a normal trajectory.

Another option is to plot the two derived position channels against each other, and the normal trajectories will form a bijective linear relation. With this information, highly scattered particles can be eliminated by applying gates that only accept events close to this linear relation. Because the position measurements are normalised by the total energy deposited, both  $^{53}\text{Mn}$  and  $^{53}\text{Cr}$  should appear on the same linear line. This design choice alone should vastly improve the sensitivity of manganese measurements.<sup>1</sup>

Finally, note that the active anode components do not occupy the full width of the board and are tapered toward the front. Since the electrode stack is grounded, the walls of the stack used to support the anode, grid and cathode (as pictured in Figure 5.3b) will generate distortions of the electric field. The ‘buffer’ at the edge of the board protects the active anodes from this effect and ensures a uniform field (the buffer will also be held at +500 V). The tapered design also helps to reduce noise and interference from highly scattered events.

<sup>1</sup>Note that the electronic noise is independent of the anode size or shape and more anodes increases the relative contribution of the electronic noise. This is why anode splitting is generally minimised if possible and why only two of the five anodes have been diagonally segmented.

### 5.2.2 Geometry

For any given ionisation chamber detector, there are several parameters associated with the geometry of the detector that can be optimised to give the best energy resolution. These factors vary depending on the species used and the operating energy, so each detector needs to be calibrated independently.

The Frisch grid is designed to shield the anode from any signals below the grid, removing the height dependence of pair formation. The *inefficiency of shielding* defines the extent to which the signal induced on the anode is dependent on the signal below the grid. Bunemann et al. [63] calculate the inefficiency to be

$$\sigma = \frac{dE_P}{dE_Q} = \frac{d}{2\pi p} \ln \left( \frac{d}{2\pi r} \right), \quad (5.1)$$

where  $d$  is the pitch of the grid,  $r$  is the grid wire radius,  $p$  is the distance between the grid and the anode, and  $q$  is the distance between the cathode and the grid.  $E_P$  is the electric field associated with  $p$ , whilst  $E_Q$  is the field associated with  $q$ . The inefficiency can then be minimised by either increasing  $p$ , or making  $d$  and  $r$  comparable.

Obviously if  $d$  and  $r$  are comparable, then a large portion of the field lines would terminate on the grid rather than the anode. This is undesirable as the grid would absorb a significant portion of the signal. As a result, the fraction of field lines intercepted by the grid should be limited as much as possible. Bunemann et al. [63] provide a condition that (theoretically) ensures zero charge interception from the grid:

$$\frac{E_P}{E_Q} > \frac{1 + \rho}{1 - \rho} \quad \text{where } \rho = \frac{2\pi r}{d}. \quad (5.2)$$

This incidentally provides a limit on  $p$ , since  $E_p$  decreases with increasing  $p$ . In addition, the voltages used to determine the field ratio are physically limited by discharges and the high voltage rating of the pre-amplifiers. This means they cannot arbitrarily increased.

The matter is further complicated by the diffusion of electrons, which can cause cross contamination at the anode boundaries. This effect is largest for rapidly changing ionisation rates, so would most negatively impact on the deeper anodes. Furthermore, the probability of recombination increases with increasing travel time. To minimise these effects, both  $p$  and  $q$  should be minimised.

Martschini et al. [64] tested several different geometries for their new ionisation chamber. These experiments indicated that  $q = 39$  mm and  $p = 7$  mm were the optimum values. The VERA detector is a multi-purpose detector, and the isotopes used span from  $^{10}\text{Be}$  to  $^{236}\text{U}$ . Whilst small gains could be made by specialising for  $^{53}\text{Mn}$ , these geometry values should be approximately optimal. The FASMA detector must have a window height of 40 mm due to the vertical spread induced by the Enge, and the grid should be high enough above the window to ensure pair formation only occurs between the grid and anode. Hence, values of  $q = 50$  mm and  $p = 8$  mm were chosen, as indicated in Figure 5.2b. With these values, the inefficiency of shielding is  $\sigma = 2.13\%$ . The field ratio is then  $E_P/E_Q = 1.875$ .

Due to manufacturing constraints, the grid was constructed from 20  $\mu\text{m}$  diameter gold-coated tungsten wire with a pitch of 0.51 mm. For the proposed geometry, the condition for zero grid interception given in Equation 5.2 is  $E_P/E_Q > 1.281$ . Since the proposed field ratio exceeds this limit, the large majority of field lines should terminate on the anode, and not on the grid.



(a) The detector housing and entrance window. The window is missing the knife-edge shield in this image.



(b) The electrode stack with its slide-in utility. Note that the soldering bumps on the anode were later redone to lay flush with the anode.

**Figure 5.3:** Images of the FASMA detector during initial tests.

### 5.2.3 Detector Housing

The detector housing was designed with two things in mind, compatibility with the current set-up, and opportunity for future modifications. The full CAD schematic is pictured in Figure 5.4. The detector mount was left unchanged and as a result, the base of the chamber is considerably wider than the housing itself. Whilst this means that the window is not as close to the pole face as possible, the energy gain from the reduction in distance was not worth the inconvenience of implementing a new mount. The wider base also provides handles for easier manoeuvring within the Enge.

The lid, base, window, and all the flanges are sealed vacuum tight using O-rings. Although not visible in Figure 5.4, most flat surfaces have been recessed to reduce the total weight of the detector. The majority of screws are vented to ensure no outgassing can occur from trapped pockets of air. The Mesytec pre-amplifier box is mounted on the rear of the detector to ensure its operation does not affect the working gas, and to minimise the distance of travel for the unshaped signals. The window geometry is identical to the old detector, except the knife-edge shield is only 70 mm across to ensure the beam enters in the centre of the detector.

The detector gas is currently supplied through an elbow ConFlat flange. The detector is

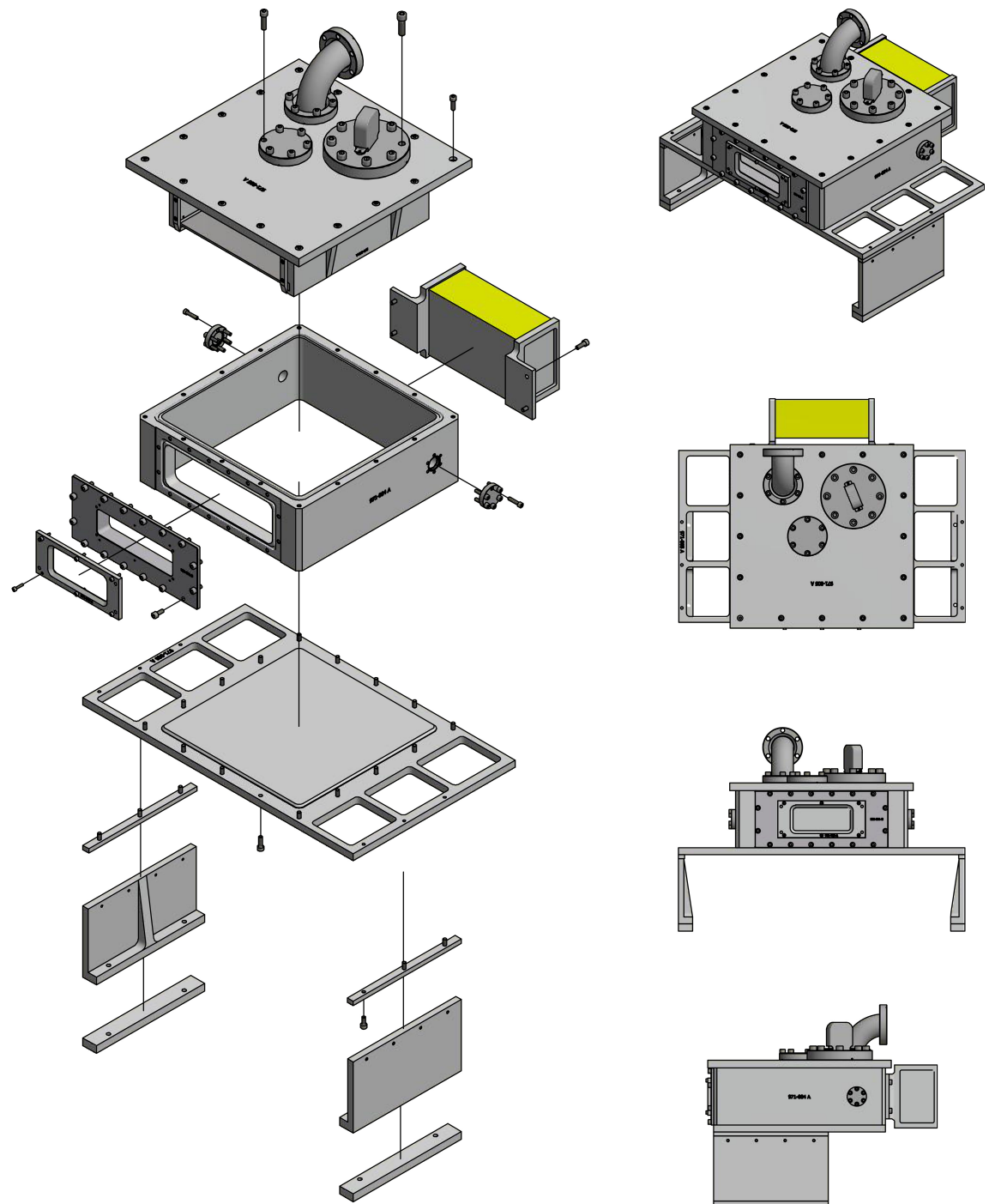


**Figure 5.4:** The CAD rendering of the FASMA detector. The anode stack is attached to the lid, which can be removed vertically so that the anode board can slide out. The Mesytec pre-amp box is mounted on the rear to minimise unshaped signal travel. The detector mount is designed to be compatible with the current mounting structure in the Enge spectrograph.

pressurised prior to the measurement, and remains stagnant throughout the measurement. Currently, this gas handling has worked well for the majority of measurements with any gas ageing being negligible. However, if problems like those presented in subsection 4.2.1 persist, then two mini-ConFlat holes have been machined into the sides of the detector so that a gas cycling system could be implemented in the future.

The electrode stack, pictured in Figure 5.3b, is supported by the lid of the detector. The electrodes and the grid slide into place and are insulated with Teflon slots. Because the sides of the stack are grounded, some field distortion will occur on the sides of the anode board, which is why the buffer anodes were implemented. The electronics are cabled from the back of the anode to the 25-pin D-sub feed-through embedded in the large ConFlat flange in the lid. This minimises the length of the wiring to get out of the detector. Currently, the anode and the grid are biased through the D-sub and the cathode is biased through a BNC connection in the final ConFlat flange in the lid. This set-up needs review, as discussed in section 5.4, because the maximum voltages have been limited by discharge problems in the initial tests.

The grid was manufactured using a grid winding device. The frame was mounted, and the device then mechanically wound the grid wire around the frame maintaining the desired tension. The pitch of the wire was adjustable. The winding produced two grids, on the top and bottom of the frame. One was secured with conductive epoxy that held the tension in the winding and ensured good electrical contact so that all wires were equally biased. The remaining wire was removed as excess. Currently the grid is only retained by the Teflon bars screwed place in Figure 5.3b, and the only tension is the residual tension from the winding process which has been enough to keep the wire taught. If the wires start to sag significantly as the detector matures, tensioning screws and insulated screw holes were machined into the sides of electrode stack so that the grid can be tensioned. The thread on these screws is very fine so that the grid wires are not snapped during tensioning.

#### 5.2.4 Predicted Resolution

The energy resolution calculated here is the derived from the FWHM of the signal. This definition was chosen to allow for easy comparison to experimentally observed energy resolutions. For the FASMA detector, the isobar suppression in the Enge spectrograph introduces energy straggling in both beams that can be estimated by Raytrace simulations. Although Raytrace will underestimate the energy tails, the FWHM should still be relatively accurate. Since the resolution is measured experimentally from the chromium peak, the energy width was sourced by simulating 181 MeV  $^{53}\text{Cr}$  ions at typical conditions of 3.45 Torr and 1.05 T. The FWHM resolution entering the detector is predicted to be  $\delta E_{\text{enge}} = 1262 \text{ keV}$ .

In addition to the energy distribution generated by the Enge, the 3.56  $\mu\text{m}$  mylar foil also induces some energy straggling. SRIM can predict this energy straggling with TRIM calculation by tracking the energy decrease for each particle. As SRIM uses Bohr straggling instead of the more realistic Yang straggling [57], a correction needs to be applied to the predicted straggling. Running this calculation using the output from the Raytrace simulation yields an energy straggling produced by the window of  $\delta E_{\text{wind}} = 589 \text{ keV}$ .

Currently, the wires running from the anode to the pre-amplifier box are unshielded, Teflon coated wires. This choice is minimalistic and may be revised if the lack of shielding turns out to cause a significant noise contribution. The pre-amplifier is a Mesytec MPR-16-L multi channel charge integrating system. It has 16 channels, which should be more

than adequate future anode designs. It includes a sensitivity switch that changes the amplification by a factor of five, and is able to hold a bias of up to  $\pm 1\text{ kV}$ . The quoted noise is less than 5 keV. The amplification and data acquisition remains the same as used for the old detector, so an estimated resolution per anode is 76.5 keV. Since we have 7 anodes, the total electronic noise is the RMS sum yielding  $\delta E_{\text{elec}} = 202\text{ keV}$ .

The detector gas also introduces energy straggling due to the stochastic nature of the stopping power. This effect is significantly larger for the individual anodes as different ions will deposit varying amounts of energy on each anode, dependent on the exact stochastic trajectory. The total energy signal is less affected since the ions deposit all their energy in the detector. However, the amount of energy lost through ionisation varies stochastically with each ion, though SRIM indicates that the total non-ionising channels are less than 1% and the straggle would be even smaller. An estimate from SRIM, corrected to represent Yang straggling instead of SRIM's use of Bohr straggling, suggests the contribution from the detector gas to the total energy signal is approximately  $\delta E_{\text{gas}} = 1413\text{ keV}$ .

Finally, the inefficiency of shielding due to the geometry and the dispersion of the beam also contribute to the uncertainty in the resolution. The uncertainty due to this effect, provided by Bunemann et al. [63], is

$$\delta E_{\text{geom}} = \frac{E_q}{E_p} \Delta E \sigma \frac{2w}{q}, \quad (5.3)$$

where  $\sigma$  is the inefficiency of shielding from Equation 5.1,  $w$  is the width of the beam,  $q$  is the distance between the grid and cathode, and  $\Delta E$  is the energy deposited by the ion. Given that the average beam width is  $w = 8\text{ mm}$  and  $q = 50\text{ mm}$ , the geometrical contribution to the energy resolution, calculated with 181 MeV deposited, is  $\delta E_{\text{geom}} = 1546\text{ keV}$ .

As a result, the total expected energy resolution is the RMS of these individual values. This estimate is  $\delta E_{\text{tot}} = 2523\text{ keV}$ . This is 1.39% for 181 MeV ions, the expected ion energy.

### 5.3 First Trial

After working through polishing, assembly, leak chasing, cabling, and several unsuspected hurdles; in early October, we were able to mount the detector in the Enge and get a beam into the detector. The +12 charge state was selected for manganese and terminal voltages of 13.600 MV for  $^{55}\text{Mn}$  and 14.121 MV for  $^{53}\text{Mn}$  were used. The Enge was filled with 4.6 Torr of nitrogen gas and operated at a field 1.072 T. Initially the detector was filled with 51.7 Torr of propane. As opposed to previous measurements, the gas behaved well and no peak drifting was observed throughout the measurements.

After finding the optimum pressure such that the crossover point aligned with the E3-E4 splitting, the spectra displayed in Figure 5.5 were produced. It is immediately clear that the separation is much cleaner than the spectra produced in section 4.2. Whilst the meteorite spectra were not indicative of the best performance of the old detector, these new spectra demonstrate separation at least as good, if not better than the optimum case for the old detector.

This is especially exciting due to the fact that these spectra were produced in sub-optimum conditions. During both runs that the FASMA detector was tested, the electrodes could not be fully biased as discharges occurred. In particular, the anode was at +295 V,

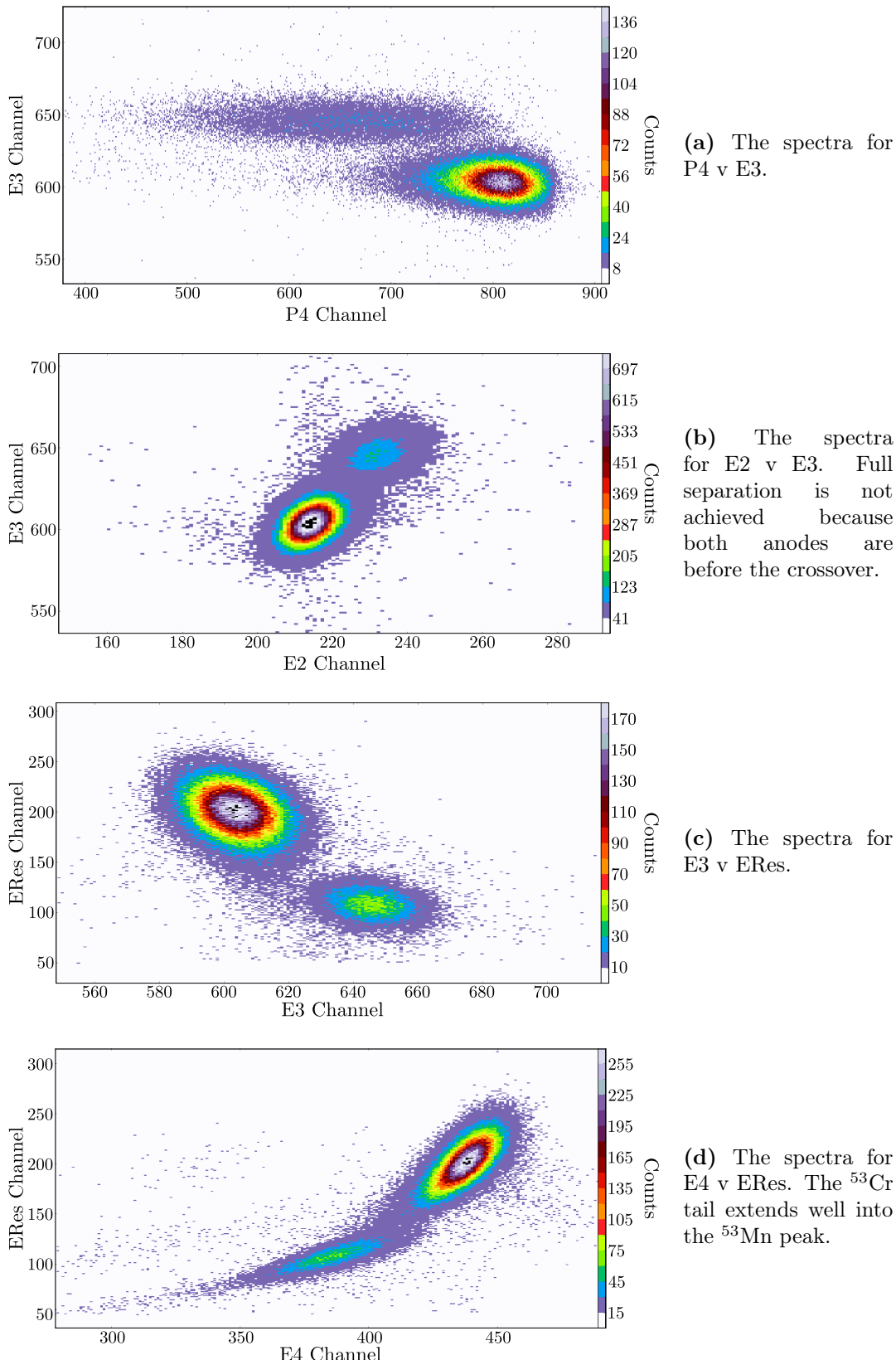


**Figure 5.5:** Example spectra from the  $^{53}\text{Mn}$  D9 standard (nominal ratio of  $1.36 \times 10^{-9}$ ) exhibiting the separation achieved with the new FASMA detector on its first trial run. Other spectra may be used for the final analysis but these four demonstrate the separation in E2, E3, E4 and ERes. E1 does not produce good separation and has a quite broad peak due to the small energy difference and the field distortion.

the grid at +100 V, and the cathode at -269 V, leading to non-optimal energy resolution. When this test was undertaken, the high voltage bias was run through unshielded wires inside the detector, and the grid and anode were unshielded outside as well. The cathode was connected with a BNC cable through a separate flange. Discharging occurred for the anode and the cathode so both connections need to be investigated. The proposed solutions are discussed further in section 5.4.

The E1 separation did not improve with the new design. This is unsurprising as the wire grid across the front of the electrode was removed to reduce scattering. This further increased the field distortion for this first anode. That being said, the other resolution improvements meant that the increased field distortion was partially cancelled out. Despite this, the separation was still significantly worse than the other anodes.

### 5.3.1 Angular Vetting

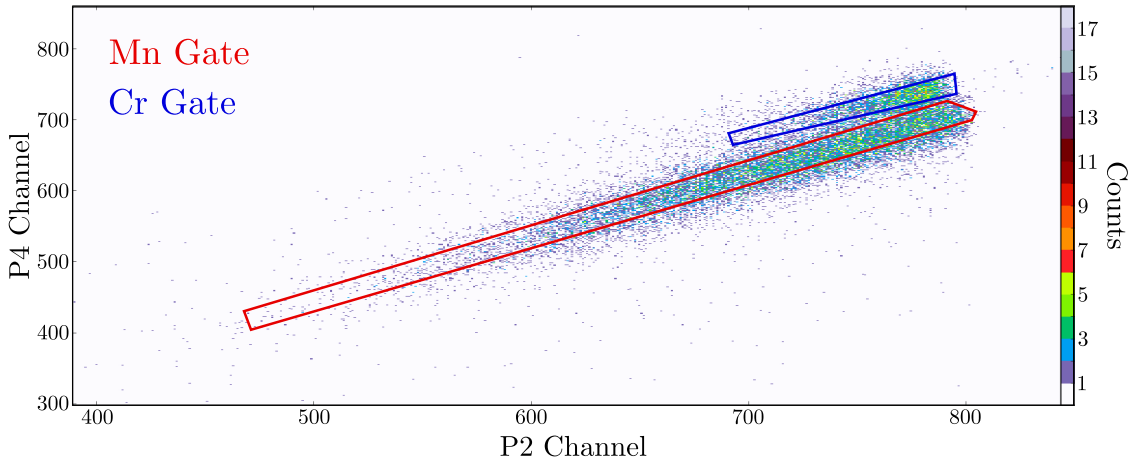
It is clear, particularly in Figure 5.5d, that the scattering tails still limit the sensitivity. Looking at the P2 v P4 spectrum should provide information that could be used to eliminate these scattering events. However, the spectrum yields somewhat surprising results. The P2 v P4 spectrum, plotted in Figure 5.6a, shows two distinct linear position relations, as opposed to the single bijective relation expected. When I gated each linear relation and examined the E4 v ERes spectrum, as displayed in Figures 5.6b and 5.6c, the linear relations appeared to be associated with a specific isobar. Because the relations were so close, they overlapped significantly so that the scattered particles from Cr were included in the Mn gate and vice versa. This is most obvious in Figure 5.6b where the red gate retains the manganese counts and only the scattering tail of the chromium counts.

This is extremely problematic. The aim of the angular trajectory suppression was to reject the scattered particles. However if rejecting these scattered particles included rejecting the manganese counts, then this is exceedingly counter-productive.

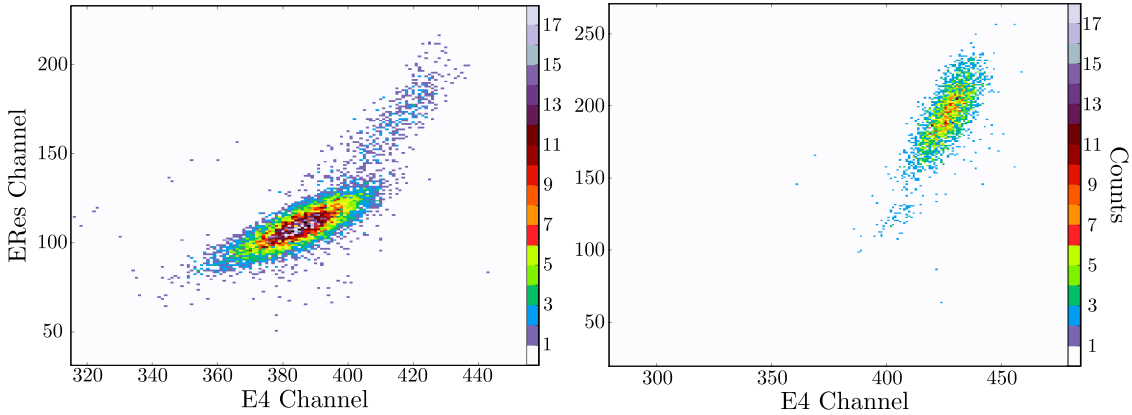
Both fortunately and unfortunately, there are several problems with this spectra that mean these results are unreliable. Firstly, the E4L and E4R anodes were amplified by different amounts. This means that the energy normalisation during the definition of P4 does not work. In particular, the normalisation is now energy dependent, which will produce an isobar separation in the P4 signal. Examining Figure 5.6a, it is clear that the difference between the two linear relations occurs in the P4 channel. Hence, it is expected that if the amplification for E4L and E4R is the same in future measurements, then only one linear relation will be observed that can be used to exclude scattered particles.

The second problem was also systematic. For the position spectra, approximately 89% of the total counts were binned in channel 1 for either P2 or P4. This is not visible from Figure 5.6a, but is quite clear in the full spectrum. It appears this problem affects chromium more than the manganese. Almost every manganese count is treated properly, but only 2.7% of the chromium counts survive. The cause for this remains unclear as the Fortran code appears identical. Unfortunately, given the late stage of these measurements, there was no time for a deeper investigation. Further measurements are required to resolve this.

Unfortunately, these issues with the angular spectra mean that the anti-scatter properties of the FASMA detector could not be investigated in this thesis. Comparison with the old detector using just the traditional gates is still available, and this should give an indication on whether the other adaptations were effective.



(a) The P2 v P4 spectrum with linear Mn and Cr gates shown. Only 11% of the total counts are shown, and the majority are manganese. Refer to main text for details.



(b) The E4 v ERes spectrum gated with the Mn gate shown above.

(c) The E4 v ERes spectrum gate with the Cr gate shown above.

**Figure 5.6:** The angular separation of the D9 standard (nominal ratio of  $1.36 \times 10^{-9}$ ). Two separate linear position relations exist for Mn and Cr which complicates any gating. However 89% of the counts are trapped in channel 1 for P2 or P4, so the derivation may be problematic.

### 5.3.2 Sensitivity

The increased length and the addition of another anode should allow for improved separation over the old detector. To get a rough estimate of the sensitivity limit from this new test, I designed gates for P4 v E3, E2 v E3, E3 v E4, and E3 v ERes (the Cr tail was too extensive in E4 v ERes to be useful). Applying them to a single standard and blank pair, the measured ratio was calculated using Equation 4.1. Renormalising, the background level for this trial run was  $1.23 \times 10^{-12}$ .

Table 5.1 compares this value to two runs done with the old detector. Since the meteorite measurements were hardly optimal conditions, as a more reliable comparison, I applied gates that cut a similar proportion of the  $^{53}\text{Mn}$  counts to a measurement run conducted in March 2017. The normalised background ratios presented are not particular useful as I did not correct for the chromium rate which varied with each blank sample. Since interfering chromium counts dominate the measured background, it is essential to normalise for the chromium count rate. This can be done by determining the chromium count rate from the total counts recorded for a variety blank samples. The observed  $^{53}\text{Mn}$

**Table 5.1:** Comparison of the background ratio for the trial run of the FASMA detector, and relevant runs with the old detector. All runs were done with  $\text{MnO}_2$ , however isobutane was used in March instead of propane. An estimate of at least 10% error is assumed for all ratios.

Measurement Run	Energy (MeV)	Raw Ratio	Scaled Ratio
FASMA Trial	180.4	$1.23 \times 10^{-12}$	$3.07 \times 10^{-13}$
Meteorites	195.7	$2.69 \times 10^{-12}$	$1.14 \times 10^{-12}$
March 2017	195.1	$4.30 \times 10^{-13}$	- <sup>a</sup>

<sup>a</sup> Above ratios scaled relative to March 2017 raw ratio.

background counts', which are primarily dominated by interfering  $^{53}\text{Cr}$  counts, can then be plotted against the chromium count rate. A linear relation is expected, where the measured background rate increases with the chromium abundance in the sample. Due to time constraints, such a variety of blank samples were not measured for this first trial run. A quick and dirty rescaling is a useful indicator of the relative chromium contribution, but does not give information on the absolute sensitivity. As a result, I rescaled each of the measured background ratios by the observed chromium count rate. In particular, the ratios were scaled against the March 2017 measurement as this had the lowest chromium count rate. The ratios are presented in Table 5.1.

From these values, we can see that the FASMA detector does at least as well, if not better, than the optimum conditions run in March. The scaled value is lower by more than the predicted error, which is substantial considering the lack of rigour applied. This is especially impressive since the FASMA detector trial was done with 15 MeV less energy and sub-optimal field values due to voltage discharges. The scaling also demonstrates the limitations of the peak drifting for the meteorite measurement. It is clear from these quick calculations that even without the anti-scattering features, the new FASMA detector is already more sensitive than the old detector.

## 5.4 Future Characterisation

These results are only the very first in a full characterisation that needs to be addressed. There are many aspects of the detector that need further attention and in this section, I will outline some of the obstacles that need to be tackled. Most of these tasks could have been achieved if the detector production was not delayed so significantly.

### 5.4.1 Electronics and Resolution

Currently, the FASMA detector is unable to hold the required voltages to optimise the energy resolution. Although it is difficult to quantify exactly how much the resolution will improve by once this problem is rectified, it will certainly make a difference.

Originally, all of the high voltage biases entered the detector through the 25-pin D-sub feed-through. In particular, the cathode and grid bias supply were only separated by 1 pin, despite the 1 kV potential difference. Although the single pin separation held up to a kV potential in atmospheric and vacuum testing, this was the most likely source of the discharge. As a result the cathode bias supply was modified and connected through a separate BNC flange. The cabling inside the detector however was still unshielded Teflon coated wiring. Since both the anode and cathode voltages were limited by discharging, it would indicate that the discharges originate from poor insulation in the detector housing,

rather than discharges between the wires themselves. There are several options to rectify this problem. Shielded wires could be used inside and outside the detector which would also improve the associated electronic noise. Both the cathode and grid could be supplied with BNC cables rather than the current bare cabling used currently. In particular, the inside of the BNC flange is currently a screw connection which could also be upgraded to a full BNC connection. Finally, the cathode and grid bias could be routed through the gas inlet pipe, as they were for the old detector, which would ensure total shielding from the housing and anode bias.

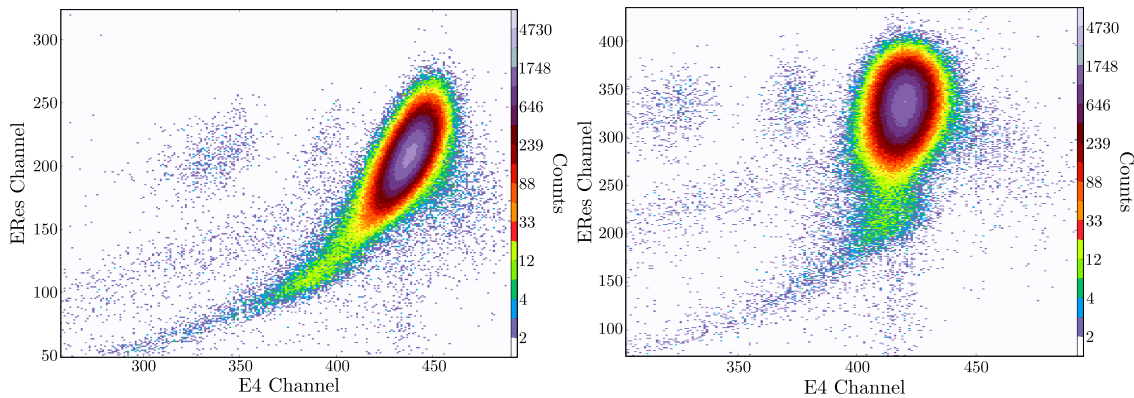
In the old detector, the total energy signal was measured from the cathode. In the FASMA detector, the total energy signal needs to be derived by summing the split anode signals. Once this is calculated, we will be able to compare the observed energy resolution to the predicted value and determine whether further optimisation can be made.

#### 5.4.2 Anode Design

The first problem that needs to be tackled is to fix the binning problem that is blocking the use of the angular information. Since this does not require any hardware changes, it should be a relatively straightforward fix. Secondly, the amplification of E4L and E4R needs to be equalised so that one linear relation exists in the P2 v P4 spectrum. Together, these would allow effective suppression of scattered particles.

The question remains whether more can be done to reduce the interference from the scattering tail in the E4 v ERes spectrum, which does not yet provide the envisaged separation power. Looking at the positioning of the manganese peak in Figure 5.5d, one might initially suppose that by reducing the separation in E4 or ERes, the manganese peak could be moved out of the chromium tail. We attempted to replicate this by decreasing the pressure, which elongates the energy loss curve, causing the crossover peak to be shifted into E4. This should remove the separation in E4 and cause the manganese peak to move out of the chromium tail. The comparison between two pressure values is given in Figure 5.7. By decreasing the pressure, we were able to reduce the separation in E4; however, the scattering tail followed the manganese peak and continued to produce significant interference.

This is not an altogether unsurprising result in light of the physics behind the scattering



(a) The E4 v ERes spectrum with 52 Torr in the detector.

(b) The E4 v ERes spectrum with 47 Torr in the detector.

**Figure 5.7:** Comparison of how the scattering tail varies with pressure in the detector. The tail follows the manganese peak. The other peaks present in the spectra are the result of pileup and signal dropping in individual anodes.

tail. A scattered particle travels on an angular trajectory such that the energy deposited on each anode is inflated by  $\sec\theta$  compared to the normal trajectory. Since the  $^{53}\text{Mn}$  and  $^{53}\text{Cr}$  energy loss profiles are very qualitatively similar, there will always be scattered  $^{53}\text{Cr}$  ions that produce the same ionisation curve, regardless of the precise pressure value. This is an important realisation because it means that the scattering cannot be eliminated by clever anode splitting, because the creating of ion pairs is independent of the anode structure. As a result, it appears there are minimal benefits to be gained by fine tuning the exact anode splittings.

Currently, the copper plating on the fibreglass anode board is only one sided so pins were drilled through the board and soldered flush with the surface to provide an electrical contact. To achieve an appropriate connection, the solder at these contacts is slightly raised above the board, which can alter the field geometry in this region. A new type of fibreglass anode board is being manufactured that will be coated on both sides such that the electrical contact can be attached to the non-active side of the anode board. This would mean the active side is completely flat, which should improve the field geometry.

#### 5.4.3 Other Isotopes

Because of the flexibility of the FASMA detector, there is the potential to expand its use for other isotopes. Ongoing research into Zirconium-93 is being conducted at the ANU. Currently,  $^{93}\text{Zr}$  uses an 8 anode ionisation chamber without the Enge. However there is the potential that the use of the Enge could be beneficial, and this opens up future pathways for an anode design specifically for  $^{93}\text{Zr}$ . Similarly, Selenium-79 has been proposed for study and could see its first applications in the new detector.



---

# Conclusion

---

In this thesis, we have investigated the construction and implementation of the new Flexible Anti-Scattering Multi-Anode (FASMA) detector, which has been specifically optimised for Accelerator Mass Spectrometry (AMS) measurements of  $^{53}\text{Mn}$ . The proposal for a new detector was motivated by the fact that the minimum achievable sensitivity of the background  $^{53}\text{Mn}/^{55}\text{Mn}$  ratio was, at best, in the low  $10^{-13}$  range. The AMS group at TU Munich was able to demonstrate a sensitivity of  $7 \times 10^{-15}$  [6] using their gas filled magnet set-up. Since the ANU has a similar gas-filled magnet and can provide the same energies, we should be aiming for comparable sensitivities, which would allow for an expansion of  $^{53}\text{Mn}$  applications.

Firstly, we investigated the positioning of the detector inside the Enge spectrograph through Raytrace simulations. It was determined that the current detector placement is appropriate given that the separation between the isobars is mostly optimised. The power of the isobar suppression can be increased for low ratio samples at the expense of the energy available for the detector. The isobar separation in the multi-anode detector was then modelled using SRIM to determine the appropriate anode splittings for  $^{53}\text{Mn}$ , given optimal operation conditions. These simulations revealed the challenges in separating  $^{53}\text{Mn}$  from its isobar  $^{53}\text{Cr}$ . Because  $^{53}\text{Mn}$  has a higher atomic number than  $^{53}\text{Cr}$ , the scattering tails from  $^{53}\text{Cr}$ , generated by low-probability angular trajectories, directly overlap with the  $^{53}\text{Mn}$  energy loss peak. In the worst case scenarios, the angular  $^{53}\text{Cr}$  trajectories can effectively simulate a normal  $^{53}\text{Mn}$  trajectory, which produces background interference that is difficult to separate.

To exhibit the measurement process and the limitations of the old detector, samples from several iron meteorites were measured for their  $^{53}\text{Mn}/^{55}\text{Mn}$  and  $^{60}\text{Fe}/\text{Fe}$  ratios. Despite being preliminary data that needs to be confirmed over several more accelerator beam times, these ratios have made a significant contribution to the  $^{53}\text{Mn}$  and  $^{60}\text{Fe}$  meteorite data. The accepted background for these measurements was relatively high. However, due to the high ratios found in meteorites, the uncertainty in this background was small compared to other systematic uncertainties in the measurement.

Finally the design principles behind the FASMA detector were deconstructed in terms of the methodology used to suppress scattered particles and the improvements to the energy resolution. The FASMA detector was tested and found to have good separation that was comparably better than the old detector, even under sub-optimal detector conditions and without the scattering suppression. Unfortunately, the scattering suppression, achieved by comparing the position signals from the 2<sup>nd</sup> and 4<sup>th</sup> diagonally split anodes, had some teething issues that meant we were not able to quantify the associated sensitivity increase. These issues are predicted to be minor inconveniences only, and within the next few months the FASMA detector should be fully operational and optimised. This will herald a new

age in  $^{53}\text{Mn}$  accelerator mass spectrometry at the ANU.

## 6.1 Future Directions

The FASMA detector should increase the sensitivity of  $^{53}\text{Mn}$  measurement at the ANU by at least an order of magnitude, which will open up its applications as a dating tool for environmental and astrophysical studies. As the ANU is one of only two institutions in the world that actively measure  $^{53}\text{Mn}$  with AMS, the demonstration of this sensitivity increase could widen the interest in  $^{53}\text{Mn}$  AMS measurements globally. Already, institutions like the University of Cologne are developing  $^{53}\text{Mn}$  capabilities. If the scattering suppression proves powerful, this could widen  $^{53}\text{Mn}$  applicability to lower energy detectors, which would dramatically increase the availability of  $^{53}\text{Mn}$  data. Due to the inherent difficulties, smaller detectors would still be only able to measure higher ratios.

Whilst the FASMA detector looks set to improve  $^{53}\text{Mn}$  prospects, there are other technical areas that would improve the accuracy and reliability of measurements. Currently, for all isotopes examined with the Enge spectrograph, the stable isotope ( $^{55}\text{Mn}$  for our specific case) is measured by changing the field of the injecting magnet, the terminal voltage, and the Wien filter. This means only 3 current measurements are made for each sample, which gives poor resolution on the variability of the current. Fast cycling, where the stable isotope is collected off the beam line in short time intervals (as described in subsection 2.4.1), has already been implemented for  $^{36}\text{Cl}$  and actinide measurements. By expanding the number of isotopes that can use fast cycling, the accuracy and reproducibility of the measured ratio would be improved. This implementation is time consuming, which is why it has not yet been achieved.

Another long term innovation that is currently being investigated is isobar suppression by laser photo-detachment [65]. By introducing counter-propagating lasers of a specific frequency, an electron can be liberated from the negative ion of the isobar, whilst not having enough energy to liberate the electron from the radioisotope:



This naturally requires that the atomic/molecular negative ion for the radioisotope have a higher electron affinity than the corresponding negative ion of the isobar. Whilst this principle has been demonstrated, practically much more work needs to be done before it can be implemented. Supposing it did work, another level of isobar suppression would be included which would allow for even higher sensitivities than are currently accessible.

*“The rest is silence.”*

- Hamlet (5.2.256), William Shakespeare.

# Beam Width Fitting

As discussed in subsection 3.2.3, the inference of the beam width from the count rate in the detector does require some mathematical deduction. In this appendix, I will demonstrate the methodology I used to extract the beam width from the experimental data produced in the August run.

From the spectra recorded by the ionisation chamber detector, the average count rate can be determined by gating the counts of interest (in particular chromium) and comparing to the number of pulsar signals received. Standard counting statistics apply for these count rates but since each measurement contains over 10,000 total counts, these uncertainties are usually negligible compared to other uncertainties like ion source fluctuations. Each count rate was associated with a magnetic field determined by the NMR fluxmeter in the Enge.

In this analysis, I assumed that the beam had a Gaussian spatial distribution. Although this assumption is incorrect (it underestimates the tails), it is the best available and is the same assumption that the Raytrace program uses. As the Gaussian beam is passed across the knife edge window and into the detector, the count rate will be proportional to the integral of the Gaussian. The integral of a Gaussian is given by the *error function*

$$\text{erf}(x) = \frac{1}{\sqrt{\pi}} \int_{-x}^x e^{-t^2} dt. \quad (\text{A.1})$$

Since we want to integrate from infinity to a given  $x$  (representing how much of the beam is in the detector), the specific form of the integral is:

$$\int_x^\infty Ae^{-B(t-C)^2} dt = \frac{A}{2} \sqrt{\frac{\pi}{B}} \left( 1 + \text{erf} \left( \sqrt{B}(C-x) \right) \right), \quad (\text{A.2})$$

where  $A$ ,  $B$  and  $C$  are simply positive constants determining the Gaussian shape. In this coordinate system, the beam remains centred on the origin and the knife edge window exists at a distance  $x$  that is decreasing as the beam moves into the detector. The function is qualitatively mirrored if we consider the detector as stationary and the beam centre given by  $x$ ; in particular we need only make the coordinate transformation  $x \rightarrow -x$ .

In addition to the entrance of the beam, the exit of the beam needs to be included to produce the desired smoothed top-hat function. Combining the above reasoning, the smoothed top-hat function that is proportional to the observed count rate is given by:

$$\text{smth}(x) = \frac{A}{2} \sqrt{\frac{\pi}{B}} \left( \text{erf} \left( \sqrt{B}(x-C) \right) - \text{erf} \left( \sqrt{B}(x-D) \right) \right), \quad (\text{A.3})$$

where  $A$  is an arbitrary scaling constant to match the maximum count rate,  $B$  is related

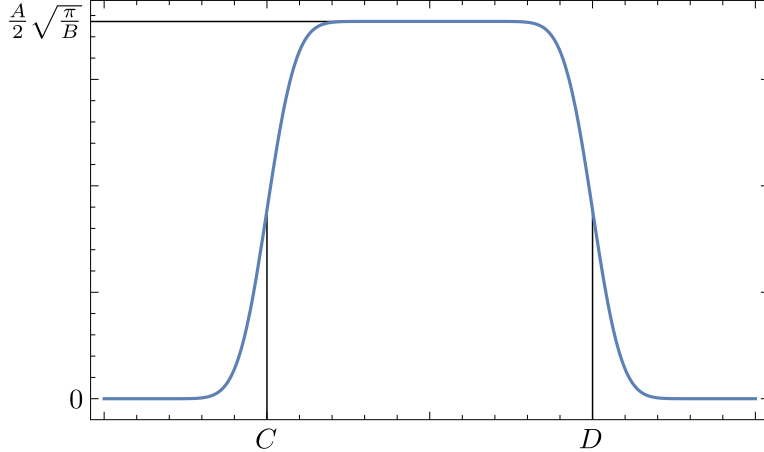


**Figure A.1:** The generalised form of the smoothed top-hat function given in A.3 that is proportional to the observed count rate.

to the width of the beam and determines the smoothness of the drop off associated with beam entry/exit, and  $C$  and  $D$  are the left and right positions of the knife edge window respectively. This produces the form observed in Figure A.1.

Equation A.3 can then be fitted to the experimental data where  $x$  is the magnetic field in the Enge and the output is the observed count rate. Mathematica will then yield a least squares estimate of the parameters  $A$ ,  $B$ ,  $C$  and  $D$  with associated fitting errors. The standard deviation can be easily derived from  $B$  by the relation  $\sigma = (2B)^{-\frac{1}{2}}$ . However this standard deviation is still in terms of the magnetic field. Since the window width of the detector is known to be  $9.87\text{ cm}$ , a simple conversion factor is given by  $z = 9.87(D - C)^{-1}\text{ cm kG}^{-1}$ . Thus the beam width in  $\text{cm}$  is given by  $z\sigma$ . This was precisely how the values in ?? were determined.

---

# Meteorite Data

---

In this appendix, I present the raw and intermediate data used to derive the final ratios presented in Chapter 4. A table is presented for each measurement set containing the raw counts, currents and measured ratios, as well as the final ratios for two standards. The calculations for the normalisation factors and blank corrections used to derive the standard ratios are simple and assumed to be accessible to anyone wanting to reproduce or correct the data presented. All the data is presented chronologically.

The error in the normalised ratios presented below are statistical uncertainties only. Systematic uncertainties like reproducibility, uncertainty in the standard, and uncertainty in the half-life are included for Table 4.4 but not in these tables. In particular, the ratios in Table 4.4 are weighted averages of the two measurement sets (for  $^{53}\text{Mn}$  at least) with the uncertainty due to reproducibility estimated, and the uncertainty in the standard due to the uncertainty in the half-life included.

## B.1 Manganese Data

For  $^{53}\text{Mn}$ , two standards were measured. The D9 standard is a standard prepared by dilution series from  $^{53}\text{Mn}$  collected from a proton-irradiated copper beam dump from the Paul Scherrer Institute (PSI). It has a nominal ratio of  $(1384 \pm 52) \times 10^{-9}$  which was determined by extensive AMS analysis against the Greg Herzog standard. The Greg Herzog standard is the only current  $^{53}\text{Mn}$  AMS standard that has been measured by activity measurements. There is no quoted uncertainty due to the precision of the measurement and every  $^{53}\text{Mn}$  measurement is calibrated against this activity measurement. Because the half-life of  $^{53}\text{Mn}$  is known only with a 10% uncertainty, the final absolute ratios reported in Table 4.4 have this 10% uncertainty included from the Greg Herzog standard.

Because the Greg Herzog standard was only measured once in each measurement set, additional uncertainty was included due to the observed fluctuation in the D9 ratio which was measured three times each set. Three different gate structures are presented, as described in section 4.2. They each represent independent analysis and so the value with the lowest uncertainty was selected to report in Table 4.4 which, in all cases, was the normal gate for the D9 standard.

Table B.1 and Table B.2 include the measured ratios and uncertainties for the first and second measurement set respectively. The standard ratios presented are background corrected and normalised. The error in the measured ratio is the root mean square of the counting uncertainty and the drift uncertainty, determined from the gate ratios. The uncertainty associated with the drift for the first (second) measurement set was estimated to be 3% (7%) for the tight gate, 2% (4%) for the normal gate, and 5.5% (5%) for the wide gate.

**Table B.1:** The raw and derived data for the **first** measurement set taken on the 28<sup>th</sup> of September, 2017. The reported current is the average of the three measured. All uncertainties are  $1\sigma$ .

Sample	Counts	Meas. Ratio	MR Error	D9 Ratio	GH Ratio
D9a 2016-1		Current: 0.507 nA	Pulser: 395		
Tight	196	$2.037 \times 10^{-10}$	$1.578 \times 10^{-11}$	-	-
Normal	323	$3.356 \times 10^{-10}$	$1.984 \times 10^{-11}$	-	-
Wide	887	$9.217 \times 10^{-10}$	$5.939 \times 10^{-11}$	-	-
TSH Blank		Current: 1.873 nA	Pulser: 1103		
Tight	14	$1.411 \times 10^{-12}$	$3.795 \times 10^{-13}$	-	-
Normal	54	$5.443 \times 10^{-12}$	$7.487 \times 10^{-13}$	-	-
Wide	1257	$1.267 \times 10^{-10}$	$7.832 \times 10^{-12}$	-	-
TSI San Angelo		Current: 0.342 nA	Pulser: 396		
Tight	601	$9.241 \times 10^{-10}$	$4.679 \times 10^{-11}$	$(5.07 \pm 0.36) \times 10^{-9}$	$(5.87 \pm 1.73) \times 10^{-9}$
Normal	956	$1.462 \times 10^{-9}$	$5.571 \times 10^{-11}$	$(4.79 \pm 0.26) \times 10^{-9}$	$(5.41 \pm 1.59) \times 10^{-9}$
Wide	2450	$3.767 \times 10^{-9}$	$2.207 \times 10^{-10}$	$(5.27 \pm 0.55) \times 10^{-9}$	$(4.15 \pm 1.23) \times 10^{-9}$
TSI Sacr. Mtns.		Current: 0.341 nA	Pulser: 395		
Tight	691	$1.068 \times 10^{-9}$	$5.174 \times 10^{-11}$	$(5.86 \pm 0.41) \times 10^{-9}$	$(6.79 \pm 2.00) \times 10^{-9}$
Normal	1119	$1.729 \times 10^{-9}$	$6.220 \times 10^{-11}$	$(5.66 \pm 0.30) \times 10^{-9}$	$(6.40 \pm 1.88) \times 10^{-9}$
Wide	2677	$4.137 \times 10^{-9}$	$2.412 \times 10^{-10}$	$(5.81 \pm 0.61) \times 10^{-9}$	$(4.57 \pm 1.36) \times 10^{-9}$
TSI Zeramra		Current: 2.039 nA	Pulser: 349		
Tight	1972	$5.773 \times 10^{-10}$	$2.166 \times 10^{-11}$	$(3.17 \pm 0.20) \times 10^{-9}$	$(3.66 \pm 1.07) \times 10^{-9}$
Normal	3214	$9.409 \times 10^{-10}$	$2.509 \times 10^{-11}$	$(3.07 \pm 0.14) \times 10^{-9}$	$(3.47 \pm 1.01) \times 10^{-9}$
Wide	8386	$2.455 \times 10^{-9}$	$1.377 \times 10^{-10}$	$(3.37 \pm 0.36) \times 10^{-9}$	$(2.65 \pm 0.79) \times 10^{-9}$
TSI Tamentit		Current: 1.620 nA	Pulser: 364		
Tight	1374	$4.854 \times 10^{-10}$	$1.958 \times 10^{-11}$	$(2.66 \pm 0.17) \times 10^{-9}$	$(2.85 \pm 0.83) \times 10^{-9}$
Normal	2186	$7.722 \times 10^{-10}$	$2.261 \times 10^{-11}$	$(2.52 \pm 0.12) \times 10^{-9}$	$(3.08 \pm 0.90) \times 10^{-9}$
Wide	5656	$1.998 \times 10^{-9}$	$1.131 \times 10^{-10}$	$(2.71 \pm 0.30) \times 10^{-9}$	$(2.13 \pm 0.63) \times 10^{-9}$
D9a 2016-1		Current: 0.745 nA	Pulser: 398		
Tight	375	$3.313 \times 10^{-10}$	$1.979 \times 10^{-11}$	-	-
Normal	651	$5.752 \times 10^{-10}$	$2.531 \times 10^{-11}$	-	-
Wide	1602	$1.415 \times 10^{-9}$	$8.550 \times 10^{-11}$	-	-
TSH Carthage		Current: 0.499 nA	Pulser: 379		
Tight	452	$4.976 \times 10^{-10}$	$2.776 \times 10^{-11}$	$(2.36 \pm 0.17) \times 10^{-9}$	$(3.16 \pm 0.94) \times 10^{-9}$
Normal	707	$7.783 \times 10^{-10}$	$3.315 \times 10^{-11}$	$(2.23 \pm 0.12) \times 10^{-9}$	$(2.87 \pm 0.84) \times 10^{-9}$
Wide	2049	$2.256 \times 10^{-9}$	$1.337 \times 10^{-10}$	$(2.75 \pm 0.28) \times 10^{-9}$	$(2.43 \pm 0.73) \times 10^{-9}$
TSH Charcas		Current: 1.14 nA	Pulser: 375		
Tight	879	$4.278 \times 10^{-10}$	$1.931 \times 10^{11-}$	$(2.03 \pm 0.13) \times 10^{-9}$	$(2.71 \pm 0.80) \times 10^{-9}$
Normal	1423	$6.926 \times 10^{-10}$	$2.300 \times 10^{-11}$	$(1.98 \pm 0.09) \times 10^{-9}$	$(2.55 \pm 0.75) \times 10^{-9}$
Wide	3898	$1.897 \times 10^{-9}$	$1.087 \times 10^{-10}$	$(2.28 \pm 0.24) \times 10^{-9}$	$(2.02 \pm 0.60) \times 10^{-9}$
TSH Chulafinnee		Current: 0.304 nA	Pulser: 382		
Tight	285	$5.112 \times 10^{-10}$	$3.394 \times 10^{-11}$	$(2.43 \pm 0.19) \times 10^{-9}$	$(3.24 \pm 0.97) \times 10^{-9}$
Normal	486	$8.717 \times 10^{-10}$	$4.321 \times 10^{-11}$	$(2.50 \pm 0.15) \times 10^{-9}$	$(3.22 \pm 0.95) \times 10^{-9}$
Wide	1332	$2.389 \times 10^{-9}$	$1.468 \times 10^{-10}$	$(2.92 \pm 0.30) \times 10^{-9}$	$(2.58 \pm 0.77) \times 10^{-9}$
TSH Dalton		Current: 1.475 nA	Pulser: 369		
Tight	1742	$6.668 \times 10^{-10}$	$2.560 \times 10^{-11}$	$(3.17 \pm 0.18) \times 10^{-9}$	$(4.23 \pm 1.24) \times 10^{-9}$
Normal	2850	$1.091 \times 10^{-9}$	$2.989 \times 10^{-11}$	$(3.13 \pm 0.13) \times 10^{-9}$	$(4.03 \pm 1.18) \times 10^{-9}$
Wide	7023	$2.688 \times 10^{-9}$	$1.513 \times 10^{-10}$	$(3.30 \pm 0.33) \times 10^{-9}$	$(2.92 \pm 0.87) \times 10^{-9}$

TSH Durango	Current: 1.274 nA	Pulser: 351			
Tight	983	$4.577 \times 10^{-10}$	$2.004 \times 10^{-11}$	$(2.17 \pm 0.13) \times 10^{-9}$	$(2.90 \pm 0.85) \times 10^{-9}$
Normal	1651	$7.688 \times 10^{-10}$	$2.438 \times 10^{-11}$	$(2.20 \pm 0.10) \times 10^{-9}$	$(2.83 \pm 0.83) \times 10^{-9}$
Wide	4666	$2.173 \times 10^{-9}$	$1.237 \times 10^{-10}$	$(3.64 \pm 0.27) \times 10^{-9}$	$(2.33 \pm 0.69) \times 10^{-9}$
TSH Plymouth	Current: 0.667 nA	Pulser: 381			
Tight	658	$5.397 \times 10^{-10}$	$2.655 \times 10^{-11}$	$(2.56 \pm 0.17) \times 10^{-9}$	$(3.43 \pm 1.01) \times 10^{-9}$
Normal	1041	$8.538 \times 10^{-10}$	$3.149 \times 10^{-11}$	$(2.45 \pm 0.12) \times 10^{-9}$	$(3.15 \pm 0.92) \times 10^{-9}$
Wide	2881	$2.363 \times 10^{-9}$	$1.372 \times 10^{-10}$	$(2.88 \pm 0.30) \times 10^{-9}$	$(2.55 \pm 0.76) \times 10^{-9}$
D9a 2016-1	Current: 0.789 nA	Pulser: 391			
Tight	396	$2.674 \times 10^{-10}$	$1.565 \times 10^{-11}$	-	-
Normal	642	$4.335 \times 10^{-10}$	$1.918 \times 10^{-11}$	-	-
Wide	1593	$1.076 \times 10^{-9}$	$6.501 \times 10^{-11}$	-	-
$\sigma$ -Al Blank 4	Current: 0.597 nA	Pulser: 1187			
Tight	1	$2.938 \times 10^{-13}$	$2.940 \times 10^{-13}$	-	-
Normal	3	$8.815 \times 10^{-13}$	$5.092 \times 10^{-13}$	-	-
Wide	165	$4.848 \times 10^{-11}$	$4.062 \times 10^{-12}$	-	-
GH Standard	Current: 1.079 nA	Pulser: 747			
Tight	163	$4.211 \times 10^{-11}$	$3.532 \times 10^{-12}$	$(1.94 \pm 0.19) \times 10^{-10}$	-
Normal	291	$7.518 \times 10^{-11}$	$4.657 \times 10^{-12}$	$(2.01 \pm 0.17) \times 10^{-10}$	-
Wide	1370	$4.540 \times 10^{-10}$	$2.169 \times 10^{-11}$	$(2.93 \pm 0.90) \times 10^{-10}$	-

**Table B.2:** The raw and derived data for the **second** measurement set taken on the 28<sup>th</sup> of September, 2017. The reported current is the average of the three measured. All uncertainties are  $1\sigma$ . The GH Ratios are incorrect, see footnote for explanation.

Sample	Counts	Meas. Ratio	MR Error	D9 Ratio	GH Ratio
D9a 2016-1	Current: 0.867 nA	Pulser: 792			
Tight	823	$2.497 \times 10^{-10}$	$1.952 \times 10^{-11}$	-	-
Normal	1427	$4.329 \times 10^{-10}$	$2.077 \times 10^{-11}$	-	-
Wide	3337	$1.012 \times 10^{-9}$	$5.357 \times 10^{-11}$	-	-
TSI Blank	Current: 1.642 nA	Pulser: 1174			
Tight	3	$3.242 \times 10^{-13}$	$1.885 \times 10^{-13}$	-	-
Normal	22	$2.377 \times 10^{-12}$	$5.156 \times 10^{-13}$	-	-
Wide	405	$4.376 \times 10^{-11}$	$3.085 \times 10^{-12}$	-	-
TSH Blank	Current: 1.672 nA	Pulser: 1175			
Tight	8	$8.480 \times 10^{-13}$	$3.056 \times 10^{-13}$	-	-
Normal	41	$4.346 \times 10^{-12}$	$7.006 \times 10^{-13}$	-	-
Wide	594	$6.296 \times 10^{-11}$	$4.073 \times 10^{-12}$	-	-
TSI San Angelo	Current: 0.297 nA	Pulser: 387			
Tight	489	$8.871 \times 10^{-10}$	$7.393 \times 10^{-11}$	$(5.09 \pm 0.52) \times 10^{-9}$	$(3.42 \pm 0.56) \times 10^{-9}$
Normal	814	$1.477 \times 10^{-9}$	$7.854 \times 10^{-11}$	$(4.87 \pm 0.32) \times 10^{-9}$	$(3.29 \pm 0.43) \times 10^{-9}$
Wide	1925	$3.492 \times 10^{-9}$	$1.919 \times 10^{-10}$	$(5.08 \pm 0.38) \times 10^{-9}$	$(2.92 \pm 0.46) \times 10^{-9}$
TSI Sacr. Mtns.	Current: 0.284 nA	Pulser: 795			
Tight	1090	$1.006 \times 10^{-9}$	$7.671 \times 10^{-11}$	$(5.77 \pm 0.55) \times 10^{-9}$	$(3.88 \pm 0.62) \times 10^{-9}$
Normal	1858	$1.714 \times 10^{-9}$	$7.928 \times 10^{-11}$	$(5.66 \pm 0.34) \times 10^{-9}$	$(3.82 \pm 0.49) \times 10^{-9}$
Wide	4334	$3.999 \times 10^{-9}$	$2.090 \times 10^{-10}$	$(5.83 \pm 0.42) \times 10^{-9}$	$(3.35 \pm 0.52) \times 10^{-9}$
TSI Zeramra	Current: 1.037 nA	Pulser: 759			

Tight	3474	$9.190 \times 10^{-10}$	$6.619 \times 10^{-11}$	$(5.27 \pm 0.49) \times 10^{-9}$	$(3.54 \pm 0.56) \times 10^{-9}$
Normal	6058	$1.602 \times 10^{-9}$	$6.733 \times 10^{-11}$	$(5.29 \pm 0.30) \times 10^{-9}$	$(3.57 \pm 0.46) \times 10^{-9}$
Wide	15079	$3.989 \times 10^{-9}$	$2.021 \times 10^{-10}$	$(5.81 \pm 0.41) \times 10^{-9}$	$(3.34 \pm 0.52) \times 10^{-9}$
TSI Tamentit					
		Current: 1.037 nA	Pulser: 769		
Tight	2109	$4.022 \times 10^{-10}$	$2.949 \times 10^{-11}$	$(2.31 \pm 0.22) \times 10^{-9}$	$(1.55 \pm 0.25) \times 10^{-9}$
Normal	3815	$7.276 \times 10^{-10}$	$3.140 \times 10^{-11}$	$(2.40 \pm 0.14) \times 10^{-9}$	$(1.62 \pm 0.21) \times 10^{-9}$
Wide	9311	$1.776 \times 10^{-9}$	$9.068 \times 10^{-11}$	$(2.55 \pm 0.19) \times 10^{-9}$	$(1.46 \pm 0.23) \times 10^{-9}$
GH Standard					
		Current: 1.49 nA	Pulser: 786		
Tight	223	$6.765 \times 10^{-11}$	$6.554 \times 10^{-12}$	$(3.84 \pm 0.30) \times 10^{-10}$	-
Normal	393	$1.192 \times 10^{-10}$	$7.676 \times 10^{-12}$	$(3.86 \pm 0.44) \times 10^{-10}$	-
Wide	1175	$3.565 \times 10^{-10}$	$2.064 \times 10^{-11}$	$(4.51 \pm 0.53) \times 10^{-10}$	-
D9a Mn					
		Current: 0.890 nA	Pulser: 396		
Tight	388	$2.329 \times 10^{-10}$	$2.014 \times 10^{-11}$	-	-
Normal	680	$4.081 \times 10^{-10}$	$2.261 \times 10^{-11}$	-	-
Wide	1608	$9.651 \times 10^{-10}$	$5.392 \times 10^{-11}$	-	-
TSH Carthage					
		Current: 0.198 nA	Pulser: 398		
Tight	171	$4.532 \times 10^{-10}$	$4.698 \times 10^{-11}$	$(3.16 \pm 0.39) \times 10^{-9}$	$(1.75 \pm 0.30) \times 10^{-9}$
Normal	327	$8.666 \times 10^{-10}$	$5.915 \times 10^{-11}$	$(3.16 \pm 0.25) \times 10^{-9}$	$(1.93 \pm 0.27) \times 10^{-9}$
Wide	855	$2.266 \times 10^{-9}$	$1.373 \times 10^{-10}$	$(3.46 \pm 0.31) \times 10^{-9}$	$(1.88 \pm 0.30) \times 10^{-9}$
TSH Chulafinnee					
		Current: 1.037 nA	Pulser: 370		
Tight	568	$3.082 \times 10^{-10}$	$2.512 \times 10^{-11}$	$(2.16 \pm 0.22) \times 10^{-9}$	$(1.19 \pm 0.19) \times 10^{-9}$
Normal	1122	$6.088 \times 10^{-10}$	$3.039 \times 10^{-11}$	$(2.21 \pm 0.14) \times 10^{-9}$	$(1.35 \pm 0.18) \times 10^{-9}$
Wide	2991	$1.623 \times 10^{-9}$	$8.641 \times 10^{-11}$	$(2.40 \pm 0.18) \times 10^{-9}$	$(1.33 \pm 0.21) \times 10^{-9}$
TSH Dalton					
		Current: 1.155 nA	Pulser: 395		
Tight	1121	$5.118 \times 10^{-10}$	$3.895 \times 10^{-11}$	$(3.59 \pm 0.36) \times 10^{-9}$	$(1.97 \pm 0.31) \times 10^{-9}$
Normal	2092	$9.551 \times 10^{-10}$	$4.354 \times 10^{-11}$	$(3.48 \pm 0.21) \times 10^{-9}$	$(2.12 \pm 0.27) \times 10^{-9}$
Wide	5251	$2.397 \times 10^{-9}$	$1.244 \times 10^{-10}$	$(3.58 \pm 0.27) \times 10^{-9}$	$(1.99 \pm 0.31) \times 10^{-9}$
TSH Durango					
		Current: 1.086 nA	Pulser: 382		
Tight	605	$3.309 \times 10^{-10}$	$2.256 \times 10^{-11}$	$(2.32 \pm 0.22) \times 10^{-9}$	$(1.27 \pm 0.20) \times 10^{-9}$
Normal	1190	$6.513 \times 10^{-10}$	$3.683 \times 10^{-11}$	$(2.37 \pm 0.17) \times 10^{-9}$	$(1.45 \pm 0.19) \times 10^{-9}$
Wide	3168	$1.734 \times 10^{-9}$	$8.141 \times 10^{-11}$	$(2.57 \pm 0.18) \times 10^{-9}$	$(1.43 \pm 0.22) \times 10^{-9}$
TSH Plymouth					
		Current: 0.546 nA	Pulser: 386		
Tight	448	$4.430 \times 10^{-10}$	$3.741 \times 10^{-11}$	$(3.11 \pm 0.33) \times 10^{-9}$	$(1.71 \pm 0.28) \times 10^{-9}$
Normal	862	$8.524 \times 10^{-10}$	$4.478 \times 10^{-11}$	$(3.10 \pm 0.21) \times 10^{-9}$	$(1.89 \pm 0.25) \times 10^{-9}$
Wide	2248	$2.223 \times 10^{-9}$	$1.206 \times 10^{-10}$	$(3.32 \pm 0.25) \times 10^{-9}$	$(1.84 \pm 0.29) \times 10^{-9}$
D9a 2016-1					
		Current: 0.856 nA	Pulser: 398		
Tight	287	$1.754 \times 10^{-10}$	$1.606 \times 10^{-11}$	-	-
Normal	589	$3.601 \times 10^{-10}$	$2.068 \times 10^{-11}$	-	-
Wide	1553	$9.494 \times 10^{-10}$	$5.323 \times 10^{-11}$	-	-

<sup>0</sup>For this measurement set, the Greg Herzog standard appears to be measured too low. There was an additional measurement of the D9a 2016-1 just after the Greg Herzog standard that reported lower measured ratios than the others by over an order of magnitude. Something clearly went wrong for this particular sample, however the problem was never identified. I believe the same problem partially affected the Greg Herzog measurement causing the normalised ratio to consistently be lower than the D9 normalised value. As a result, disregard the GH Ratios.

## B.2 Iron Data

For  $^{60}\text{Fe}$ , only one standard was used: the PSI-12 standard. The  $^{60}\text{Fe}$  was sourced from a proton-irradiated copper beam dump at the Paul Scherrer Institute (PSI), as described in [32]. It has a nominal ratio  $1246 \times 10^{-15}$  that was determined via activity measurements. The error in the half-life of  $^{60}\text{Fe}$  is only 2%, which has been included for the final ratios reported in Table 4.4.

The  $^{60}\text{Fe}$  measurements operated slightly different to the  $^{53}\text{Mn}$  measurement as we were primarily battling Poissonian counting statistics. As a result, two measurement sets are reported; the background determination in Table B.3 and the meteorite measurements in Table B.4. The normalised ratios are not reported as these are the final ratios presented in Table 4.4.

**Table B.3:** The raw data for the **blank** measurements taken on the 29<sup>th</sup> of September, 2017. The reported current is the average of the three measured. As only one measurement per sample was taken and only one standard was used, the final ratios are reported in Table B.4. Note that the measured ratios are the  $^{60}\text{Fe}/^{54}\text{Fe}$  ratios which are a factor of 17 larger than the  $^{60}\text{Fe}/\text{Fe}$  ratios.

Sample	$^{54}\text{Fe}$ Current (nA)	Pulser	Counts	Measured Ratio	MR Error
PSI - 12/2	4.306	391	205	$1.951 \times 10^{-11}$	$1.363 \times 10^{-12}$
Fe Blk AA1	4.827	3770	0	0	-
	4.474	3877	0	0	-
	3.601	3918	0	0	-
Fe Blk AA2	4.398	3816	0	0	-
	3.986	3872	0	0	-
	3.667	2870	0	0	-
	4.192	3784	0	0	-
Fe Blk AA3	4.807	3801	0	0	-
	4.824	3854	0	0	-
	4.271	3839	0	0	-
	4.264	3898	0	0	-
	3.345	3897	0	0	-
PSI - 12/2	2.804	394	127	$8.891 \times 10^{-12}$	$7.889 \times 10^{-13}$

**Table B.4:** The raw data for the **meteorite** measurements taken on the 29<sup>th</sup> of September, 2017. The reported current is the average of the three measured. As only one measurement per sample was taken and only one standard was used, the final ratios are reported in Table B.4. Note that the measured ratios are the  $^{60}\text{Fe}/^{54}\text{Fe}$  ratios which are a factor of 17 larger than the  $^{60}\text{Fe}/\text{Fe}$  ratios.

Sample	$^{54}\text{Fe}$ Current (nA)	Pulser	Counts	Measured Ratio	MR Error
PSI - 12/2	2.804	377	105	$1.591 \times 10^{-11}$	$1.553 \times 10^{-12}$
TSI San Angelo	4.294	3514	21	$2.230 \times 10^{-13}$	$4.866 \times 10^{-14}$
	3.972	3711	11	$1.196 \times 10^{-13}$	$3.605 \times 10^{-14}$
PSI - 12/2	2.551	392	94	$1.506 \times 10^{-11}$	$1.554 \times 10^{-12}$
TSI Sacr. Mtns.	4.257	3531	34	$3.624 \times 10^{-13}$	$6.785 \times 10^{-14}$
	3.623	1955	9	$2.036 \times 10^{-13}$	$6.215 \times 10^{-14}$
TSI Tamentit	4.233	3949	34	$3.259 \times 10^{-13}$	$5.588 \times 10^{-14}$
	4.031	3955	25	$2.512 \times 10^{-13}$	$5.024 \times 10^{-14}$
PSI - 12/2	4.512	198	85	$1.524 \times 10^{-11}$	$1.653 \times 10^{-12}$
TSH Plymouth	3.130	3899	23	$3.020 \times 10^{-13}$	$6.296 \times 10^{-14}$
TSH Chulafinnee	3.416	3936	49	$5.839 \times 10^{-13}$	$8.341 \times 10^{-14}$
TSH Durango	3.768	3931	26	$2.812 \times 10^{-13}$	$5.515 \times 10^{-14}$
TSH Charcas	3.541	3944	23	$2.639 \times 10^{-13}$	$5.502 \times 10^{-14}$
PSI - 12/2	2.041	395	78	$1.550 \times 10^{-11}$	$1.755 \times 10^{-12}$



---

# Bibliography

---

- [1] H. Diels and K. Freeman. *Ancilla to the pre-socratic philosophers: a complete translation of the fragments in Diels, “Fragmente der Vorsokratiker”*. Harvard University Press, 1983.
- [2] W. Kutschera. Applications of accelerator mass spectrometry. *International Journal of Mass Spectrometry*, 349-350:203–218, 2013.
- [3] Y. Igarashi, C. K. Kim, Y. Takaku, K. Shiraishi, M. Yamamoto, and N. Ikeda. Application of inductively coupled plasma mass spectrometry to the measurement of long-lived radionuclides in environmental samples a review. *Analytical Sciences*, 6(2):157–164, 1990.
- [4] M. R. Smith, E. J. Wyse, and D. W. Koppenaal. Radionuclide detection by inductively coupled plasma mass spectrometry: A comparison of atomic and radiation detection methods. *Journal of Radioanalytical and Nuclear Chemistry*, 160(2):341–354, 1992.
- [5] N. Trautmann, G. Passler, and K. D. A. Wendt. Ultratrace analysis and isotope ratio measurements of long-lived radioisotopes by resonance ionization mass spectrometry (RIMS). *Analytical and Bioanalytical Chemistry*, 378(2):348–355, 2004.
- [6] M. Poutivtsev, I. Dillmann, T. Faestermann, K. Knie, G. Korschinek, J. Lachner, A. Meier, G. Rugel, and A. Wallner. Highly sensitive AMS measurements of  $^{53}\text{Mn}$ . *Nuclear Instruments and Methods in Physics Research B*, 268(7-8):756–758, 2010.
- [7] K. Dong, M. He, C. Li, H. Hu, G. Liu, Z. Chen, Z. Li, S. Wu, J. Liu, Q. You, C. Jin, X. Wang, H. Shen, Y. Guan, J. Yuan, and S. Jiang. AMS Measurement of  $^{53}\text{Mn}$  at CIAE. *Chinese Physics Letters*, 28(7):070703:1–4, 2011.
- [8] L. K. Fifield. Accelerator mass spectrometry and its applications. *Reports on Progress in Physics*, 62(8):1223–1274, 1999.
- [9] L. Gladkis. *Development of AMS Techniques for  $^{53}\text{Mn}$  and  $^{236}\text{U}$* . PhD thesis, The Australian National University, 2006.
- [10] J. M. Schaefer, T. Faestermann, G. F. Herzog, K. Knie, G. Korschinek, J. Masarik, A. Meier, M. Poutivtsev, G. Rugel, C. Schlüchter, F. Serifiddin, and G. Winckler. Terrestrial manganese-53 – A new monitor of Earth surface processes. *Earth and Planetary Science Letters*, 251(3-4):334–345, 2006.
- [11] T. Fujioka, L. K. Fifield, J. O. Stone, P. M. Vasconcelos, S. G. Tims, and J. Chappell. *In situ* cosmogenic  $^{53}\text{Mn}$  production rate from ancient low-denudation surface in tropic Brazil. *Nuclear Instruments and Methods in Physics Research B*, 268(7-8):1209–1213, 2010.
- [12] M. Honda and M. Imamura. Half-Life of  $\text{Mn}^{53}$ . *Physical Review C*, 4(4):1182–1188, 1971.
- [13] K. Knie, G. Korschinek, T. Faestermann, C. Wallner, J. Scholten, and W. Hillebrandt. Indication for supernova produced  $^{60}\text{Fe}$  activity on Earth. *Physical Review Letters*, 83(1-5):18–21, 1999.
- [14] E. Uberseder, R. Reifarth, D. Schumann, I. Dillmann, C. Domingo Pardo, J. Görres, M. Heil, F. Käppler, J. Marganiec, J. Neuhausen, M. Pignatari, F. Voss, S. Walter, and M. Wiescher. Measurement of the  $^{60}\text{Fe}(n, \gamma)^{61}\text{Fe}$  cross section at stellar temperatures. *Physical Review Letters*, 102(15):151101:1–4, 2009.
- [15] M. Limongi and A. Chieffi. The nucleosynthesis of  $^{26}\text{Al}$  and  $^{60}\text{Fe}$  in solar metallicity stars extending in mass from 11 to  $120 M_{\odot}$ : the hydrostatic and explosive contributions. *The Astrophysical Journal*, 647(1):483–500, 2006.

- [16] K. Knie, G. Korschinek, T. Faestermann, E. A. Dorfi, G. Rugel, and A. Wallner.  $^{60}\text{Fe}$  anomaly in a deep-sea manganese crust and implications for a nearby supernova source. *Physical Review Letters*, 93(17):171103:1–4, 2004.
- [17] J. Feige, A. Wallner, S. R. Winkler, S. Merchel, L. K. Fifield, G. Korschinek, G. Rugel, and D. Breitschwerdt. The search for supernova-produced radionuclides in terrestrial deep-sea archives. *Publications of the Astronomical Society of Australia*, 29(2):109–114, 2012.
- [18] A. Wallner, J. Feige, N. Kinoshita, M. Paul, L. K. Fifield, R. Golser, M. Honda, U. Linnemann, H. Matsuzaki, S. Merchel, G. Rugel, S. G. Tims, P. Steier, T. Yamagata, and S. R. Winkler. Recent near-Earth supernovae probed by global deposition of interstellar radioactive  $^{60}\text{Fe}$ . *Nature*, 532(7597):69–72, 2016.
- [19] D. Breitschwerdt, J. Feige, M. M. Schulreich, M. A. de. Avillez, C. Dettbarn, and B. Fuchs. The locations of recent supernovae near the Sun from modelling  $^{60}\text{Fe}$  transport. *Nature*, 532(7597):73–76, 2016.
- [20] K. Ammon, J. Masarik, and I. Leya. New model calculations for the production rates of cosmogenic nuclides in iron meteorites. *Meteoritics & Planetary Science*, 44(4):485–503, 2009.
- [21] O. Eugster. Cosmic-ray exposure ages of meteorites and lunar rocks and their significance. *Chemie der Erde - Geochemistry*, 63(1):3–30, 2003.
- [22] K. Knie, T. Faestermann, G. Korschinek, G. Rugel, W. Rühm, and C. Wallner. High-sensitivity AMS for heavy nuclides at the Munich tandem accelerator. *Nuclear Instruments and Methods in Physics Research B*, 172(1-4):717–720, 2000.
- [23] K. Knie, S. Merchel, G. Korschinek, T. Faestermann, U. Herpers, M. Gloris, and R. Michel. Accelerator mass spectrometry measurements and model calculations of iron-60 production rates in meteorites. *Meteoritics & Planetary Science*, 34(5):729–734, 1999.
- [24] A. Bischoff, D. Weber, R. Clayton, T. Faestermann, I. A. Franchi, U. Herpers, K. Knie, G. Korschinek, P. W. Kubik, T. K. Mayeda, S. Merchel, R. Michel, S. Neumann, H. Palme, C. T. Pillinger, L. Schultz, A. S. Sexton, B. Spettel, A. B. Verchovsky, H. W. Weber, G. Weckwerth, and D. Wolf. Petrology , chemistry , and isotopic compositions of the lunar highland regolith breccia Dar al Gani 262. *Meteoritics & Planetary Science*, 33(6):1243–1257, 1998.
- [25] U. Ott, S. Merchel, S. Herrmann, S. Pavetich, G. Rugel, T. Faestermann, L. Fimiani, J. M. Gomez-Guzman, K. Hain, G. Korschinek, P. Ludwig, M. D’Orazio, and L. Folco. Cosmic ray exposure and pre-atmospheric size of the Gebel Kamil iron meteorite. *Meteoritics & Planetary Science*, 49(8):1365–1374, 2014.
- [26] T. Smith, B. A. Hofmann, I. Leya, S. Merchel, S. Pavetich, G. Rugel, and A. Scharf. The cosmic-ray exposure history of the Twannberg iron meteorite (IIG). *Meteoritics & Planetary Science*, 52(10):2241–2257, 2017.
- [27] A. Shukolyukov and G. W. Lugmair. Live iron-60 in the early solar system. *Science*, 259(5098):1138–1142, 1993.
- [28] Y. Guan, G. R. Huss, and L. A. Leshin.  $^{60}\text{Fe}$ - $^{60}\text{Ni}$  and  $^{53}\text{Mn}$ - $^{53}\text{Cr}$  isotopic systems in sulfides from unequilibrated enstatite chondrites. *Geochimica et Cosmochimica Acta*, 71(16):4082–4091, 2007.
- [29] H. Tang and N. Dauphas. Abundance , distribution , and origin of  $^{60}\text{Fe}$  in the solar protoplanetary disk. *Earth and Planetary Science Letters*, 359-360:248–263, 2012.
- [30] M. Bizzarro, D. Ulfbeck, A. Trinquier, K. Thrane, J. N. Connelly, and B. S. Meyer. Evidence for a late supernova injection of  $^{60}\text{Fe}$  into the protoplanetary disk. *Science*, 316(5828):1178–1182, 2007.
- [31] G. Rugel, T. Faestermann, K. Knie, G. Korschinek, M. Poutivtsev, D. Schumann, N. Kivel, I. Günther-Leopold, R. Weinreich, and M. Wohlmuther. New measurement of the  $^{60}\text{Fe}$  half-life. *Physical Review Letters*, 103(14-17):072502:1–4, 2009.

- 
- [32] A. Wallner, M. Bichler, K. Buczak, R. Dressler, L. K. Fifield, D. Schumann, J. H. Sterba, S. G. Tims, G. Wallner, and W. Kutschera. Settling the half-life of  $^{60}\text{Fe}$ : fundamental for a versatile astrophysical chronometer. *Physical Review Letters*, 114(4):041101:1–6, 2015.
  - [33] H. A. Synal. Developments in accelerator mass spectrometry. *International Journal of Mass Spectrometry*, 349-350:192–202, 2013.
  - [34] B. X. Han, J. R. Southon, M. L. Roberts, and K. F. von Reden. Computer simulation of MC-SNICS for performance improvements. *Nuclear Instruments and Methods in Physics Research B*, 261(1-2):588–593, 2007.
  - [35] G. S. Jackson, D. E. Elmore, M. Caffee, K. A. Mueller, B. de Bonte, P. Muzikar, and B. Alexander. Ion source modeling and design at PRIME Lab. *Nuclear Instruments and Methods in Physics Research B*, 223-224:155–160, 2004.
  - [36] R. Middleton. A versatile high intensity negative ion source. *Nuclear Instruments and Methods*, 214 (2-3):139–150, 1983.
  - [37] J. G. Trump, F. J. Safford, and R. J. Van de Graaff. Generating voltmeter for pressure-insulated high voltage sources. *Review of Scientific Instruments*, 11(2):54–56, 1940.
  - [38] M. Paul, B. G. Glagola, W. Henning, J. G. Keller, W. Kutschera, Z. Liu, K. E. Rehm, B. Schneck, and R. H. Siemssen. Heavy ion separation with a gas-filled magnetic spectrograph. *Nuclear Instruments and Methods in Physics Research A*, 277(2-3):418–430, 1989.
  - [39] H. D. Betz. Charge states and charge-changing cross sections of fast heavy ions penetrating through gaseous and solid media. *Reviews of Modern Physics*, 44(3):465–537, 1972.
  - [40] R. O. Sayer. Semi-empirical formulas for heavy-ion stripping data. *Revue de Physique Appliquée*, 12 (10):1543–1546, 1977.
  - [41] J. E. Spencer and H. A. Enge. Split-pole magnetic spectrograph for precision nuclear spectroscopy. *Nuclear Instruments and Methods*, 49(2):181–193, 1967.
  - [42] K. Knie, T. Faestermann, and G. Korschinek. AMS at the Munich gas-filled analyzing magnet system GAMS. *Nuclear Instruments and Methods in Physics Research B*, 123(1-4):128–131, 1997.
  - [43] H. W. Fulbright. Ionization chambers. *Nuclear Instruments and Methods*, 162(1-3):21–28, 1979.
  - [44] G. Knoll. *Radiation Detection and Measurement*. John Wiley & Sons, Inc., New York, third edition, 1999.
  - [45] G. Schultz and J. Gresser. A study of transport coefficients of electrons in some gases in proportional and drift chambers. *Nuclear Instruments and Methods*, 151(3):413–431, 1978.
  - [46] J. Buchriegler. *Construction of a Multi-Anode Ionization Chamber for AMS at VERA*. PhD thesis, University of Vienna, 2013.
  - [47] M. Martschini. *Development of methods for isobar suppression in AMS and measurements of  $^{36}\text{Cl}$  with the VERA 3-MV-tandem accelerator*. PhD thesis, The University of Vienna, 2012.
  - [48] G. Rosner, B. Heck, J. Pochodzalla, G. Hlawatsch, B. Kolb, and A. Miczaika. A new position measurement for ionisation chambers. *Nuclear Instruments and Methods*, 188(3):561–569, 1981.
  - [49] T. D. M. Weijers, T. R. Ophel, H. Timmers, and R. G. Elliman. A systematic study of the pulse height deficit in propane-filled gas ionization detectors. *Nuclear Instruments and Methods in Physics Research A*, 483(3):676–688, 2002.
  - [50] A. E. Litherland and L. R. Kilius. A recombinator for radiocarbon accelerator mass spectrometry. *Nuclear Instruments and Methods in Physics Research B*, 52(3-4):375–377, 1990.
  - [51] W. Kutschera. Accelerator mass spectrometry: state of the art and perspectives. *Advances in Physics: X*, 1(4):570–595, 2016.

- [52] J. Ziegler, J. Biersack, and U. Littmark. *The Stopping and Range of Ions in Solids*. Pergamon, 1985.
- [53] J. P. Biersack and L. G. Haggmark. A Monte Carlo computer program for the transport of energetic ions in amorphous targets. *Nuclear Instruments and Methods*, 174(1-2):257–269, 1980.
- [54] H. Bethe. Zur theorie des durchgangs schneller korpuskularstrahlen durch materie. *Annalen der Physik*, 397(3):325–400, 1930.
- [55] F. Bloch. Zur bremsung rasch bewegter teilchen beim durchgang durch materie. *Annalen der Physik*, 408(3):285–320, 1933.
- [56] N. Bohr. On the decrease of velocity of swiftly moving electrified particles in passing through matter. *Philosophical Magazine*, 30(178):581–612, 1915.
- [57] Q. Yang, D. J. O'Connor, and Z. Wang. Empirical formulae for energy loss straggling of ions in matter. *Nuclear Instruments and Methods in Physics Research B*, 61(2):149–155, 1991.
- [58] C. Vockenhuber, K. Arstila, J. Jensen, J. Julin, H. Kettunen, M. Laitinen, M. Rossi, T. Sajavaara, M. Thöni, and H. J. Whitlow. Energy loss and straggling of MeV Si ions in gases. *Nuclear Instruments and Methods in Physics Research B*, 391:20–26, 2016.
- [59] H. Schmidt-Böcking and H. Hornung. Energy straggling of CI ions in gases. *Zeitschrift für Physik A*, 286(3):253–261, 1978.
- [60] A. S. Schlachter, J. W. Stearns, W. G. Graham, K. H. Berkner, R. V. Pyle, and J. A. Tanis. Electron capture for fast highly charged ions in gas targets: An empirical scaling rule. *Physical Review A*, 27(6):3372–3374, 1983.
- [61] D. Burch and K. Green. University of Washington, Annual Report: Multiple scattering of heavy ions. Technical report, 1976. URL <https://www.osti.gov/scitech/servlets/purl/6222351>.
- [62] G. J. Feldman and R. D. Cousins. Unified approach to the classical statistical analysis of small signals. *Physical Review D*, 57(7):3873–3889, 1998.
- [63] O. Bunemann, T. E. Cranshaw, and J. A. Harvey. Design of grid ionisation chambers. *Canadian Journal of Research*, 27a(5):191–206, 1949.
- [64] M. Martschini, J. Buchriegler, P. Collon, W. Kutschera, J. Lachner, W. Lu, A. Priller, P. Steier, and R. Golser. Isobar separation of  $^{93}\text{Zr}$  and  $^{93}\text{Nb}$  at 24 MeV with a new multi-anode ionization chamber. *Nuclear Instruments and Methods in Physics Research B*, 361:201–206, 2015.
- [65] O. Forstner, P. Andersson, C. Diehl, R. Golser, D. Hanstorp, W. Kutschera, A. Lindahl, A. Priller, P. Steier, and A. Wallner. Isobar suppression in AMS using laser photodetachment. *Nuclear Instruments and Methods in Physics Research B*, 266(19-20):4565–4568, 2008.